8-2021

Investigation on the Interaction of an Impinging Jet with Cylinder Wakes

Karthik Krishna

INVESTIGATION ON THE INTERACTION OF AN IMPINGING JET WITH CYLINDER WAKES

By

Karthik Krishna

A Dissertation Submitted to the Faculty of Embry-Riddle Aeronautical University

In Partial Fulfillment of the Requirements for the Degree of

Doctor of Philosophy in Aerospace Engineering

August 2021

Embry-Riddle Aeronautical University

Daytona Beach, Florida

INVESTIGATION ON THE INTERACTION OF AN IMPINGING JET WITH CYLINDER WAKES

By

Karthik Krishna

This Dissertation was prepared under the direction of the candidate's Dissertation Committee Chair, Dr. Mark Ricklick, Department of Aerospace Engineering, and has been approved by the members of the Dissertation Committee. It was submitted to the Office of the Senior Vice President for Academic Affairs and Provost, and was accepted in the partial fulfillment of the requirements for the Degree of Philosophy in Aerospace Engineering.

DISSERTATION COMMITTEE

Mark Ricklick Digitally signed by Mark Ricklick Date: 2021.07.14 15:54:25 -04'00'

Chairman, Dr. Mark Ricklick

Dr. Magdy S. Attia Digitally signed by Dr. Magdy S. Attia Date: 2021.07.18 19:20:24 -05'00'

Member, Dr. Magdy S. Attia

Sandra Boetcher Digitally signed by Sandra Boetcher Date: 2021.07.15 14:38:59 -04'00'

Member, Dr. Sandra Boetcher

Reda Mankbadi Digitally signed by Reda Mankbadi Date: 2021.07.14 19:16:40 -04'00'

Member, Dr. Reda Mankbadi

Sirish Namilae

Graduate Program Coordinator,
Dr. Sirish Namilae

08/03/2021

Date

Maj Dean Mirmirani

Dean of the College of Engineering,
Dr. Maj Mirmirani

08/03/2021

Date

Senior Vice President for Academic Affairs and Provost,
Lon Moeller, J.D.

08/04/2021

Date

ACKNOWLEDGEMENTS

I want to dedicate this work to my mom Bhagyalakshmi and my dad Krishna who have supported and encouraged me to follow my dreams of becoming an Aerospace Engineer no matter how hard it was for them. A special thanks to my wife Sheetal for all the time she spent critiquing my manuscript and believing in me. I want to thank my advisor, Dr. Mark Ricklick, for his support, patience, and guidance. I am blessed to have spent time in his tutelage.

I also like to thank all the professors of the Aerospace Engineering department at ERAU who taught me a tremendous number of lessons about academics and life. I want to thank my lab mates Anish, Neil, John, Devon, and Paula, for helping in my research.

Finally, and the most important of everything, I would like to thank my family, and friends, without your help and encouragement, I could not have achieved this great accomplishment.

ABSTRACT

Jet impingement cooling is a widely used cooling method due to the high heat transfer rates associated with it. Research for improving heat transfer rates for this cooling method is still being carried out due to its broad application in various fields like gas turbine blade cooling, electronic component cooling, and paper drying. The unsteady jet oscillation effectively enhances the stagnation region and the time-averaged heat transfer rates. It is shown that a novel passive jet oscillation technique can be achieved using the vortices periodically shed from a cylinder placed upstream in a channel with an initial crossflow. Preliminary CFD results prove the hypothesis of jet oscillation induced by the cylinder vortices and that the lateral jet oscillation is an efficient method for uniform distribution of heat transfer. The statistical analysis concluded jet oscillation is most sensitive to cylinder vortex strength. A frequency spectral analysis is performed to classify oscillating and non-oscillating cases. Finally, unsteady numerical and experimental research is carried out to determine the effect of cylinder-jet distance, cylinder diameter, and velocity ratio on jet oscillation and heat transfer rate. The range of cylinder-jet distance and velocity ratio tested are S/d = 2 – 4 and VR = 4 – 12, respectively. The flow interaction mechanism leading the jet oscillation is analyzed using TKE, vorticity, and velocity contours in time. The flow feature analysis concluded the cylinder wakes deformed the jet core inducing lateral and angular oscillations. The heat transfer results showed the Nusselt number is proportional to the velocity ratio for oscillating jet cases. The non-oscillating jet enhances the heat transfer rate by 94% in the wall jet region due to crossflow interaction. And the optimum oscillating jet case improved the stagnation region Nusselt number by 19%.

TABLE OF CONTENTS

LIST OF FIGURES

Figure Page

Figure Page

Figure Page

Figure Page

Figure Page

LIST OF TABLES

NOMENCLATURE

A_c	Cross-sectional area	m^2
A_s	Surface area	m^2
a_∞	Speed of sound	m/s
B or b	Systematic uncertainty	
C_0 to C_4	Coefficients	
CFD	Computational Fluid Dynamics	
C_p	Specific heat capacity at constant pressure	J/Kg.K
CMOS	Complementary Metal Oxide Semiconductor	
D	Jet diameter	m
d	Cylinder diameter	m
e_1 to e_n	Measuring device errors	
E_a	Recorded voltage	V
E_{corr}	Corrected voltage	V
GPM	Gallons per minute	
H	Height of the channel	m
h	Height of the cylinder	m
I	Current	A
I_s	Surface intensity	
I_{ref}	Reference intensity	

k	Thermal conductivity	W/m.K
k_0	Sutherland's constant for thermal conductivity	W/m.K
L	Length of the channel	m
LED	Light emitting diode	
n	Number of pixels in streamwise direction	
N	Sample size	
Nu	Nusselt number	
$\dot{\mathbf{m}}$	Mass flow	Kg/s
P	Pressure	Pa
P_0	Chamber pressure	Pa
P_c	Pressure correction	Psig
PVC	Polyvinyl chloride	
P_∞	Atmospheric pressure of the room	Pa
q"	Heat flux	W/m^2
$q"_{loss}$	Heat flux lost	W/m^2
$q"_{sup}$	Heat flux supplied	W/m^2
q(x)	Heat supplied per spanwise row of pixel	W/m
$\dot{q}$	Internal heat generation	W/m^3
R	Gas constant	J/Kg.K
RANS	Reynolds Averaged Navier Stokes	

Re	Reynolds number	
S	Random uncertainty	
SCFM	Standard cubic feet per minute	
SST	Shear Stress Transport	
S_k	Sutherland's constant for temperature	K
T	Temperature	K
T_3	Turbine inlet temperature	K
T_4	Turbine exit temperature	K
T_0	Calibration temperature	K
T_0	Sutherland's constant for temperature	K
t_{95}	Student t confidence interval	
T_a	Ambient temperature	K
T_c	Temperature correction	°R
TI	Turbulence Intensity	
T_{ref}	Reference temperature	K
T_s	Surface temperature	K
TSP	Temperature Sensitive Paint	
T_w	Wall Temperature	K
Tj	Jet Temperature	K
T_∞	Temperature of the jet	K

u_y	Calculated uncertainty	
U_{mean}	Mean velocity	m/s
U_{rms}	Root mean square velocity	m/s
U_y	Final uncertainty	
V	Voltage	V
V	Velocity	m/s
V_∞	Jet velocity	m/s
w	Width of strip	m
γ	Ratio of specific heats	
ρ	Resistivity	Ω.m
ρ	Density	Kg/m^3
μ	Dynamic viscosity	Pa.s
μ_0	Sutherland's constant for dynamic viscosity	Pa.s
σ_x	Standard deviation	

1. Introduction

The gas turbine engine (GTE) is efficient and extensively used in power production and gas propulsion. The ever-growing demand for higher power and efficiency has led researchers and industries to take advantage and invest their skills and finance in this field of study. A typical gas turbine engine (shown in Figure 1.1) consists of four components: compressor; combustor; turbine; and nozzle. The axial compressor ingests the incoming air and delivers compressed air to the combustor. In the combustor, heat is added by burning chemical fuel further increases the working fluid's total temperature. The high-energy hot gas is expanded in the turbine to extract energy to drive the compressor and generator (for industrial GTE). Finally, a nozzle is used to expand the gasses to produce thrust for a gas propulsion engine. The application of the gas generator output determines the GTE configuration (Boyce, 2011).

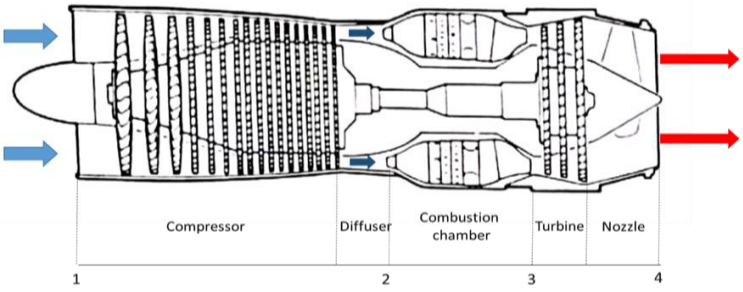

Figure 1.1 Gas turbine engine (Boyce, 2011)

1.1. Motivation

Jet impingement cooling is a widely used cooling method due to the high heat transfer rates associated with it. Research for improving heat transfer rates for this type of cooling is still being carried out due to its wide application in various fields like gas turbine blade

cooling, electronic component cooling, and paper drying.

One approach which yields high heat transfer rates is the use of unsteady oscillating impingement jets. Here, the target surface is cooled by a high-speed fluid jet whose position periodically transitions from one extreme to another. Implementation of existing oscillation techniques may not be suitable for current industrial manufacturing methods and environments. The adverse impacts of crossflow development, passage clogging, and breakage of small features must be addressed. Therefore, a robust design is necessary that will continue to yield adequate rates of heat transfer even in the presence of these failures.

1.2. Thermodynamics of Gas Turbine Engine

The thermodynamic ideal Brayton cycle (neglecting losses) is shown in Figure 1.2, which shows the cyclic working process of a gas turbine engine. The first process is the isentropic compression of the incoming air to high pressure using an axial or a centrifugal compressor, process1-2. This process also leads to an increase in temperature due to the rise in pressure. Secondly, heat energy is added into the system by burning fuel in the combustor, process 2-3 (constant pressure heat addition). The maximum temperature allowable at the exit of the combustor is limited by the material and cooling capability of the turbine blade used in the following stage. The combustor exit temperature limit of the current generation engine is approximately 1500 ºCelsius (Hill et al., 1992). The turbine expands the working fluid and extracts energy for driving the compressor, process 3-4 (isentropic expansion). The 4-1 is an isobaric process, decreasing the temperature from T4 to T1 to close the ideal cycle. The thermal efficiency (shown in equation 1) is derived as a function of the working temperatures.

$$\eta_{Brayton} = 1 - \frac{T_4 - T_1}{T_3 - T_2} \quad (1)$$

The atmospheric inlet temperature (T1), the compressor outlet temperature (T2), and the turbine outlet temperature (T4) are fixed by the compressor design and working conditions of the GTE. The turbine blade's thermal capability limits the turbine inlet temperature (T3). The turbine inlet temperature (T3) is also found to be proportional to the efficiency of the Brayton cycle. Hence, the material capability and cooling technology advancement dictate the efficiency of a gas turbine engine. Currently, the superalloy material limit is approximately 1000 ºCelsius. Further cooling the blade using the known cooling methods will increase the limit to 1500 ºCelsius (Hill et al., 1992; Halbig et al., 2013).

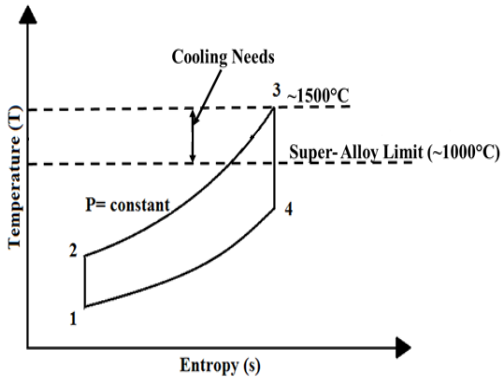

Figure 1.2 Brayton cycle

1.3. Gas Turbine Cooling

The cooling of a gas turbine's hot components is a crucial process required to maintain lower thermal stresses and facilitate higher working turbine inlet temperatures. The allowable turbine inlet temperature is also limited by the material capability of the

turbine components. In the early 1950s, the increase in turbine inlet temperature is only governed by material property research advancement (shown in Figure 1.3). Later in the 1960s, researchers explored the importance of cooling technology, leading to the increased turbine inlet temperature. Further comparing the trend between material capability and cooling capability research advancement, cooling methods have led to a higher increase in turbine inlet temperature due to the variety of cooling methods available for researchers to enhance and develop.

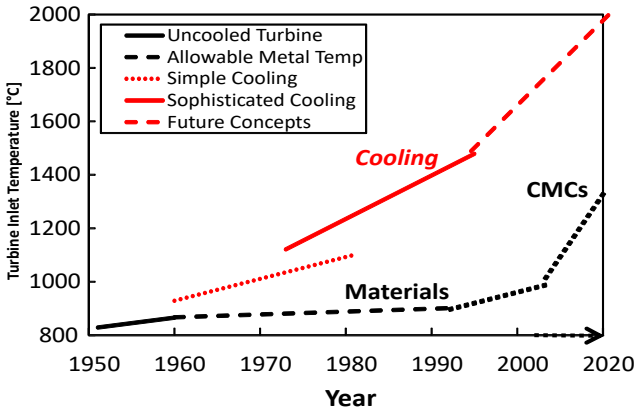

Figure 1.3 Evolution of turbine inlet temperature (Ricklick et al., 2015)

The cooling techniques used can be mainly classified into two streams: internal blade cooling and external surface cooling. Internal cooling of the turbine blade configures using cooling methods like jet impingement cooling, pin fin cooling, serpentine cooling channels, and ribbed channel cooling. The external surface cooling of the turbine blade is based on producing a layer/film of relatively cold air around the blade to protect it from the hot gasses. Complex designs incorporating both internal and external cooling methods are being used and developed to provide higher turbine inlet temperatures for GTE. An

example of an intricate design involving internal and external cooling arrangement in a gas turbine blade is shown in Figure 1.4 (Ricklick et al., 2015; Han et al., 2012).

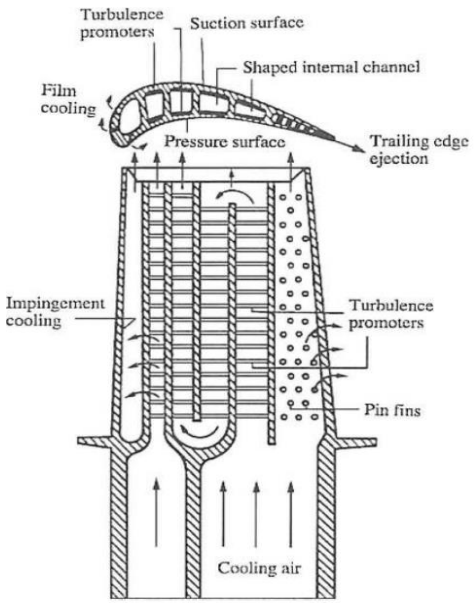

Figure 1.4 Typical internal and external turbine blade cooling (Han et al., 2012)

1.4. Jet Impinging Cooling

The jet impingement cooling method is an effective cooling method used to generate high local heat transfer rates. This method's high heat removal capability has led to its implementation in fields like internal cooling of a gas turbine blade, food industry, paper drying, textile drying, and electronic component cooling (Han et al., 2012).

A typical jet impingement cooling (shown in Figure 1.5) constitutes a core fluidic jet produced by an orifice or a slot (jet diameter = D) targeted onto a plate (impingement surface/ target surface). The distance between the jet orifice and the target plate is the displacement height of impingement (H/D), the geometrical point of impingement of the jet onto the target plate is the stagnation point (r/D = 0).

An impingement flow is divided into three regions: the free jet region, the stagnation region, and the wall jet region. The free jet region is the jet developed from the slot and acts like a submerged jet when the slot is sufficiently distant from the impingement surface (H/D>2). Due to the shear-driven interaction between the jet and the surrounding, the surrounding is entrained into the jet leading to an increase in mass flow rate.

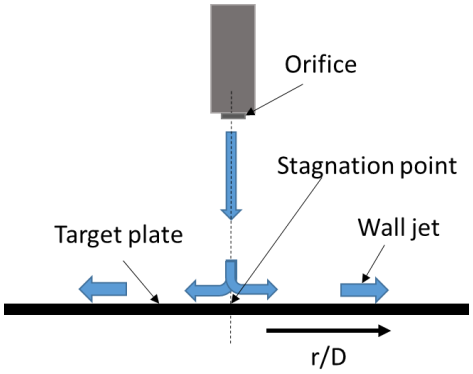

Figure 1.5 Jet impingement configuration

The free jet is further divided into three regions: potential core region, developing region, and fully developed region (shown in Figure 1.6). The core region is the region with the centerline velocity equal to jet exit velocity. The core region is continuously expanding in the spatial direction with the entrainment of the surrounding fluid due to the shear layer mixing. The length of the core region is found to be 6-7 jet diameter. At the end of the potential core, the center line jet velocity is 95% of the exit jet velocity. Further, the jet velocity decreases with the increase in shear layer interaction moving into the developing zone. The velocity profile is stretched in the x-direction in the fully developed region, further reducing the centerline velocity (Shukla et al., 2017).

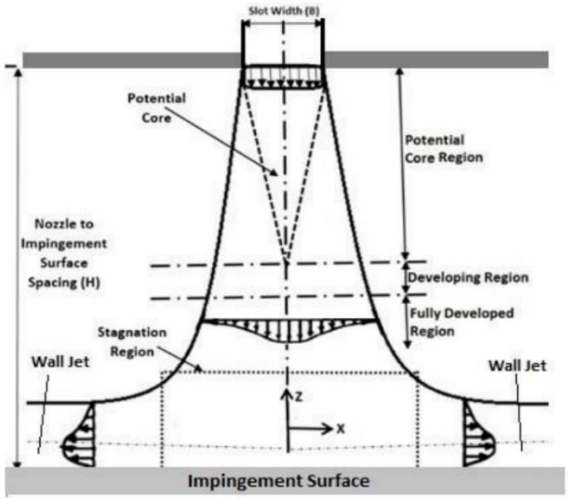

Figure 1.6 Flow schematic of a jet impingement flow (Shukla et al., 2017)

The jet moves towards the wall creating a stagnation region and deflects upon impingement. As a result, the jet's kinetic energy in the z-direction decreases, leading to increased static pressure on the wall. The local point with the highest static pressure is the stagnation point. Later on, the jet flow is expanded radially outwards from the stagnation point, creating the wall jet.

Jet impingement flow is classified into confined and unconfined jet impingement. The unconfined jet impingement is the geometrical arrangement with no walls, and the wall jet can move radially downstream parallel to the target surface, as discussed above. The confined jet impingement is the geometrical arrangement where the fluidic jet is contained within the channel walls, usually in a multiple jet arrangement (Figure 1.7). In this configuration, the wall jet impinges on the sidewall and deflects upwards, creating a vortical entraining of more fluid. These vortices move downstream, interacting and deflecting downstream jets (Figure 1.7). The deflection of the jet downstream is directly proportional to the crossflow accumulation produced by the upstream jets. The jet

deflection creates an adverse effect on the heat removal capability of the jet. Hence the jet deflection should be minimum for maximum heat transfer (Shukla et al., 2017).

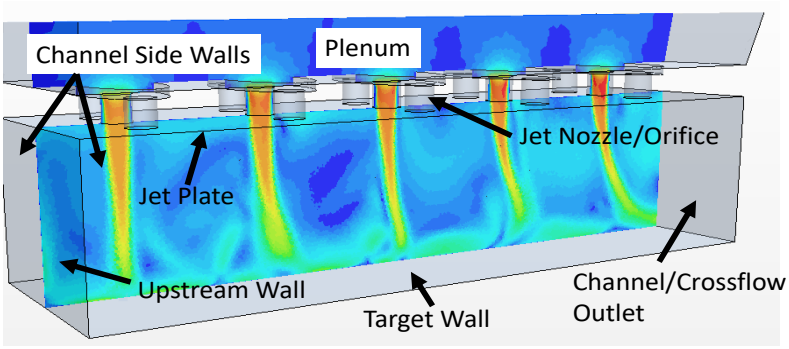

Figure 1.7 Impingement channel configuration

1.5. Unsteady Jet Impingement

Unsteady jet impingement studied in this current research is the periodic jet core oscillation leading to benefits in heat transfer rate. Jet impingement is a quasi-steady-state process provided the flow and geometrical parameters discussed earlier are fixed, with no flow interaction with the crossflow or the neighboring jet. Therefore, studies on unsteady jet impingement are related to the method in which the unsteadiness is generated in the jet impingement flow structure. Broadly unsteady jet impingement can be classified based on the excitation method. Jet oscillation produced by external energy sources like piezoelectric reeds can be classified as active jet oscillation. And passive jet oscillation is a technique utilizing the internal energy of the jet or surrounding flow structure to impart jet oscillation. A flow chart showing the classification of unsteady jet impingement is shown in Figure 1.8. Also, examples of active and passive jet oscillation techniques are listed in the flow chart.

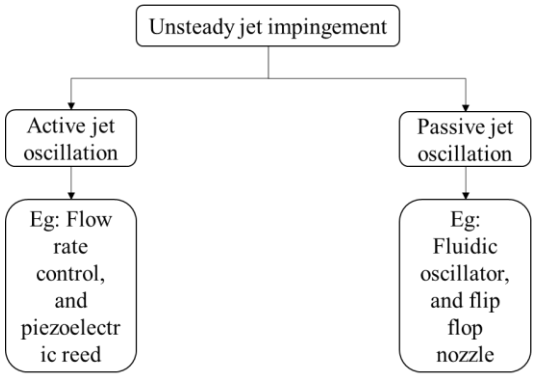

Figure 1.8 Unsteady jet impingement classification

2. Literature Review

The current work intends to find a robust technique for jet oscillation leading to enhanced heat transfer rate. Numerous methods exist leading to jet oscillation. However, none fit the intended goal of this study to develop a robust jet oscillation technique. Hence, the literature works of basic jet impingement characteristics and previous jet oscillating techniques are discussed in the first and second subsections. Soon to discuss the hypothesis of using cylinder wakes for jet oscillation. Therefore, the last subsection discusses the literature on cylinder wake formation from a cylinder.

2.1. Jet Impingement

The impingement heat transfer configuration results in a heat transfer rate peak at the stagnation point ($r = 0$) and decays radially outward (for $H/D > 2$). A secondary peak in heat transfer distribution is observed if the impingement surface is closer to the jet orifice ($H/D < 2$). This phenomenon is caused by the increase in the wall jet turbulence, as shown in Figure 2.1 (O'Donovan et al., 2007). The heat transfer capability of this cooling technique is directly proportional to the Reynolds number of the jet and inversely proportional to the height of impingement. Due to the change in kinetic energy of the jet impinging onto the target plate. However, maximum heat transfer capability is attained at a jet to plate distance, $H/D = 6$ (Chakroun et al., 1997).

Heat transfer rates due to impingement are among some of the highest per unit mass flow and are therefore often used in areas with high thermal loading (Ligrani et al., 2003; Lee, 1999). Another implementation of the jet impingement is within a channel, such that the exhausted jet flow is confined to flow axially along the channel after impingement, as shown in Figure 2.2. (Parida, 2015; Liang, 2012).

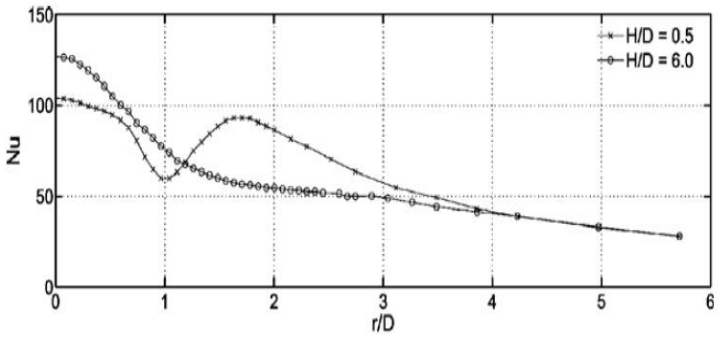

Figure 2.1 Unconfined jet impingement Nu distribution (O'Donovan et al., 2007)

The crossflow rate increases in the downstream direction with an increase in the number of jets. The crossflow interacts with the impinging jets downstream and aerodynamically pushes the core jet from the geometrical point of impingement (shown in Figure 2.2). The jet deflection causes a detrimental effect on the heat transfer rate (Ricklick, 2009; Ricklick and Kapat, 2010).

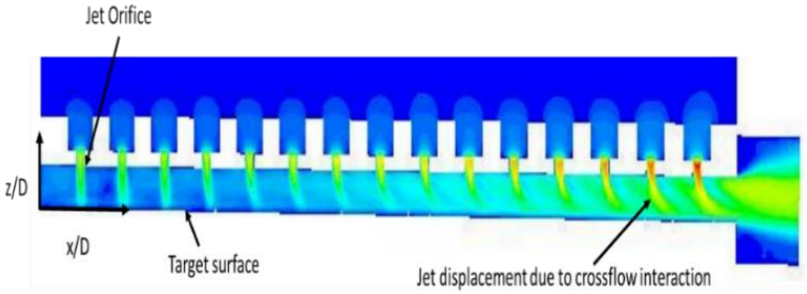

Figure 2.2 Velocity contour of row jet impingement (Ricklick, 2009)

In channel jet impingement, the heat transfer distribution (Figure 2.3) is highest at the individual stagnation point. The heat transfer rate radially decays similar to unconfined jet impingement, an additional decrease in HTC is observed in the x-direction due to the

crossflow interaction. While high heat transfer rates are achieved at the stagnation point, the radial decay can lead to thermal stresses if not accounted for (Ricklick et al., 2010). The high local heat transfer rate can be distributed radially, improving the average heat transfer rate and reduce thermal stresses. An approach to distributing the thermal load and improving average HTC is to utilize an unsteady oscillating jet, spreading the stagnation region into a wider area.

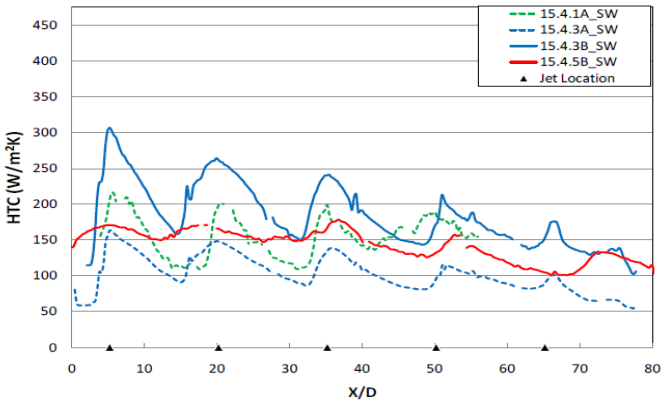

Figure 2.3 Channel row jet impingement span averaged HTC (Riclick, 2009)

2.2. Jet Impingement in Crossflow

The jet flow field in a crossflow (JICF) is primarily affected by the crossflow strength, quantified by the jet-crossflow momentum ratio (J). A typical flow structure evolved by the interaction of a jet in crossflow is shown in Figure 2.4. The flow structures observed are dominated by the counter-rotating vortex pair (CVP) generated near the jet nearfield region. Also, the JICF leads to the formation of vortical structures like horseshoe vortices, leading-edge/lee-side vortices, wake vortices, and the counter-rotating vortex pair. (Karagozian, 2014).

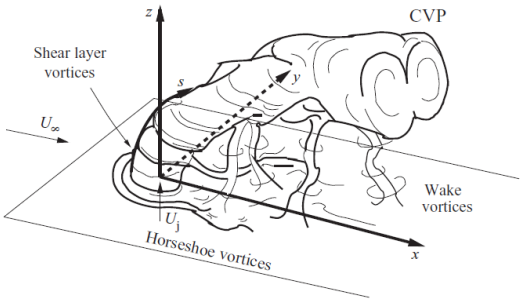

Figure 2.4 Schematic of flow structure of a jet in crossflow (Karagozian, 2014)

Working under the assumption of constant density flows the momentum ratio can be reduced to velocity ratio, shown in Equation 2. Hence, the jet deflection is primarily influenced by the velocity ratio (He et al., 1999).

$$VR = \frac{V_j}{V_{CF}} \tag{2}$$

As the jet is primarily affected by the velocity ratio (VR), a generalized jet trajectory equation can be formed, shown in Equation 3. Various works of literature exist determining an effective way to predict the jet deflection, primarily predicting the constants A and B. The jet-crossflow interaction will lead to the deformation of the jet core as the jet penetrates the crossflow. The jet nozzle shape also influenced the deflection and deformation of the jet (Muppidi et al., 2005).

$$\frac{y}{VR\ d} = A\ \left(\frac{x}{VR\ d}\right)^B \tag{3}$$

2.3. Unsteady Jet Impingement

Unsteady jet impingement can be achieved in various methods like flow rate control, Coanda effect, fluidic oscillator, vortex shedding from a cylinder/active reed placed at the nozzle exit, and cavity interaction.

An experimental analysis was carried out to study the effect of unsteady jet flow rate on heat transfer rate. This study showed that the active jet flow rate control technique augmented the heat transfer rate by 30% in some cases when compared against its quasi-steady counterpart. In addition, a detailed analysis of the flow feature using PIV and hotwire technique was carried out. Results concluded that the unsteadiness induced generated vortical structures at the free boundary shear layer interface as the jet exited the nozzle, which was the primary driver to increase the heat transfer rate. The results also showed uniform Nusselt number distribution at a higher frequency of flow rate oscillation, whereas at lower frequencies deteriorating heat transfer rates were observed near the stagnation region (Middelberg and Herwig, 2009; Zhou et al., 2009).

Similar to the previous study, a 2D numerical investigation was carried out on two inline jet configuration with unsteady jet flow rate (Figure 2.5). The results showed that the unsteadiness disrupted the boundary layer leading to an augmentation in heat transfer rate and uniform temperature distribution on the target surface, as shown in Figure 2.6 (Hewakandamby, 2009).

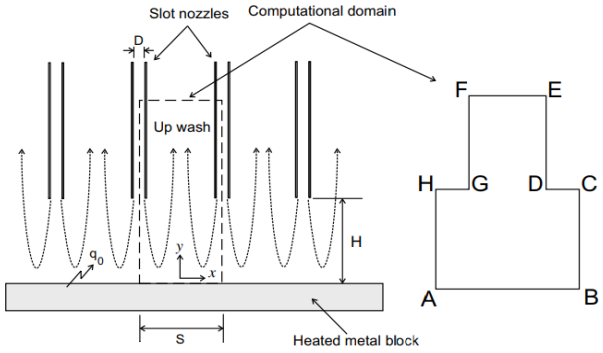

Figure 2.5 Multiple jet flow rate control (Hewakandamby, 2009)

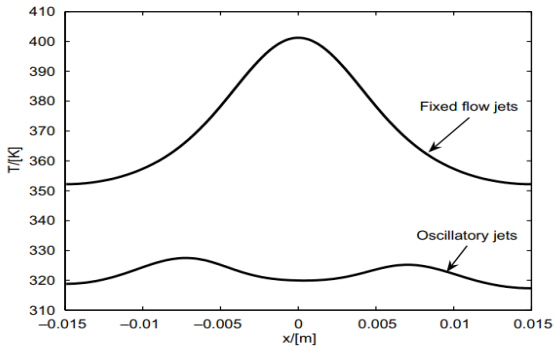

Figure 2.6 Consecutive oscillating jet (Hewakandamby, 2009)

Research on inducing jet oscillation was initially investigated by H. Viets, 1975 for thrust enhancement by oscillating the jet using a flip-flop nozzle with a fluidic actuator controlling the jet flow path. This nozzle had no moving parts hence classified as a passive jet oscillation technique, shown in Figure 2.7. As the jet emerges from the orifice, it is pushed by the fluidic actuator to either right or left wall. Consider the jet now being attached to wall A by the Coanda effect. Due to fluid entrainment, the pressure at port A' is lower, whereas port B' is higher on the other side. As the two ports are connected, a compression wave travels from port B' to port A', leading to the rise in pressure pushing the jet across to wall B. Conversely, leading to the decrease in pressure at port B and a compression wave from port A' to B' to push the jet back to wall A. Results also show the jet frequency is dependent upon the geometrical characteristics of the actuator loop (Viets, 1975; Herwig et al., 2004).

Due to the thrust improvement and enhanced mixing (turbulent features) capability shown by H. Viets (1975), researchers showed interest in developing self-excited passive jet oscillation methods like the Karman jet nozzle and the precessing jet nozzle. The Karman jet nozzle is a geometrical arrangement with a cylinder at the nozzle exit. The

cylinder introduces von Karman vortex street into the jet by periodic vortex shedding (Figure 2.8a). The precessing jet nozzle works on the Coanda effect; the inverted chamfer at the exit of the jet orifice amplifies the perturbation in the flow. This perturbation results in the jet attaching to one side of the wall, and it revolves around the chamfer producing a precessing motion. The frequency of precession depends on the size of the nozzle and the jet Reynolds number. The setup of this nozzle is shown in Figure 2.8b (Herwig et al., 2004).

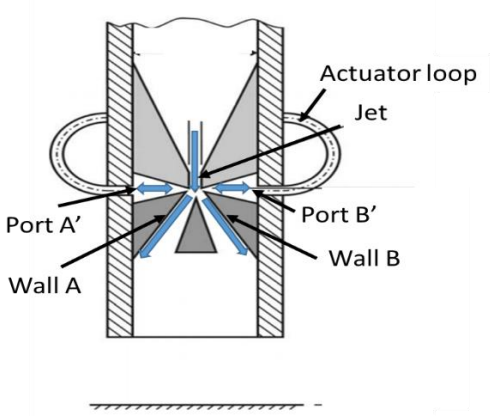

Figure 2.7 Flip-Flop nozzle (Herwig et al., 2004)

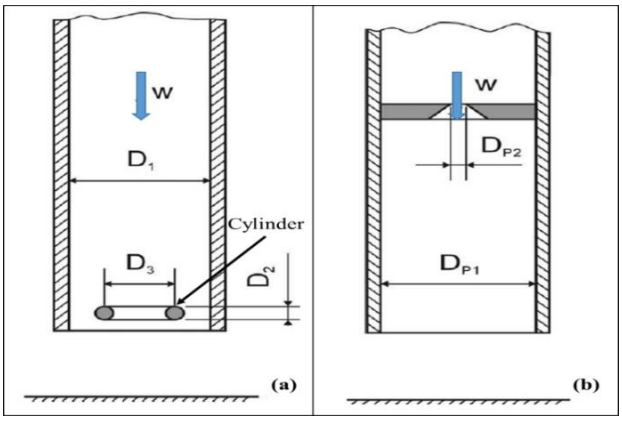

Figure 2.8 Karman nozzle (a); precessing nozzle (b) (Herwig et al., 2004)

Experimental analysis was carried on a flip-flop nozzle with no wall separator combined with a pulsed flow rate nozzle. Also, the author investigated the effect of these nozzles on fluid entrainment. Results showed that the pulsed flow rate nozzle performed better than the fluidic flip-flop nozzle (Platzer et al., 1978). The use of two flip-flop nozzles at an angle targeted towards a primary jet at the center was experimentally investigated to force oscillations into the primary jet. This technique successfully forced velocity perturbation in the main jet. The jet velocity decayed more rapidly for the forced cases than the unforced cases, proving higher entrainment due to shear layer interaction. However, the effect of heat transfer rate was unexplored (Raman and Cornelius, 1995).

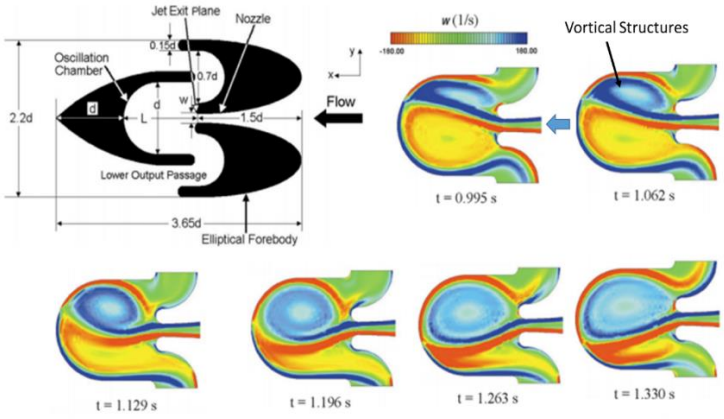

Figure 2.9 CFD vorticity contour of a fluidic oscillator (Uzol and Camci, 2002)

Experimental and computational analysis was carried out on a fluidic oscillator similar to a self-excited flip-flop nozzle. The jet movement is caused by the vortical structures generated by the target wall (Figure 2.9). The vorticity distribution of this nozzle for one time period is shown in Figure 2.9. At t = 0.995seconds, the jet is attached to the upper side of the concave wall, resulting in vortical structures. These vortices push

the jet to the other side of the wall (t = 1.33s). The author concluded that the jet spends more time on the sidewalls than the transition period between walls due to the stability criteria. Also, the oscillating jet frequency was proportional to the jet Reynolds number (Uzol and Camci, 2002).

Researchers further investigated the passive jet oscillation similar to flip-flop nozzle to understand the frequency control and flow dynamics under different jet inlet conditions and control port conditions (Tesar and Zimmerman, 2006; Koklu and Owens, 2014). The effect of the control port in a flip-flop nozzle was studied experimentally.

An empirical formula (Equation 4-5) was developed to show the jet oscillation frequency (or Strouhal number) is a function of the inner diameter of the connecting tube (d/s), length of the connecting tube (L/s), and Jet Reynolds number (Re_j). The results also showed that the frequency decreased with the increase in the tube length due to the time required for the compression wave to travel (Inoue et al., 2016).

$$f = \frac{St\ V}{s} \tag{4}$$

Where, V = jet velocity, s = orifice/slot width and St = Strouhal number.

$$St = C\left(\frac{L}{s}\right)^{\alpha}\left(\frac{d}{s}\right)^{\beta} Re^{\gamma} \tag{5}$$

Where, C = 0.068, α = -0.72, β = 1.37 and γ = 0.22.

The use of the flip-flop fluidic actuator in heat transfer applications has found interest during the 21st century. Camci and Herr (2002) experimentally tested the effect of the flip-flop jet on heat transfer capability. The results showed augmentation of heat transfer rate by 70% compared to the steady jet impingement result. The Nusselt number distribution comparing a steady and oscillating jet at Reynolds number Re_j = 7500 is

shown in Figure 2.10. The oscillating jet has higher local heat transfer rates than a steady jet. Also, the lateral jet oscillation leads to an increase in the stagnation area region. The author mentioned that the level of heat transfer augmentation achieved would be useful if implemented in a turbine blade. But, it is also essential to understand the effect of manufacturing and maintenance difficulties experienced in implementing this technology.

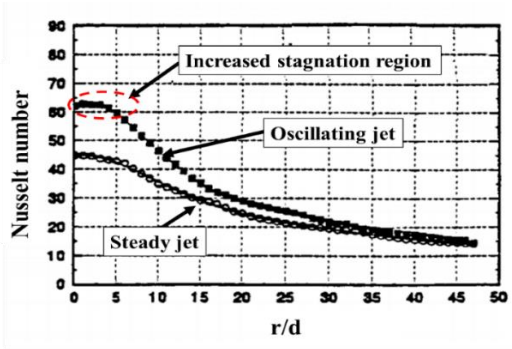

Figure 2.10 Steady and oscillating jet Nu Distribution (Camci and Herr, 2002)

Similar to the previous study, a hybrid synthetic flip-flop nozzle was experimentally investigated to determine the heat transfer rate. Results showed a maximum of 300% increase in heat transfer rate (Tesar, 2009).

Experimental analysis of a fluidic oscillator invented by Bowels Fluidic Corporation was investigated to determine heat transfer rate (Agricola et al., 2017). The Fluidic oscillator is shown in Figure 2.11. As the jet expands downstream through the nozzle, the unstable jet attaches to one sidewall. Upon attachment, a recirculation region is developed at the entrance of the opposite wall feedback loop blocking it, and a part of the flow is forced into the wall feedback loop (Figure 2.11). The flow travels upstream near the throat to push the jet onto the other sidewall, and the process is repeated.

The results showed that a sweeping jet's maximum heat transfer rate is obtained at a jet to plate distance, h/D = 5. The literature on steady jet impingement suggests maximum heat transfer is achieved at a jet to plate distance, h/D = 6. A sweeping jet travels an additional distance before impingement; hence the h/D required by a sweeping jet is less than its steady counterpart for maximum heat transfer rate (Agricola et al., 2017).

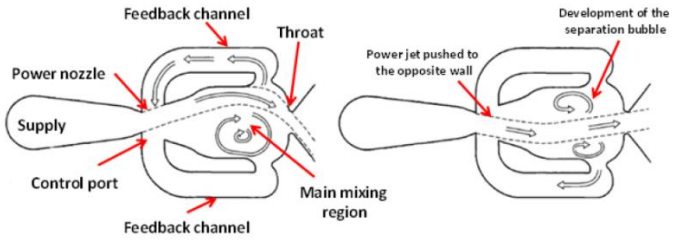

Figure 2.11 Fluidic oscillator (Agricola et al., 2017)

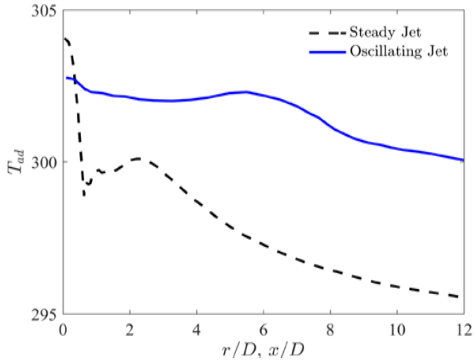

Figure 2.12 Temperature profile of oscillating jet (Lundgreen et al., 2017)

A numerical investigation was carried out on a sweeping jet using unsteady RANS k-ω SST and k-ε v^2f turbulence model. Comparing the CFD and experimental results showed k-ω SST model performed better than the k-ε v^2f turbulence model in matching the experimental results. The time-averaged temperature distribution for a jet to plate

distance, h/D = 4, is showed in Figure 2.12. The temperature distribution is uniform for the oscillating jet, whereas the steady jet produces non-uniform radially decaying temperature profiles (Lundgreen et al., 2017).

An array of fluidic jet oscillators was applied to a turbine vane leading edge, as shown in Figure 2.13. Conjugate heat transfer experiments were carried out in a low-speed wind tunnel. The sweeping jet was fabricated using additive manufacturing. The literature quantified the effect of jet spacing, jet to plate distance, jet Reynolds number, and aspect ratio of the sweeping jet on overall cooling effectiveness. The literature concluded maximum heat transfer rate at a jet plate distance H/D = 5, the cooling performance is higher at a pitch P/D = 4, and the sweeping jet tends to produce smaller pressure drop than the steady jet (Hossain et al., 2018).

Implementing the above-discussed literature into an industrial application will rely on advanced manufacturing methods, and the geometries may be susceptible to clogging. Similarly, the impact of crossflow on performance is not yet understood.

Another method explored by researchers was the use of vortical shedding and fluid-structure interaction from spring supported cylinders or active reeds placed downstream of the jet to induce unsteady oscillations into the jet flow structure, the setup is shown in Figure 2.14 (Haneda et al., 1998; Hidalgo et al., 2010; Hidalgo et al., 2015).

The vortical structure jet interaction augmented heat transfer rate in the wall jet region. Whereas the cylinder obstructed the jet impinging into the stagnation region and deteriorating heat transfer capability. Overall heat transfer enhancement of 20% and higher observed in cylinders, and the use of active reeds lead to a 4x times increase in thermal performance. However, the need for small-scale moving parts limits the

applicability of this technique to harsh industrial environments and gas turbine engines.

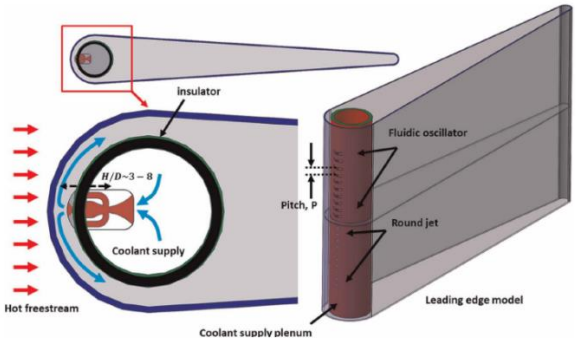

Figure 2.13 Fluidic oscillator in a turbine blade (Hossain et al., 2018)

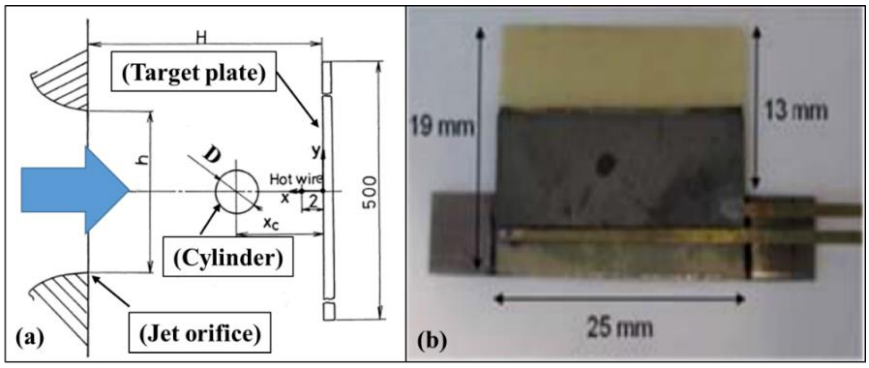

Figure 2.14 Cylinder downstream (a); piezoelectric reed (b)(Hidalgo et al., 2015)

Secondary synthetic jets have been used to impart unsteadiness into a primary jet in different geometrical arrangements for jet vectoring and promote shear layer mixing (Yu et al., 2014; Smith and Glezer, 2005; Chiekh et al., 2011). A maximum of 20% heat transfer enhancement was observed in some configurations, and also results showed deteriorating stagnation region Nusselt number. However, using active synthetic diaphragms in generating the synthetic jet is not a reliable method for harsh industrial application. To eliminate the use of moving parts, some researchers found interest in

utilizing aeroacoustics tones to promote jet instabilities (Page et al., 1995; Arthurs and Ziada, 2012). The nozzle length and jet-plate distance controlled the acoustics driving the jet instabilities. Results concluded that overall heat transfer enhancement in some configurations by 50% and adverse effects were observed for higher jet-plate distance. The sensitivity of this technique makes their industrial application a challenge.

Jet impinging into a rectangular cavity leads to the development of vortical structure due to fluid-wall interaction, and these vortices push the jet in either direction causing jet oscillation (Kalter et al., 2014; Righolt et al., 2015). The PIV results of the jet movement in time for half cycle is shown in *Figure 2.15*. The vortical structures causing the jet oscillation can also be observed near the wall. Several other groups have studied this phenomenon to understand the flow physics of this configuration. However, due to the large jet to plate distance in these works of literature, heat transfer effects were not given importance (Mataoui and Schiestel, 2009; Kolsek et al, 2007; Lawson and Davidson, 2001).

The jet impingement process is a quasi-steady process. Researchers have studied the unsteady flow structures occurring naturally in a jet/ multiple jet impingement process. An unsteady DNS (direct numerical simulation) numerical investigation was carried out on a two-dimensional jet impinging on a target plate and confined by the top wall for a range of Reynolds number, Re = 300 - 1,000 (Chung and Luo, 2002). The scalar flow field is shown in Figure 2.16; as the jet fluid exits the orifice, primary vortices are formed due to shear layer interaction. These primary vortices move downstream, periodically impinging on the target plate, leading to an unsteady Nusselt number in the stagnation region. The interaction of the primary vortex and the wall jet also imparted unsteady

Nusselt number distribution in the wall jet region. The unsteady vortex separation in the wall jet region led to a secondary peak at a higher Reynolds number and lower jet-plate distance.

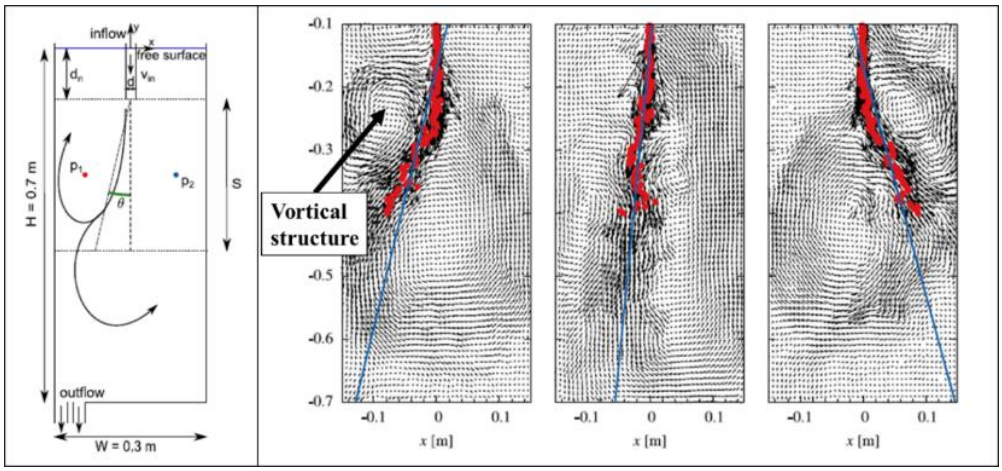

Figure 2.15 PIV contour of jet flow into a cavity (Righolt et al., 2015)

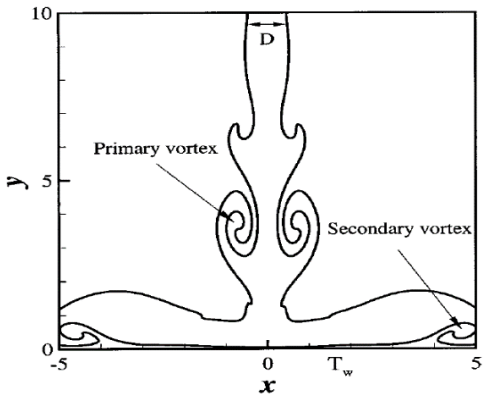

Figure 2.16 Flow features of unsteady jet impingement (Chung and Luo, 2002)

The experimental and numerical investigation comparing steady and unsteady RANS simulation to experimental results was carried out by Yang et al. (2014) for multiple jet impingement channel (*Figure 2.17*). Results show that the unsteady k- ω SST turbulence

model better matches the experimental results than the steady RANS model. Also, unsteady flow features were being developed due to vortical structures generated in the channel. These vortical structures are formed due to the confined channel jet impingement and travel downstream, interacting with the downstream jet imparting additional unsteadiness (Yang et al., 2014).

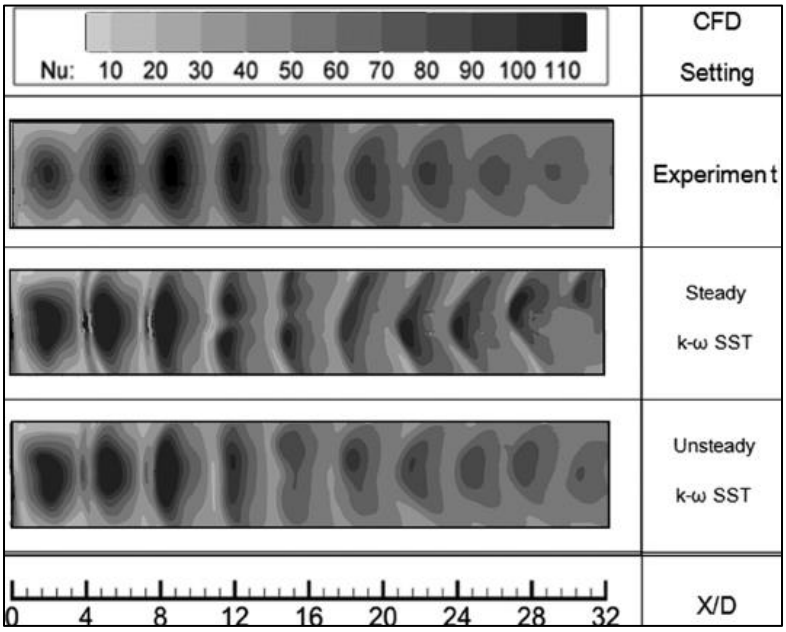

Figure 2.17 Effect of turbulence model on Nu distribution (Yang et al., 2014)

2.4. Unsteady Vortical Structures

The unsteady vortex shedding strength from a cylinder in a flow field is proportional to the flow velocity. The unsteady wake generation stretches in the shear layer transition regime (Re = 1,000 - 200,000), where the Strouhal number is found to be St = 0.2 (Williamson, 1996). The flow physics for finite and infinite length cylinders is different due to the tip vortex protruding into the 2-D vortex shedding from the cylinder. The flow

physics also depends on the blockage ratio, cylinder length, and Reynolds number. The vortex formation length for an infinite cylinder is around two-cylinder diameters from the cylinder center. The formation length is further downstream for a shorter cylinder (FC) and increases with the cylinder height (as shown in Figure 2.18).

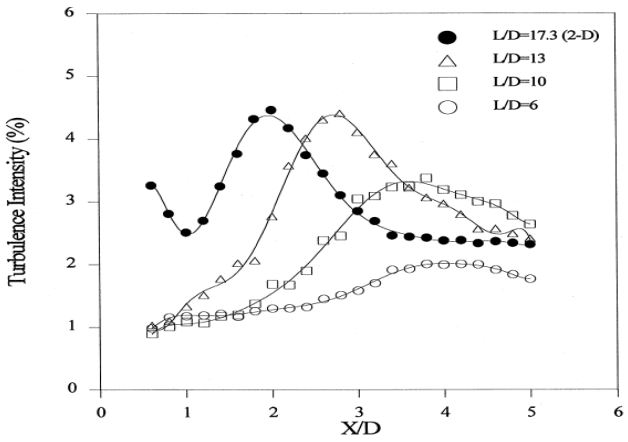

Figure 2.18 TI plot behind a finite/infinite cylinder (Park et al., 2000)

The local maximum of the turbulent kinetic energy behind the cylinder corresponds to the formation length (Park et al., 2000; Giordano et al., 2008). The vortex shedding is symmetric for an FC with an aspect ratio of less than 4 and develops into an asymmetric wake with the increase in aspect ratio (Okamoto et al., 1992).

The flow feature for flow around a cylinder in a confined channel is different from the finite or infinite cylinder case discussed above. The wakes shed from the cylinder interact with the walls to cause further turbulent features downstream. The interaction between the wakes and sidewall leads to a beating effect observed at high blockage ratio ($b>0.5$). The drag coefficient for this case increases with the increase in Reynolds number and the blockage ratio (Griffith et al., 2011; Khan et al., 2004).

The interaction between the jet and the upstream cylinder can be related to the flow features around two cylinders inline. The forces acting on the second cylinder downstream are significantly affected by the spacing between the cylinders. A critical spacing (L/d = 3) below which the shear layer separated from the upstream cylinder attaches to the downstream cylinder, and no wakes are produced. The forces acting on the downstream cylinder beyond this critical spacing fluctuate and reach a maximum value when the wakes generated by each cylinder are in phase (Alam et al., 2003; da Silveria et al., 2005).

A study by Singh et al. (2017), on the combined effect of pin fin and jet impingement in an inline/staggered array arrangement was recently investigated. The literature aimed to protect the jet behind the pin to reduce crossflow effects. Results showed enhancement in heat transfer rates, but the jet was positioned close to the cylinder in the recirculation region. Hence, the literature showed no unsteady jet oscillation.

The literature review shows there is potential for significant gains in heat transfer using oscillating jets. Active and passive jet oscillation techniques exist, but the complexity of an active flow control system inside a gas turbine blade will be a challenge. The suitability of the available active/passive jet oscillation approaches to a harsh industrial environment is limited due to reliability concerns and the expected negative impact of an accumulated crossflow. The purpose of this research is to alleviate the issues associated with implementing a passive jet oscillating technique through the interaction with vortex structures periodically shed from a cylinder placed upstream in the channel with an initial crossflow. These modifications will be readily adapted to the existing designs and will likely benefit from some level of crossflow accumulation.

2.5. Problem Statement and Hypothesis

The industrial application of the existing active and passive jet oscillation techniques is an engineering challenge. Hence, a robust passive jet oscillation technique is in demand due to its enhanced heat transfer rates.

The hypothesis of this study is a novel method to utilize wakes generated from an upstream cylinder in a channel with initial crossflow to impart periodic oscillation into a jet downstream. And, the achieved jet oscillation leads to more uniform/enhanced heat transfer rates on the target plate.

The overall objective of this study is to investigate the flow interaction of an impinging jet with vortex structures periodically shed from a cylinder placed upstream in the channel with an initial crossflow for jet oscillation causing heat transfer enhancement. Further, perform experimental analysis to understand the underlying flow physics causing the jet oscillation and develop an optimum design with correlations. The proposed study is broken down into three phases:

- A response surface sensitivity analysis using unsteady RANS simulations for an oscillating jet through interactions with a cylinder; to prove the above-stated hypothesis and determine the effect of geometrical/flow parameters on the jet oscillation frequency and amplitude. Finally, develop an optimum geometrical design generating effective jet oscillation.
- To experimentally study the effect of the geometrical/ aerodynamic parameters and benchmark the computational results. Finally, decrypt the flow physics of jet-cylinder interaction using tools like unsteady pressure & velocity measurement, and turbulence using hotwire technique.

- Finally, thermal performance comparison of the developed optimum oscillating jet with a non-oscillating jet.

3. Methodology

The current work utilizes both computational and experimental analysis to prove the above-discussed hypothesis and achieve the goal of this study. The primary approach is the initial use of inexpensive CFD analysis to identify the critical geometrical and flow parameters responsible for jet oscillation. Subsequently, design and perform detailed experimental analysis to further study the observed CFD results and cylinder wake-jet flow interaction.

A single confined jet is considered with a cylinder placed upstream in the channel at S from the orifice, as shown in Figure 3.1. The vortex shedding induced by the crossflow around the cylinder interacts with the downstream jet leading to lateral jet oscillation. The turbulent air jet impinges onto the heated surface and removes heat by convection.

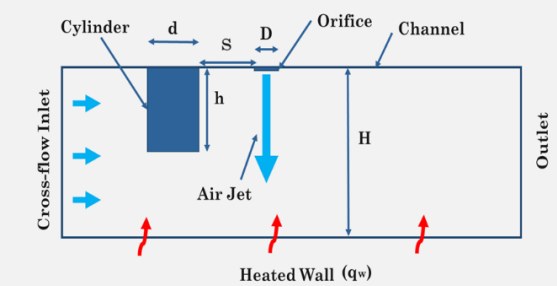

Figure 3.1 Schematic diagram of the setup

Table 3.1

Constant parameters

Parameter	Value
Channel height	H/D = 3
Channel width	W/D = 8
Channel length	L/D = 33.34

3.1. Response Surface Sensitivity Analysis Methodology

For the first phase of this study, a response surface sensitivity analysis is carried out to identify the parameters affecting the oscillation and produce a maximum enhancement in the time-averaged Nusselt number. In this initial phase, assuming momentum required to oscillate the jet is directly proportional to the strength of the cylinder wake. The parameters selected for this initial study are the cylinder diameter (d/D), cylinder height (h/D), and crossflow velocity/ cylinder Reynolds number (Re_{cyl}). In addition, the literature on inline cylinders identified the distance between the cylinders played a significant role in wake generation (Alam et al., 2003; da Silveria et al., 2005). Hence, the effect of cylinder-jet distance (S/D) on jet oscillation is also studied.

A full factorial design of trials for the four parameters with three variations will result in 81 trials. To reduce time and resources, a statistical approach is followed to utilize Box-Behnken Method (BBM) in this study to reduce the number of tests to 25 (Nguyen, 2010). The selected three levels of variables for each parameter are shown in Table 3.2.

Table 3.2

List of varying parameters

Parameter	Value		
	-1	0	1
Cylinder diameter (d/D)	1	2	3
Cylinder height (h/D)	1	2	3
Cylinder Reynolds number (Re_{cyl})	5,000	10,000	15,000

For the jet cylinder distance (S/d), a preliminary study of the cylinder alone in a confined channel is carried out. The cases studied in this preliminary analysis of cylinder

with no jet impingement are shown in Table 3.3. The cylinder diameter is defined as the characteristic length for the crossflow Reynolds number for literature reference. The test matrix is developed using MINITAB software (version 18); the developed test matrix is shown in Table 3.4.

Table 3.3

Preliminary study of the cylinder wake test case matrix

Case	d/D	h/D	Re_{cyl}
0	1	3	5,000
0.1	1	3	15,000
0.2	2	1	10,000
0.3	2	2	10,000
0.4	2	3	5,000
0.5	2	3	10,000
0.6	2	3	15,000
0.7	3	3	10,000

Table 3.4

Test matrix

Case	d/D	h/D	S/d	Re_{cyl}
1	0	1	1	0
2	-1	-1	0	0
3	0	-1	0	-1
4	0	1	0	-1
5	-1	0	0	-1
6	1	0	-1	0
7	-1	0	1	0
8	0	1	0	1
9	-1	0	0	1
10	0	-1	0	1
11	0	0	0	0
12	0	0	-1	1
13	1	0	1	0

14	0	0	-1	-1
15	-1	0	-1	0
16	1	1	0	0
17	0	0	1	-1
18	0	1	-1	0
19	0	-1	-1	0
20	1	0	0	1
21	0	0	1	1
22	1	0	0	-1
23	-1	1	0	0
24	0	-1	1	0
25	1	-1	0	0

3.2. Computational Setup

The computational domain developed for the initial phase is set up similar to the schematic shown above. The initial phase CFD domain used is shown in Figure 3.2. The surfaces featuring the jet orifice and the crossflow inlet are specified velocity inlet conditions. The channel outlet surface is set as a pressure outlet condition. The side walls are set as a periodic interface to simulate an infinite series of parallel domains. The target wall is given a constant heat flux boundary condition. Whereas all other surface faces are set to be an adiabatic wall. A table featuring all the physical properties used in this approach is shown in Table 3.5.

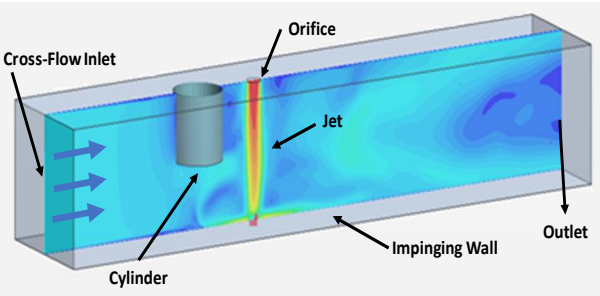

Figure 3.2 Initial phase computational domain

Table 3.5

Initial computational domain physical properties

Description	Value
Atmospheric temperature (K)	$T_\infty = 300$
Atmospheric pressure ($Kgm^{-1}s^{-2}$)	$P_\infty = 101325$
Density of air (kgm^{-3})	$\rho = 1.18415$
Dynamic viscosity of air ($kgm^{-1}s^{-1}$)	$\mu = 1.855X10^{-5}$
Specific heat of air ($JKg^{-1}K^{-1}$)	$c_p = 1003.62$
Temperature of bottom wall (K)	$T_w = 344.9$
Temperature of impinging jet (K)	$T_j = 300$
Thermal conductivity of fluid air ($Wm^{-1}K^{-1}$)	$k_f = 0.0260305$

A second and final computational domain is setup to incorporate the design constraints from the designed experimental rig. The final computational and mesh domain developed is shown in Figure 3.3. The surface featuring the plenum inlet and the crossflow inlet are given mass flow inlet condition. A pressure outlet condition is specified for the channel outlet. The target wall is given a constant heat flux boundary condition. Whereas all other surface faces are set to be an adiabatic wall. The final CFD domain constants are listed in Table 3.6; the viscosity and thermal conductivity are predicted using Sutherland's law using the temperature.

The 3D flow problem is solved using an unsteady k-ω SST turbulence model in a commercial software (STAR-CCM+ version 14.02.01). This model can predict good results for both jet impingement and flow around a cylinder, hence selected (Yang et al., 2014). The target surface Nusselt number is averaged over time, and the final time-averaged Nusselt number is used to compare with experimental results. The simulation is run for a total time, t = 10s, until the time-averaged Nusselt number remained constant over time.

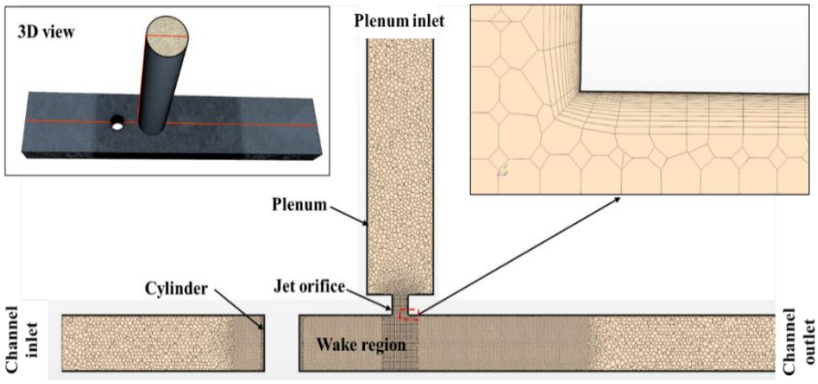

Figure 3.3 Final computational domain

Table 3.6

Final CFD parameters

Description	Value
Atmospheric temperature (K)	$T_\infty = 300$
Atmospheric pressure ($Kgm^{-1}s^{-2}$)	$P_\infty = 101325$
Heat flux supplied to bottom wall (Wm^{-2})	$q_w = 2500$
Temperature of impinging jet (K)	$T_j = 300$

3.2.1. Mesh Independent Study

A mesh independent study is carried out for an oscillating jet case to determine the effect of cell density; three cell counts are analyzed. The geometric and flow characteristic of the selected oscillating jet case are listed in Table 3.7.

The target wall is designed with 25 prism layers and 0.1D prism thickness to maintain a wall y+ < 1, which is an essential requirement for this problem type. A volumetric mesh constraint is used to finely mesh the cylinder's stagnation and wake region downstream (shown in Figure 3.3).

The streamwise average Nusselt number in the stagnation region is used to differentiate the effect of cell size (shown in Figure 3.4). The method of streamwise

averaging will be discussed in detail in the result section. The results show that the curves representing the medium and fine cell size overlap with less than 1% change. Therefore, medium cell size is efficient in producing results with minimum computational cost and time.

Table 3.7

Oscillating jet case parameters.

Parameter	Value
Cylinder diameter	d/D = 2
Cylinder-jet distance	S/d = 3
Velocity ratio	VR = 6
Jet Reynolds Number	Re_j = 38,000

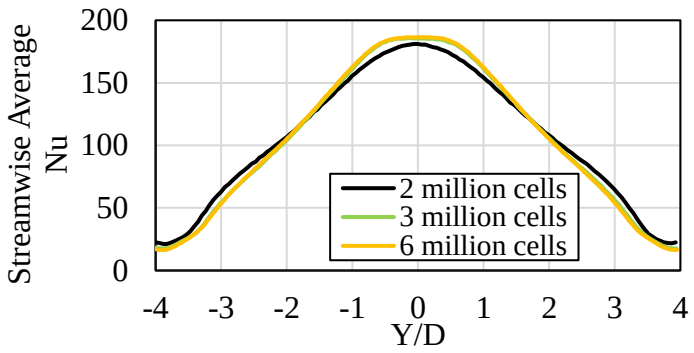

Figure 3.4 Effect of mesh size on streamwise average Nu

As the CFD domain includes a cylinder producing cylinder wakes. The mesh size must not affect the wakes produced. Hence a CFD domain is generated, including only the cylinder diameter (d = 2D) exposed to a crossflow channel Reynolds number, Re = 32,000 . The effect of mesh size on cylinder lift, drag and Strouhal number is also quantified (shown in Table 3.8). A medium cell size of 3 million proved efficient in all

the categories, with a less than 2% change from the results.

Further, the turbulent intensity (TI) behind the cylinder is also compared for different cell sizes shown in Figure 3.5. The curves representing the medium and fine cell size are in close proximity of each other, indicating a minimum change. Summarizing the above results, to reduce computational cost and time. A medium cell size of 3 million is selected to perform the current CFD analysis for all trials efficiently and effectively.

Table 3.8

Mesh independent study

Mesh Cell	Cell Size	Cl_{rms}	% change	Cd_{Avg}	% change	St	% change
Fine	6 Million	0.99	-	1.68	-	0.25	-
Medium	3 Million	1.00	1%	1.67	0%	0.26	2%
Coarse	2 Million	0.96	-3%	1.61	-4%	0.25	0%

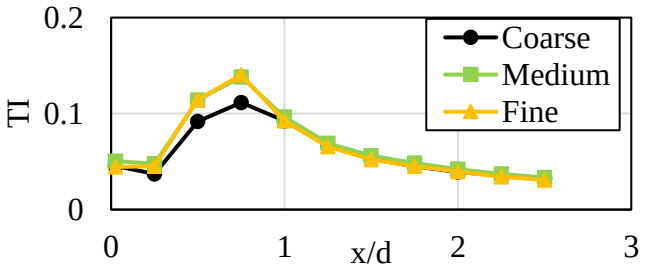

Figure 3.5 Effect of mesh size on Turbulent intensity

3.2.2. Time Step Study

A preeminent parameter defining the accuracy of the simulated cylinder wake amplitude, frequency, and phase is the time step. The time step of an unsteady simulation involving cylinder wake shedding is dependent on the wake frequency. The vortex shedding frequency (*f*) is calculated based on the Strouhal number (*St*) given by,

$$f = \frac{St \times V}{d} \tag{6}$$

Where *V* is the free stream velocity and *d* is the cylinder diameter. The time period (T) of the wake shedding is given by,

$$T = \frac{1}{f} \tag{7}$$

A generalized method defined by the works of literature on cylinder wakes is to determine the time step by dividing the wake time period (*dt*) by a factor of 20 (Equation 8). This leads to the CFD simulation of 20-time steps in between each vortex shedding.

$$dt = \frac{T}{20} \tag{8}$$

Table 3.9

Time step independent study

Time step	Cl_{rms}	% change	Cd_{avg}	% change	St	% change
0.0001	0.834	-	1.684	-	0.259	-
0.0005	0.919	10%	1.718	2%	0.253	-2%
0.001	0.975	17%	1.744	4%	0.253	-2%
0.002	1.151	38%	1.819	8%	0.248	-4%

Substituting the extreme flow and geometric conditions of this current study, the time step can be calculated to be, dt = 0.001 for a Strouhal number, St = 0.21. However, the Strouhal number from the mesh independent study did not match with the literature findings of St = 0.21. Hence, the effect of different time steps on vortex shedding frequency, cylinder lift, and drag is analyzed. The CFD domain considered for this study is similar to the cylinder mesh independent study.

The CFD results listing the cylinder drag/lift and Strouhal number for various time

steps are shown in Table 3.9. The cylinder RMS lift is found to be sensitive to the time step, which represents the wake strength driving jet oscillation. The results show the time step, dt = 0.0005 leads to a minimum percentage change in lift, drag and St assuming the results of time step, dt = 0.0001 as the base. Confined by computational time and cost, a dt = 0.0005 is selected for this current study and held constant for all the trials investigated.

3.2.3. Inner Iteration Study

CFD numerical error comprises rounding error, spatial/time discretization error, and iteration error. The spatial/ time discretization error is minimized by the mesh independent study and time step study. In addition, to minimize iteration error in an unsteady simulation, the following inner iteration study is conducted (Bartesaghi & Columbo, 2013).

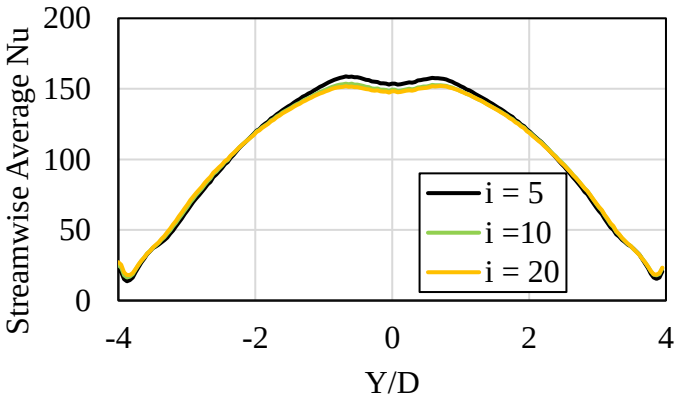

Figure 3.6 Effect of inner iteration on streamwise average Nu

To investigate the effect of inner iteration, the CFD domain of the oscillating jet case from the mesh independent study is utilized. The inner iteration analysis is performed

similar to the literature work of Bartesaghi and Columbo (2013); the inner iteration tested are i = 5, 10, and 20. Figure 3.6 shows that the inner iteration, i = 10 is sufficient in predicting results close to inner iteration, i = 20. Hence, for the current CFD analysis, an inner iteration of i = 10 is selected to perform all other trials.

3.3. Experimental Setup

The experimental setup designed for this study is shown in Figure 3.7. For the initial frequency analysis, a compressor and a rotameter are used to generate and measure the jet orifice flow. Later on, to investigate higher jet Reynolds numbers, a blower is used to generate the necessary upstream driving pressure. The flow through the jet orifice is forced through a settling chamber and flow conditioner to reduce turbulence. The setup also includes another blower working under suction at the outlet to generate the crossflow velocity. The flow through the blower is measured using an adjacent inline venturi meter. The open-loop channel also contains a bypass valve near the downstream blower to regulate the flow through the channel.

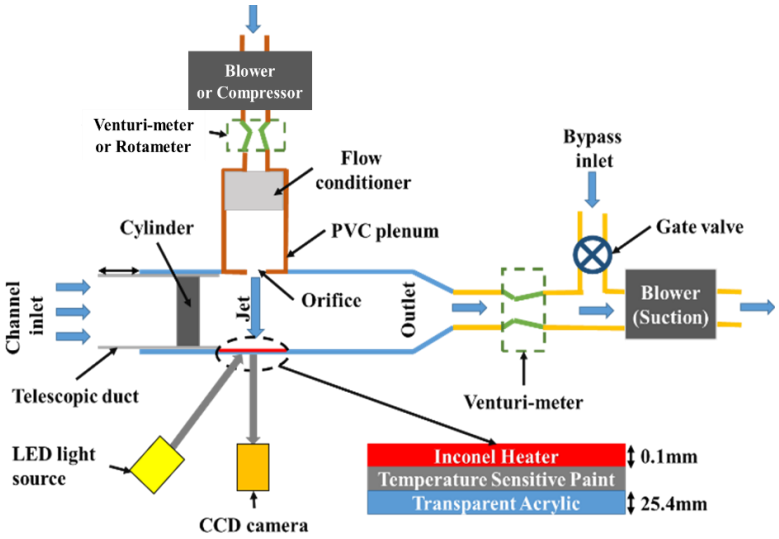

Figure 3.7 Schematic of experimental setup

The designed experimental rig for the initial frequency analysis is shown in Figure 3.8. The cylinder-jet distance (S/d) is varied by placing the cylinder inside a thin rectangular sheet metal duct that slides inside the channel (telescopic duct shown in Figure 3.9). The duct also maintains a constant cylinder-inlet distance of 13 jet diameters.

Figure 3.8 Initial experimental rig

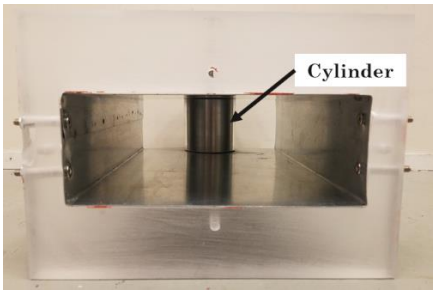

Figure 3.9 Telescopic duct front-view

The experimental investigation aims to collect the unsteady time-averaged Nusselt number of a laterally oscillating jet. A schematic of the setup used to collect temperature measurement is shown in Figure 3.10. The target surface is painted utilizing a Temperature Sensitive Paint (TSP) to measure the local temperature. The Inconel heater is attached to the target surface using high-temperature adhesive tape. The resistive

Inconel heater is heated using an external electrical source. The internally generated heat flux ($q_{supplied}$) is convected by the oscillating jet. A part of this thermal energy (q_{loss}) is lost through the acrylic plate, driven by the temperature difference on either side of the acrylic plate.

The thermal conductivity of the double-sided tape is k = 0.46 W/mK, and the thickness of the tape is t = 0.004inch (0.1mm), leading to a negligible amount of resistance compared to the heat flux transferred through it. The TSP is excited using an LED excitation source to the required wavelength (490 nm), and data from the excited TSP is collected using a CCD camera. The measured heat flux and temperature can be deduced to determine the Nusselt number, using Newton's law of cooling. A detailed explanation of the data reduction process to derive the Nusselt number is discussed later on under the data reduction subchapter.

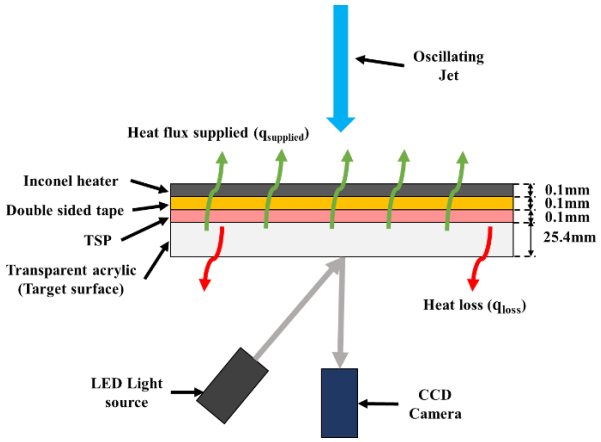

Figure 3.10 Schematic setup to measure temperature using TSP

The impinging surface is a low thermal capacity material to minimize fast dissipation of the oscillating jet stagnation region. A low thermal conductivity 1” transparent acrylic

sheet is used to build the entire channel, including the target wall. The area of interest on the target surface (10 X 8 inches in dimension) is heated electrically using Inconel heater strips connected in series (Figure 3.11). The Inconel strip is of a thickness of 0.004inch (0.1mm) with thermal conductivity of 11.2 W/mK. The strips are laid out in the streamwise direction, separated by a small gap connected in series. The temperature data collected in this gap is rejected as there is no heat flux supplied. Also, the Inconel heater is fabricated inhouse using a spot welder, hence the strip junction data is corrupted (0.59 inch) on either edge, as shown in Figure 3.11.

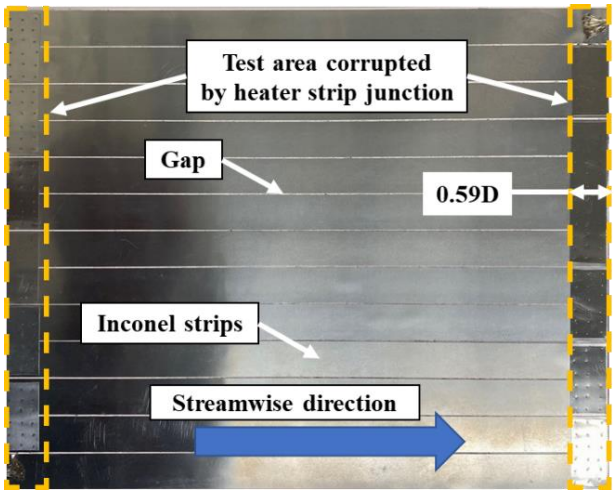

Figure 3.11 Inconel heat strip

3.3.1. Heat Leakage Test

As discussed above, constant heat flux is supplied to the target surface through the Inconel heater. A part of the heat flux is lost through the bottom surface into the surrounding atmosphere (as shown in Figure 3.10). The heat lost should be quantified to determine the heat transfer coefficient accurately. The heat flux lost (q''_{loss}) is

proportional to the temperature difference between the top surface and the surrounding room temperature.

$$q''_{loss} \; \alpha \; \Delta T \tag{9}$$

A heat leakage test is conducted to determine the constant in the above Equation 9. The top surface of the Inconel heater is covered by a thick layer of fiberglass insulation material. The insulation leads to an assumption of no heat leakage from the top surface. Hence the heat flux supplied through the Inconel heater will be equal to the heat flux through the bottom surface, as shown in Figure 3.12.

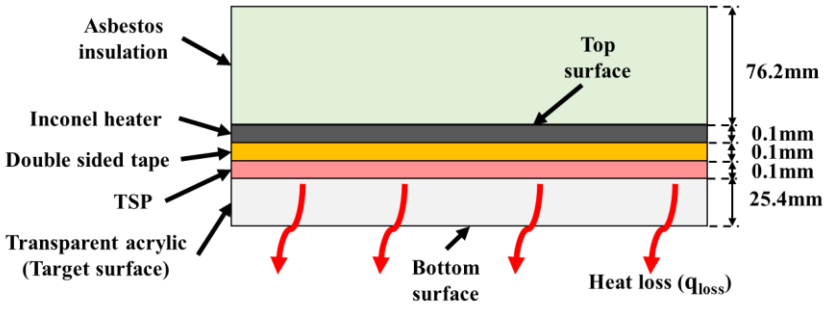

Figure 3.12 Schematic setup of heat leakage test

The temperature of the top surface and room atmosphere is measured using a type-T thermocouple. The heat flux supplied is varied to determine the temperature difference ((ΔT) on heat flux lost (q''_{loss}). The literature of Prasad (2021) followed the same experiment hence its results from the heat leakage study is shown in Figure 3.13. The heat loss is found to be directly proportional to the temperature difference between the wall and room temperature. Hence, the curve is simulated using the straight-line Equation 10 shown below.

$$q''_{loss} = 6.31442 * \Delta T \quad (10)$$

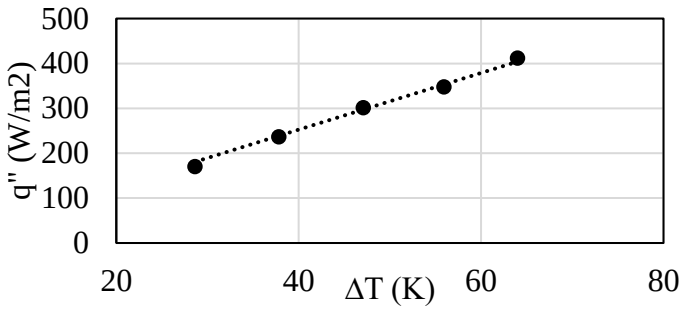

Figure 3.13 Heat leakage test result (Prasad, 2021)

3.3.2. Temperature Sensitive Paint (TSP)

The temperature-sensitive paint is used to measure the local surface temperature and eliminates the use of numerous thermocouples. A TSP constitutes luminescent molecules in a transparent polymer binder. A typical arrangement of the TSP measurement system is the TSP painted surface, excitation light source, and a digital camera.

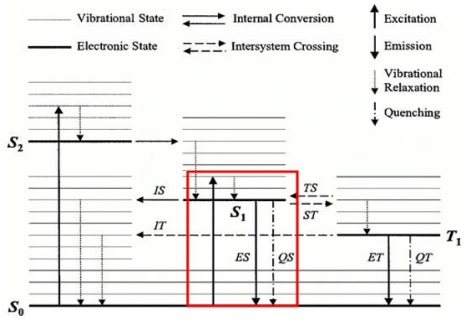

Figure 3.14 Jablonski diagram (Bell et al., 2001)

The luminescence process of the TSP molecules through different energy states is shown in the Jablonski diagram (Figure 3.14). Initially, the TSP is excited by a light

source to the required excitation wavelength, and the excited molecules are now at a higher energy state (S2). These molecules are unstable and return to the ground state (S0) either by luminescence emitting photons (emission wavelength) or thermal quenching. Thermal quenching is caused by the change in temperature of the TSP surface; an increase in temperature decreases the photons emitted by the TSP. The number of photons emitted is directly proportional to the intensity of the TSP surface. Hence, the increase in surface temperature leads to a decrease in TSP intensity.

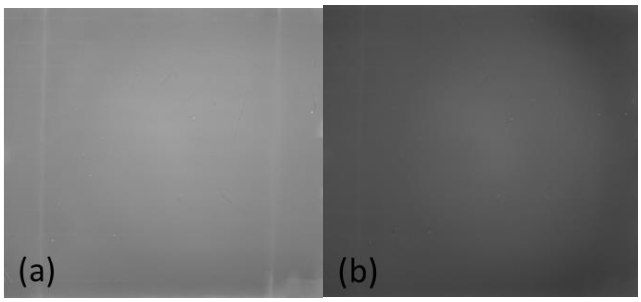

Figure 3.15 Reference image (a) and data image (b)

The excited TSP at room temperature with higher intensity is showed in the reference image (Figure 3.15a). The local TSP temperature is assumed to be constant, and multiple thermocouples are used to measure the reference temperature. Later on, running the experiment, a heated data image is captured (Figure 3.15b). The data image intensity is observed to be reduced due to the temperature rise. The local temperature of the data image can be calculated using the change in intensity ratio (*IR*).

$$IR = \frac{I_S}{I_{ref}} \tag{11}$$

Where I_s is the data image intensity and I_{ref} is the reference image intensity.

The TSP should be calibrated to determine the effect of the intensity ratio on the temperature change. The calibration setup consists of a small test coupon with TSP on one side. The test coupon is heated electrically in an insulated environment to a uniform temperature. The temperature of the test coupon is measured using multiple thermocouples. The TSP intensity is captured using the CMOS camera discussed above. Multiple TSP measurements are carried out at different temperatures to derive the calibration curve (intensity ratio versus temperature difference) shown in Figure 3.16. The same TSP paint from the literature work of Prasad (2021) is utilized in this current study. Hence the same calibration equation (Equation 12) is used to calculate the data surface temperature.

$$\frac{T_S - T_{ref}}{100} = 2.52\,IR^4 - 8.3\,IR^3 + 10.18\,IR^2 - 6.24\,IR + 1.85 \qquad (12)$$

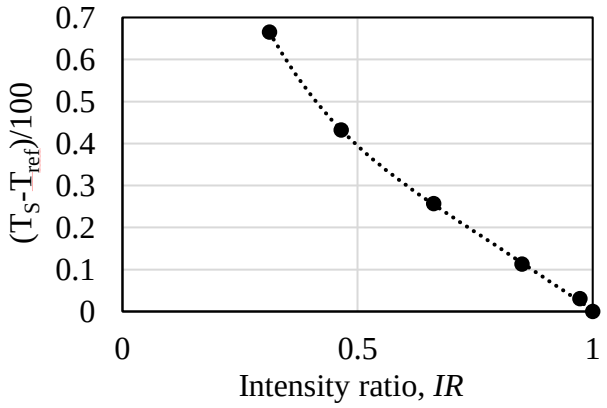

Figure 3.16 Calibration of TSP, Prasad (2021)

The TSP utilized in this current research is ISSI UniCoat TSP; the manufacturer specification is shown in Table 3.10. An LED excitation source is used to excite the TSP to the required excitation wavelength of 400 nm. A scientific-grade CMOS camera with a

550 nm filter is used to capture the emitting wavelength and the intensity of the TSP paint. The uncertainty analysis of the TSP was carried out by Liu et al. (2006), results showed a maximum error of ±0.93 ºCelsius for a temperature range of 20-70 ºCelsius.

Table 3.10

ISSI UniCoat TSP specifications

Parameter	Value
Pressure sensitivity	0.0% per kPa
Pressure range	1-kPa to 10-MPa
Temperature sensitivity	0.9% per °C
Temperature range	10°C to 80°C
Response time	750 ms
Excitation wavelength	380 – 520 nm (460 nm ideal)
Emission wavelength	500 – 720 nm
Photo-degradation rate	1% per hour (Excitation)
Filter	550 nm

3.4. Constant Temperature Anemometry

A constant temperature hotwire anemometer is used to measure the velocity magnitude and fluctuation in a flow field. A hotwire works on the principle of the sensor heat transfer rate being proportional to the flow velocity. The hot wire is used to measure the downstream turbulence effect of a cylinder in a channel (shown in Figure 3.17). The local velocity behind the cylinder is measured at various distances (S/d), similar to the literature work of Park et al (2000). The velocity fluctuation is used to derive the turbulence intensity behind the cylinder, the detailed process of TI calculation is discussed in the data reduction section. The cylinder vortex shedding frequency is calculated by spectral analysis of the measured velocity fluctuations. The sampling

frequency of f_s = 1666Hz is selected for this study which satisfies the Nyquist criteria.

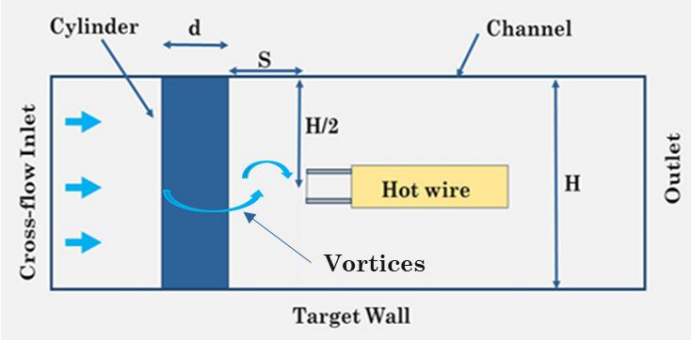

Figure 3.17 Schematic of hotwire measurement

The hotwire utilized in this study is a 5-micron single-strand tungsten-wire, shown in Figure 3.18. The tungsten wire is heated to 200 ºCelsius electrically by Joule heating, and the resistance of the hotwire is continuously monitored using a Wheatstone bridge. However, by heat transfer, the velocity fluctuations try to impose a temperature change. A servo amplifier maintains the temperature of the tungsten wire constant by varying the current through the sensor. Hence, the measured bridge voltage is directly proportional to the velocity fluctuations.

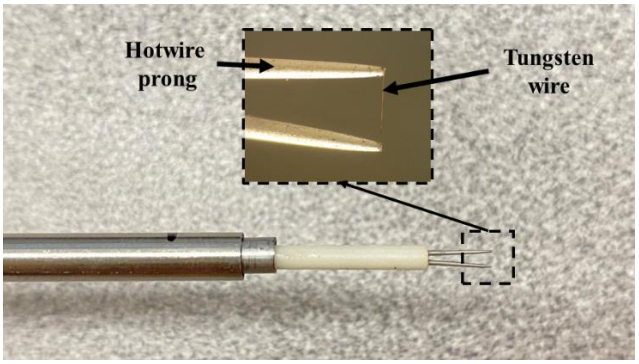

Figure 3.18 Single strand hotwire probe

The hotwire should be calibrated before and after each day experiment to maintain accuracy. The calibration of a hot wire is performed by placing the hot wire in the jet core of an isentropic nozzle. The velocity of the jet is proportional to the chamber pressure, derived from the isentropic equation below,

$$\frac{P_0}{P_\infty} = \left(1 + \frac{\gamma - 1}{2} {M_\infty}^2\right)^{\frac{\gamma}{(\gamma-1)}} \tag{13}$$

Where P_0 is the chamber pressure, P_∞ is the atmospheric pressure, γ is the specific heat ratio, and $M\infty$ the Mach number at the jet exit. Equation 13 can be rearranged to determine the jet Mach number. Finally, the jet velocity can be calculated using the Mach number using Equation 14.

$$V_\infty = M_\infty \sqrt{\gamma R T_\infty} \tag{14}$$

Where T_∞ is the atmospheric temperature.

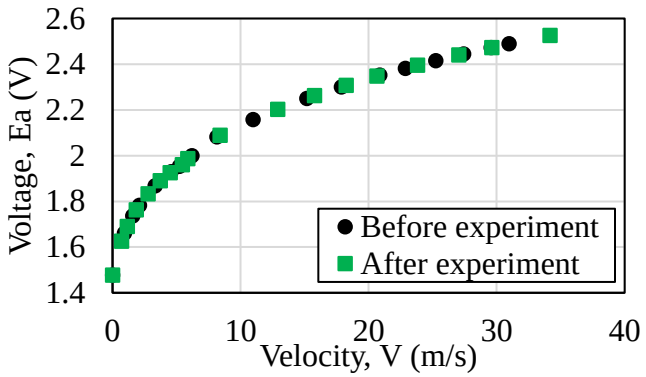

Figure 3.19 A typical hotwire calibration curve

The calibration experiment is performed to determine the effect of velocity on the hotwire bridge voltage. The calibration curve (velocity versus voltage measured) generated before and after a particular experiment is shown in Figure 3.19. The jet

temperature (T_a) and the room temperature (T_0) will also affect the accuracy of the hotwire measurement system; hence it is to be corrected. The equation used to correct the measured bridge voltage (E_a) is shown below,

$$E_{corr} = \sqrt{\frac{T_w - T_0}{T_w - T_a}} \times E_a \tag{15}$$

The corrected voltage (E_{corr}) and corresponding velocity (V) is used to generate the algebraic calibration equation shown below,

$$V = C_0 + C_1 E_{corr} + C_2 {E_{corr}}^2 + C_3 {E_{corr}}^3 + C_4 {E_{corr}}^4 \tag{16}$$

3.5. Pressure Transducers

A typical jet oscillation will lead to an oscillating stagnation region. Hence, a miniature pressure sensor is placed in the stagnation region to measure pressure fluctuation. The pressure probe is dislocated away from the stagnation point by 0.6D (10mm) downstream to account for the crossflow effect on the jet (shown in Figure 3.20). The pressure fluctuations measured will be utilized to calculate the oscillating jet frequency. The pressure probe will also measure the cylinder wake shedding frequency. Analyzing the measured frequency spectrum will help to differentiate oscillating and non-oscillating jets.

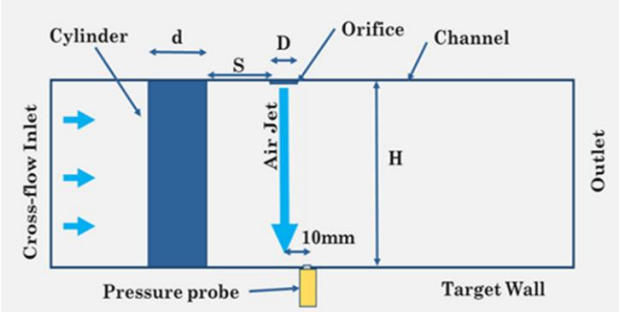

Figure 3.20 Schematic of pressure measurement

3.6. Data Reduction

In this subsection the data reduction process of all the calculated values are discussed below. However, additional data reduction processes of other parameters are discussed in the result section, for ease of explanation.

3.6.1. Nusselt number

The heat transfer experiment aims to measure the local Nusselt number from the TSP surface temperature measurement. Firstly, the supplied heat flux (q''_{sup}) through the Inconel heater strips is calculated using Equation 17 by measuring the current (I) flowing through the heater strip using a shunt resistor in series. The effective heat flux (q''_{eff}) flowing through the test specimen is given by Equation 18.

$$q''_{sup} = \frac{I^2 \rho}{w^2 t} \tag{17}$$

$$q''_{eff} = q''_{sup} - q''_{loss} \tag{18}$$

Where ρ is the Inconel strip resistivity, w is the Inconel strip width, t is the Inconel strip thickness, and q''_{loss} is the heat leaked through the acrylic plate. Newton's law of cooling defines heat transfer coefficient (h) as the ratio of effective heat flux to wall-jet temperature difference (Equation 19). The local heat transfer coefficient is calculated from the TSP surface temperature (T_s) measurement. Finally, the local Nusselt number (Nu) is computed using the HTC (h) and the jet orifice diameter (D) from Equation 20.

$$h = \frac{q''_{eff}}{(T_s - T_j)} \tag{19}$$

$$Nu = \frac{h\,D}{k} \tag{20}$$

Where T_j is the jet temperature, and k is the thermal conductivity.

3.6.2. Reynolds Number and Velocity ratio

The mass flow rate through the jet orifice is measured using a venturi meter or rotameter. The total mass flow rate through the jet orifice and channel inlet is measured downstream using a venturi meter. The flow rate through the channel inlet can be calculated using the difference, Equation 21.

$$\dot{m}_{\text{channel inlet}} = \dot{m}_{\text{channel outlet}} - \dot{m}_{\text{jet orifice}} \tag{21}$$

The jet velocity (V_{jet}) and jet Reynolds number (Re_j) is calculated using the equations below,

$$V_{\text{jet}} = \frac{\dot{m}_{\text{jet}}}{A_{\text{jet}}} \tag{22}$$

$$\text{Re}_{\text{jet}} = \frac{D\ \dot{m}_{\text{jet}}}{\mu\ A_{\text{jet}}} \tag{23}$$

Where A_{jet} is the jet orifice cross-sectional area, and μ is the jet fluid viscosity. The channel velocity (V_{ch}) and jet-crossflow velocity ratio (VR) is calculated using the equations below,

$$V_{\text{ch}} = \frac{\dot{m}_{\text{channel inlet}}}{A_{ch}} \tag{24}$$

$$VR = \frac{V_{\text{jet}}}{V_{\text{ch}}} \tag{25}$$

Where A_{ch} is the channel cross-sectional area.

3.6.3. Turbulence Intensity

The local velocity behind the cylinder is measured using the hotwire anemometer in time. The time-averaged mean velocity (U_{mean}) is given by Equation 26.

$$U_{mean} = \frac{1}{N}\sum_{1}^{N} U_i \tag{26}$$

Where N is the sample size and U_i is the measured local velocity. The root mean square velocity (U_{rms}) is calculated using the Equation 27 below. Finally, the turbulent intensity (TI) can be calculated using Equation 28.

$$U_{rms} = \sqrt{\frac{1}{N-1}\sum_{1}^{N}(U_i - U_{mean})^2} \tag{27}$$

$$TI = \frac{U_{rms}}{U_{mean}} \tag{28}$$

3.6.4. Uncertainty Analysis

The uncertainty of the experimental result is calculated using the root sum square method. Consider an expression where y is a function dependent on x, and y represents one experimental result term. Assuming the function y to be a straight-line equation with slope, m (Prasad, 2016).

$$y = mx \tag{29}$$

The uncertainty (u_y) can be derived as a function of bias/systematic uncertainty (b) and random uncertainty (S) of the result (y), shown in the equation below. Also, the root sum square method propagates the error from all the dependent and independent variables.

$$u_y = \sqrt{\left(\frac{\partial y}{\partial m} * b_m\right)^2 + \left(\frac{\partial y}{\partial x} * b_x\right)^2 + \left(\frac{\partial y}{\partial m} * S_m\right)^2 + \left(\frac{\partial y}{\partial x} * S_x\right)^2} \tag{30}$$

The systematic uncertainty is the RMS sum of all the errors generated by the measuring devices utilized (Equation 31). The random uncertainty represents the

precision and repeatability of the measurement. The random uncertainty is determined by performing multiple experimental measurements. The standard deviation (σ_x) of the measurement is used to calculate the random uncertainty (S_x).

$$B_x = \sqrt{{e_1}^2 + {e_2}^2 \ldots\ldots + {e_n}^2} \quad (31)$$

$$S_x = \frac{\sigma_x}{\sqrt{N}} \quad (32)$$

Where *e1, e2……en* are the bias errors and N is the sample size. The uncertainty (uy) is factored in by a constant (t_{95}) to produce a 95% confidence level in the result. The constant (t_{95}) is determined from the student t distribution table for the sample size (N) selected. In this current study, the sample is five, and the corresponding constant, t_{95} = 2.164. Also, the t_{95} constant affects only random error; hence the bias uncertainty is divided by the constant, t_{95} (Equation 33). Finally, the uncertainty (U_y) with 95 % confidence level is given by Equation 34

$$b_x = \frac{B_x}{t_{95}} \quad (33)$$

$$U_y = t_{95} \times u_y \quad (34)$$

4. Results

The result section has been split into four sections. The first subsection will discuss the preliminary response surface CFD results and prove the current research hypothesis. The second subsection will discuss the flow feature analysis of the jet cylinder-wake interaction. Lastly, the final CFD and experimental results subsections will discuss the optimum design for maximum heat transfer rate.

4.1. Preliminary Response Surface Study

The hypothesis of this study is to utilize the cylinder wake to oscillate the jet laterally in the y-direction. The response surface sensitivity analysis is carried out to identify the parameters affecting the oscillation and produce a maximum enhancement in the time-averaged Nusselt number. The parameters selected for this initial study are the cylinder diameter (d/D), cylinder height (h/D), cylinder-jet distance (S/d), and crossflow velocity/ cylinder Reynolds number (Re_{cyl}). A Box-Behnken Method (BBM) is utilized in this study to reduce the number of tests to 25; the test matrix is shown in Table 3.4.

4.1.1. Initial Cylinder Wake Analysis Result

The jet cylinder distance (S/d) is an essential characteristic of the sensitivity study. To perform the response surface analysis, three levels of variable are to be selected for the cylinder-jet distance. Hence, a preliminary study of just the cylinder in the confined channel is carried out. The cases studied in this initial analysis are shown in Table 3.3.

The literature study shows that the jet should be placed in front of the wake formation length (S/d = 2) to prevent shear layer reattachment. The shear layer from the cylinder separates from the recirculation region moving downstream for a maximum deflection, and this maximum deflection is proportional to the maximum lift coefficient. Hence, the

lift coefficient is a direct measure of momentum generated for jet oscillation. The equation used in this analysis defining the non-dimensional lift coefficient (Cl) is shown in Equation 35.

$$Cl = \frac{L}{\frac{1}{2}\rho {U_\infty}^2 hd} \tag{35}$$

Where L is the lift force, d is the cylinder diameter, h is the cylinder height, ρ is the fluid density, and U_∞ is the channel inlet velocity.

The time period of one oscillation of the lift coefficient curve can be defined as the unit cycle time (t_p), used to calculate the non-dimensional time (t/t_p). The time-resolved lift coefficient is shown in Figure 4.1 for Case 0.5. The corresponding wake profile at peak amplitude is shown in Figure 4.2 using the turbulent kinetic energy, for Case 0.5. For the cylinder height, h/d = 3, the TKE at the mid cylinder height is considered for jet deflection measurement. In the case of short cylinders to avoid tip vortex interference, the TKE at height, h/d = 0.13, is considered for jet deflection measurement.

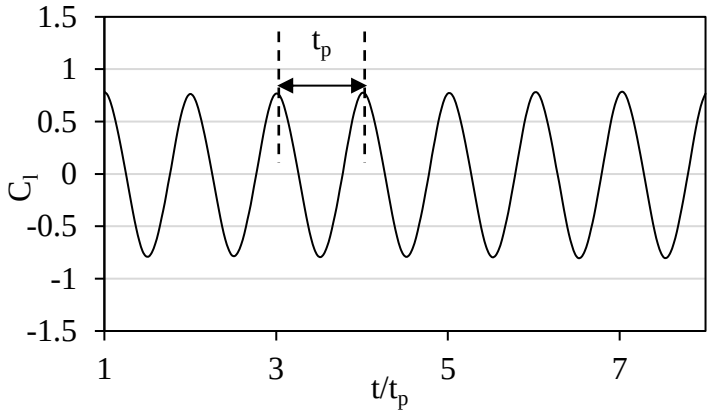

Figure 4.1 Lift coefficient for Case 0.5

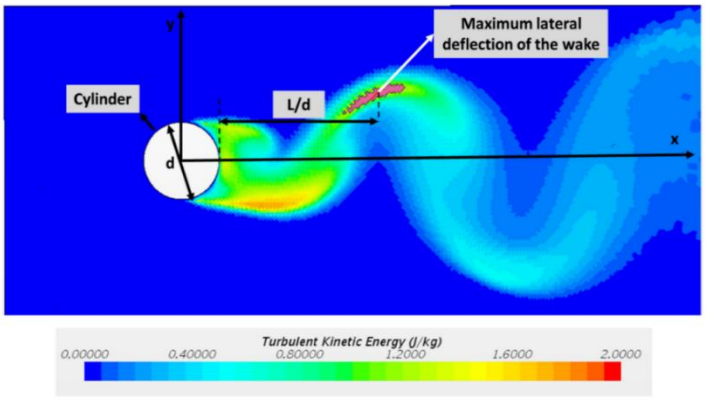

Figure 4.2 TKE showing the wake deflection at peak amplitude for Case 0.5

The corresponding horizontal length between the maximum lateral deflection and the cylinder is measured. The cylinder-jet distance at maximum wake deflection for different cases investigated is listed in Table 4.1. The measured maximum deflection for each case is found to be close to two diameters. Therefore, the jet is placed at this point for maximum deflection. However, the corresponding point is still in the region where the shear layer detached from the cylinder can reattach to the jet, as stated in the literature (Alam et al., 2003; da Silveria et al., 2005).

Table 4.1

The cylinder-jet distance for maximum wake deflection

Case	S/d
0	2.18
0.1	2.16
0.2	2.13
0.3	2.13
0.4	2.1
0.5	2.03
0.6	1.83
0.7	1.955

In this current study, the jet is deflected in the downstream direction from the original position due to the crossflow. Hence the cylinder-jet distance for the following sensitivity study is S/d = 2d, 3d, and 4d. To be noted, the distance between the jet and the cylinder is non-dimensionalized by the cylinder diameter. The table showing the final three levels of variation for the parameters studied in the response surface analysis is listed in Table 4.2.

Table 4.2

The three level of variation of parameter for response surface

Parameter	Value		
	-1	0	1
Cylinder diameter (d/D)	1	2	3
Cylinder height (h/D)	1	2	3
Cylinder Reynolds number (Re_{cyl})	5,000	10,000	15,000
Jet-cylinder distance (S/d)	2	3	4

4.1.2. Jet Core Oscillation Result

The 25 cases investigated resulted in only two cases leading to jet oscillation. The lateral position of the oscillating jet velocity core is tracked in time at a plane 1/3D above the target plate (shown in Figure 4.3). The maximum lateral jet deflection (y/D) of the jet core for Case 8 at a peak amplitude is shown in Figure 4.3. It can be observed that the vortex which caused the jet core deflection towards the top has travelled downstream, and the vortex in front of the jet core is ready to push the jet downwards as it passes around the jet. The physics of the vortex interaction with the jet will be discussed in detail later on.

The lateral position of the jet core (s/D) and the cylinder lift coefficient plotted versus time for Case 8 are shown in Figure 4.4. It can also be observed that the cycle time for

the lift coefficient curve and the jet core position oscillation are equal; therefore, "t_0" represents the time period of the jet position curve. The time taken for one jet oscillation is equal to t_0 = 0.0225s; the maximum lateral oscillation of the jet core is s/D = 1.94. In Figure 4.4, the two waves are out of phase by $0.5t_0$; this is the time taken for the wake shedding from the cylinder to interact with the jet core. The peak magnitude of the jet core position curve fluctuates due to the jet core stretching when in contact with high-energy crossflow. Also, the cylinder wake interaction induces a twisting motion into the jet core. Although the core position curve possesses unsteadiness in magnitude, the frequency of both the waves are equal in magnitude, f = 44.4Hz.

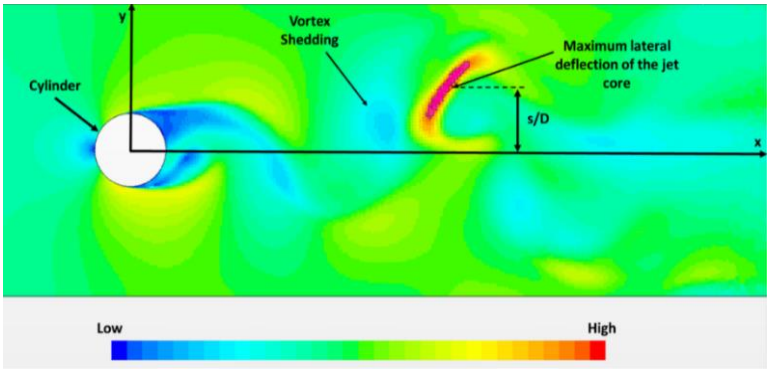

Figure 4.3 Velocity profile showing maximum jet deflection at peak amplitude

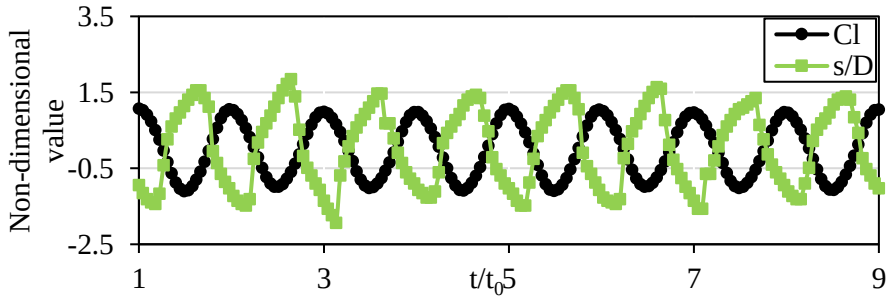

Figure 4.4 Lift coefficient and the jet core position versus time, for Case 8

To compare the jet core oscillation for Case 1 and 8, the jet core position is plotted in time for the two cases (Figure 4.5). The cycle time for Case 1 and Case 8 is t_p = 0.0287s and t_p = 0.0225s respectively; the frequency for Case 1 and Case 8 is f = 34.48Hz and f = 44.44Hz respectively. The Case 1 curve exhibits a smooth change in slope compared to Case 8, and Case 8 exhibit a higher slope at the peak of the waveform. It can be observed that the curve slope changes at y/D = 1, this is due to the jet moving away from the path behind the cylinder into the higher crossflow region. Due to the higher crossflow Reynolds number, the jet position curve amplitude of Case 8 is higher than Case 1.

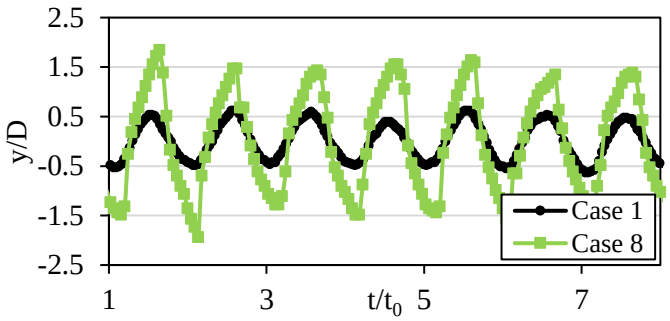

Figure 4.5 Jet core position versus time, for Case 1 and 8

4.1.3. Statistical Analysis Result

For the 25 cases investigated, jet oscillation occurred only in two cases (Case 1 and 8). Hence the jet oscillation is extremely sensitive to the parameters studied. Also, the combination of the parameters studied is an essential characteristic of jet oscillation. The statistical analysis of the results is carried out in Minitab software. The average Nusselt number and the uniform distribution of the local Nusselt number are proportional to the jet oscillation and its frequency (Raman and Cornelius, 1995; Camci and Herr, 2002). Hence, the two-parameter considered for the sensitivity study are the maximum lateral jet

oscillation and the frequency.

Table 4.3

Maximum jet deflection and frequency for oscillating cases

Case	Maximum jet deflection (s/D)	Frequency (f)
1	1.038	34.8432
8	1.9413	44.44

$$\left\{\left(\frac{S}{D}\right) \text{ or } f\right\} = \beta_0 + \left[\beta_1\left(\frac{d}{D}\right) + \beta_2\left(\frac{h}{D}\right) + \beta_3\left(\frac{L}{d}\right) + \beta_4\left(Re_{cyl}\right)\right] + \left[\beta_{11}\left(\frac{d}{D}\right)^2 + \beta_{22}\left(\frac{h}{D}\right)^2 + \beta_{33}\left(\frac{L}{d}\right)^2 + \beta_{44}\left(Re_{cyl}\right)^2\right] + \left[\beta_{12}\left(\frac{d}{D}\right)\left(\frac{h}{D}\right) + \beta_{13}\left(\frac{d}{D}\right)\left(\frac{L}{d}\right) + \beta_{14}\left(\frac{d}{D}\right)\left(Re_{cyl}\right) + \beta_{23}\left(\frac{h}{D}\right)\left(\frac{L}{d}\right) + \beta_{24}\left(\frac{h}{D}\right)\left(Re_{cyl}\right) + \beta_{34}\left(\frac{L}{d}\right)\left(Re_{cyl}\right)\right] \quad (36)$$

Table 4.4

Percentage contribution of coefficients in the correlation above

Term	Coefficients	Maximum Jet deflection (s/D)		Frequency (f)	
		Values	Contribution (%)	Values	Contribution (%)
Constant	β_0	0	0.00	0	0.00
(d/D)	β_1	0	0.00	0	0.00
(h/D)	β_2	0.22167	22.17	6.6067	16.52
(S/d)	β_3	0.06	6.00	2.9036	7.26
Re_{cyl}	β_4	0.1617	16.17	3.7033	9.26
(d/D) ×(d/D)	β_{11}	-0.1108	-11.08	-3.3033	-8.26
(h/D) ×(h/D)	β_{22}	0.2217	22.17	6.6067	16.52

(S/d) ×(S/d)	β_{33}	-0.0208	-2.08	1.0517	2.63
Re_{cyl} ×Re_{cyl}	β_{44}	0.1317	13.17	2.2517	5.63
(d/D) ×(h/D)	β_{12}	0	0.00	0	0.00
(d/D) ×(S/d)	β_{13}	0	0.00	0	0.00
(d/D) ×(Re_{cyl})	β_{14}	0	0.00	0	0.00
(h/D) ×(S/d)	β_{23}	0.18	18.00	8.71	21.78
(h/D) ×(Re_{cyl})	β_{24}	0.485	48.50	11.11	27.78
(S/d) ×Re_{cyl}	β_{34}	0	0.00	0	0.00
		Summation	100		100

The maximum deflection of the jet and jet oscillation frequency for the oscillating cases are determined and listed in Table 4.3; for other non-oscillating cases, the maximum deflection and frequency is zero. The correlation developed for the two parameters is shown in Equation 36; the corresponding coefficients for the two parameters are shown in Table 4.4

From Table 4.4, the critical factors (maximum contribution percentage) responsible for the jet-core oscillation are the height of the cylinder (h/D), the position of the jet (S/d), and crossflow Reynolds number (Re_{cyl}); the major contributor being the height of the cylinder. The maximum cylinder height is equal to the channel height. Hence, the channel height is also a vital characteristic to be studied in the future. Furthermore, the term "(h/D) × (Re_{cyl})" having the highest contribution describes that the height and the crossflow Reynolds number of the cylinder have a coupled effect on the jet oscillation characteristic; this term is directly proportional to the vortex strength generated by the cylinder (Williamson, 1996).

The jet is oscillating for only two cases whereas stationary for all other cases. It is found that all different combinations investigated led to the reattachment of the shear layer separated from the cylinder onto the jet, shown in Figure 4.6 (Case 23). The other

factor causing the adverse effect is the cylinder height (h/D). From the statistical results, the jet is oscillating only for the full cylinder or (h/D) = 3. For the (h/D) < 3, the tip vortex protrudes into the low-pressure recirculation region behind the cylinder decreasing the cylinder wake effectiveness (shown in Figure 4.7). It can also be observed that the upstream wall jet facilitates this protrusion of the tip vortex into the recirculation region.

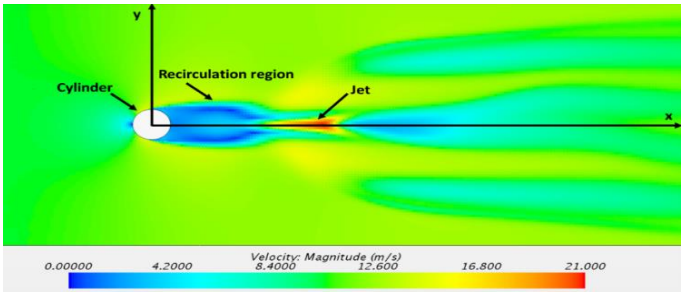

Figure 4.6 Velocity profile of stationary jet in recirculation region for Case 23

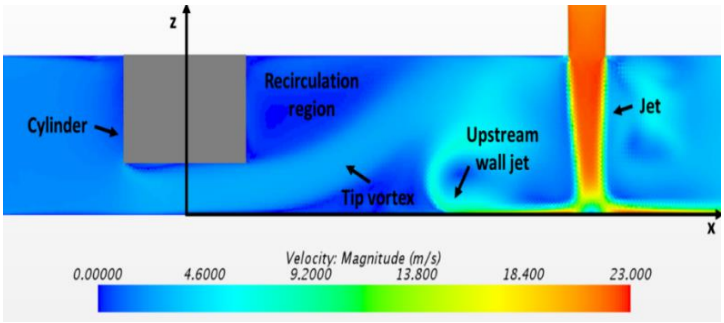

Figure 4.7 Velocity profile of tip vortex in the recirculation region for Case 6

4.1.4. Heat Transfer Result

The velocity profile of the oscillating jet for a half-time cycle showing the jet moving from one extreme to the other end, is shown in Figure 4.8 for Case 1. The jet is oscillating at a frequency of 34Hz, which causes an increase in time average Nusselt

number; this leads to a more uniform distribution of the Nusselt number. The wall jet tends to curl near the sidewall due to crossflow interaction; this causes a decrease in Nusselt number.

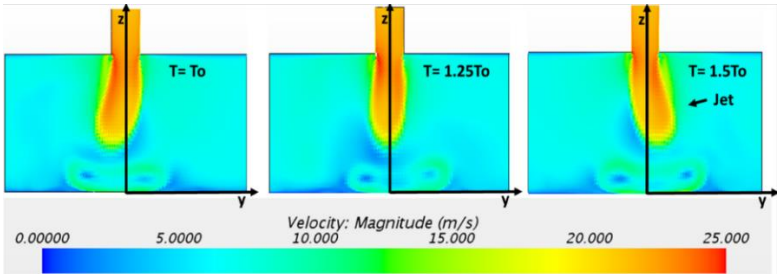

Figure 4.8 Half cycle jet oscillation for Case 1

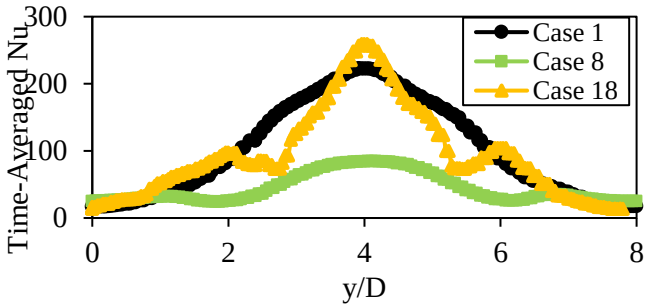

Figure 4.9 Time-averaged Nu in streamwise direction for Case 1, 8 and 18

The local Nusselt number distribution about the stagnation point in the y-direction is plotted for Cases 1, 8, and 18 (shown in Figure 4.9). The oscillating jet cases are Case 1 and 8, whereas Case 18 is a non-oscillating jet case. The secondary peak is formed for the stationary jet case, whereas it is smoothened by the uniform distribution of the Nusselt number for the oscillating cases. The maximum local Nu for the stationary jet is higher than the oscillating jet as expected (Lundgreen et al., 2017). However, the three cases are the same (h/D) and (d/D). The effect of Reynolds number and (S/d) is primarily

responsible for the differences in Nusselt number distribution.

Comparing Cases 1 and 18, having the same Reynolds number results in close stagnation Nusselt number; the more uniform Nu curve is formed due to the oscillating jet. Comparing the oscillating Cases 8 and 1, the change in Nusselt number distribution is caused by the difference in (S/d) and (Recyl). The statistical analysis shows that the channel Reynolds number contributes higher to the jet oscillation than the percentage contributed by the cylinder-jet distance. Although the frequency and amplitude are higher in Case 8, the time-averaged local Nusselt number is less for Case 1 because of the higher crossflow velocity.

4.2.Flow feature Analysis

The first phase of experimental analysis investigates the flow feature interaction of the cylinder wake with the jet. This subsection intends to study the effect of cylinder diameter and channel Reynolds number on vortex strength distribution and jet oscillation. Finally, decrypt the flow physics of cylinder wake-jet interaction using tools like unsteady pressure measurement using probes and local turbulence measurement using hotwire technique.

4.2.1. Effect of Cylinder-Jet Distance on Turbulence Intensity

The jet must be positioned at a distance downstream from the cylinder for synchronized wake interaction and jet oscillation. Therefore, the unsteady flow behavior behind the cylinder in the streamwise direction must be quantified by measuring turbulence intensity. For the following cases discussed below, the jet has been shut off to isolate the effect cylinder wake in the channel. The effect of cylinder-jet distance on turbulence intensity is quantified at various channel Reynolds numbers and cylinder

diameters. The various cylinder diameters investigated are, d = 1D, 2D, and 3D; the various channel Reynolds number investigated are, Re_{ch} = 22,000, 27,000, and 32,000.

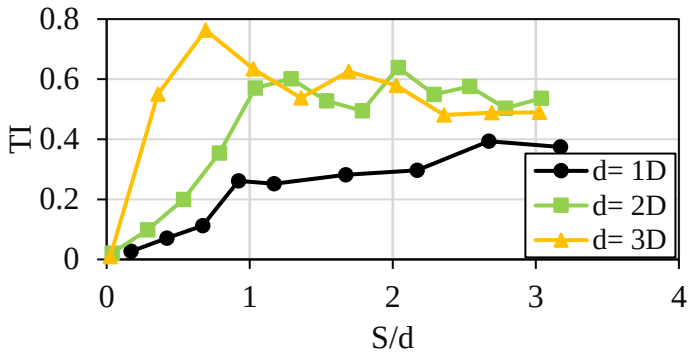

Figure 4.10 TI distribution for different cylinder diameters at Re_{ch} = 22,000

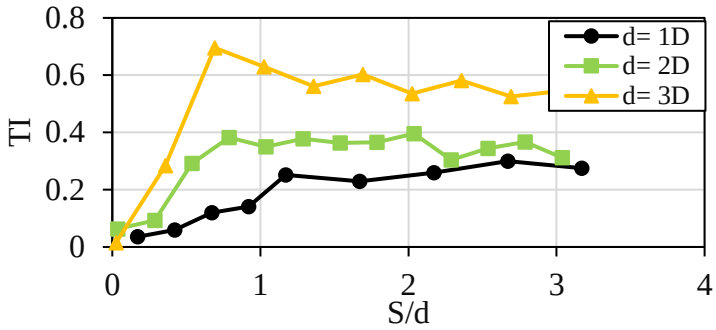

Figure 4.11 TI distribution for different cylinder diameters at Re_{ch} = 27,000

In Figure 4.10, the turbulence intensity initially increases steeply with the change in cylinder-jet distance. The initial peak of TI is formed near a one-cylinder diameter similar to the literature findings; the initial peak also determines the extent of the recirculation region behind the cylinder. However, the TI distribution downstream from the peak continues to be constant for cylinder diameter, d = 1D. In the case of cylinder diameters, d = 2D and 3D, the turbulence intensity degrades slowly.

The peak turbulence intensity magnitude is proportional to the cylinder diameter, indicating the cylinder wake strength is higher for a larger cylinder diameter. In Figure 4.10, the turbulence intensity plots for cylinder diameters, d = 2D and 3D, show minimum change. Whereas for channel Reynolds number, Re_{ch} = 27,000, turbulence intensity is strongly dependent on the cylinder diameter, shown in Figure 4.11.

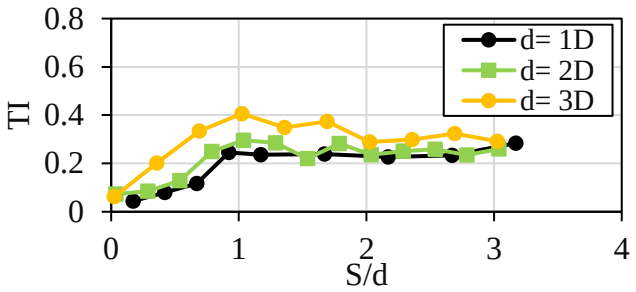

Figure 4.12 TI distribution for different cylinder diameters at Re_{ch} = 32,000

In Figure 4.12, the cylinder diameter is found to have a minimum change in turbulence intensity at a higher Reynolds number of Re_{ch} = 32,000. However, the initial peak is observed at cylinder-jet distance, S/d =1, similar to earlier plots; later, the TI remains constant for change in cylinder-jet distance.

Comparing Figure 4.10, Figure 4.11, and Figure 4.12, it can be observed that the turbulence intensity is inversely proportional to the channel Reynolds number. The TI is normalized by their respective flow velocities. Hence, it can be concluded that the lower velocities are more efficient in producing unsteady flow perturbation.

From the previous sensitivity analysis, it is observed that a lower threshold jet position (S/d) exists below which the jet is deflected into the low-pressure recirculation region of the cylinder. The TI results can be summarized stating, to achieve jet oscillation the jet

should be placed at a cylinder-jet distance, S/d = 1-3. Also, higher cylinder diameter and lower channel velocities are more efficient for jet oscillation.

4.2.2. Spectral Analysis of the Cylinder Wake

To determine the cylinder wake frequency, spectral analysis is carried out on the measured velocity readings behind the cylinder. The data is deciphered to determine the cylinder wake frequency using the fast Fourier transformation (FFT). The effect of cylinder diameter (d) and channel Reynolds number (Re_{ch}) on cylinder wake frequency is shown in Figure 4.13. The cylinder wake frequency increases with the increase in channel Reynolds number, and the wake frequency is inversely proportional to the cylinder diameter. The literature results are calculated for a Strouhal number, St = 0.21, and plotted for comparison (Williamson, 1996). The results observed are in good match with the literature; this analysis also suffice initial rig validation.

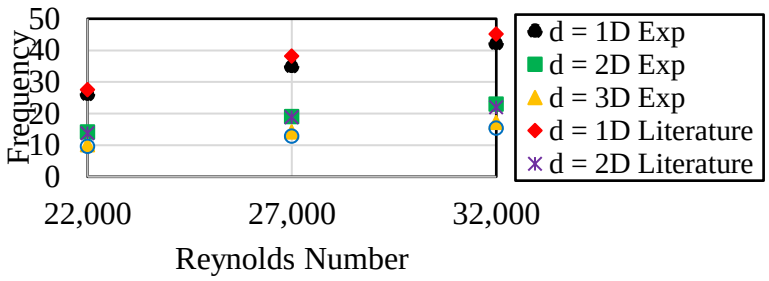

Figure 4.13 Effect of cylinder diameter and channel Re on wake frequency

4.2.3. Spectral Analysis of Target Wall Stagnation Pressure

To determine the effect of cylinder diameter and channel Reynolds number on jet oscillation, pressure fluctuation in the jet stagnation region is measured. The power spectral analysis of the pressure fluctuation leads to the computation of jet oscillation

frequency. The comparison of experimental results with the cylinder wake frequency should conclude that the jet is oscillating due to the interaction of cylinder wakes. The pressure probe measures the cylinder wake frequency and the jet oscillation frequency; hence, it is necessary to differentiate both. However, the pressure fluctuation amplitude of the cylinder wakes is less than the oscillating jet's near-stagnation pressure amplitude.

To demonstrate this theory, two cases are considered, one with jet oscillating (air-jet on) and the other with the jet orifice closed (air-jet off), producing only the cylinder wakes. The frequency spectrum for both the cases with cylinder diameter, d = 3D and channel Reynolds number, Re_{ch} = 22,000, is shown in Figure 4.14. For the case with jet orifice open, the jet oscillates at a particular frequency, f = 22Hz, and with a pressure fluctuation amplitude of P = 4.5Pa. For the case with the jet orifice closed, the cylinder wake frequency is measured to be f = 11Hz with its harmonic at f = 21Hz; and the amplitude is P = 1Pa. Thus, the amplitude of the cylinder wake is relatively four times smaller than the jet oscillation. The jet Reynolds number is a constant in this analysis. Hence the expected pressure amplitude to certify jet oscillation will be close to P = 5Pa.

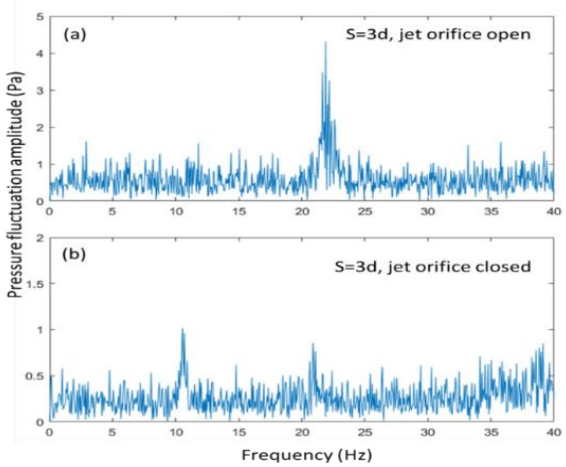

Figure 4.14 Comparison of jet oscillation (a) and cylinder wake oscillation (b)

The jet oscillates laterally in the spanwise direction from one sidewall to the other. On this path, the jet encounters the pressure probe at the center of the channel. One jet oscillation period is the jet starting at one sidewall and moving to the other end and coming back to the same sidewall, the half time period of jet oscillation is shown in Figure 4.15. The pressure probe's three stages of jet oscillation are tracked in time to understand the pressure fluctuation measurement, as shown in Figure 4.15. It can be observed that the pressure probe measures one jet oscillation period with two pressure oscillation wave periods. Hence, the pressure fluctuation frequency measured will be double the actual jet oscillation frequency. The jet oscillation frequency is assumed to be equal to cylinder wake frequency. Therefore, the measured jet oscillation frequency using the pressure probe will be double the cylinder wake frequency.

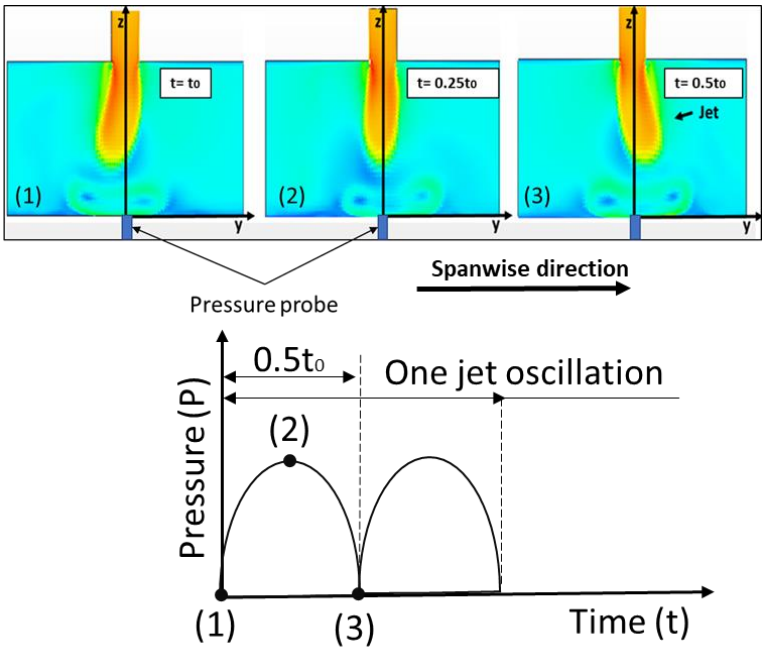

Figure 4.15 Jet oscillation traced in time using the pressure fluctuation

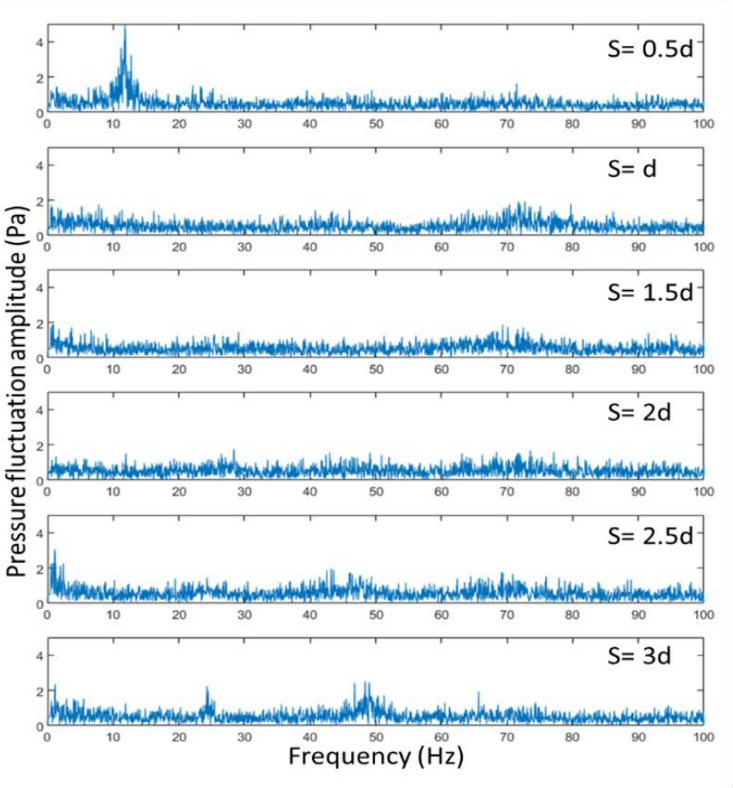

Figure 4.16 Power spectrum of pressure fluctuation at d = 1D and Re_{ch} = 22,000

Assuming the interaction of the cylinder wakes is the primer driver for jet oscillation, the higher the wake turbulence intensity more momentum exists to oscillate the jet. Figure 4.16 shows the frequency spectrum for cylinder diameter, d = 1D, and channel Reynolds number, Re_{ch} = 22,000. It can be observed that the high amplitude frequency does not exist for cylinder-jet distance, S = 0 - 2.5d in the 50Hz region (double the cylinder wake frequency); hence there is no jet oscillation. However, at S = 3d, a peak is observed at f = 48.38Hz, proving the jet oscillates in this case. Comparing the results with the TI distribution (Figure 4.10), the jet is oscillating at S = 3D when the TI is the maximum (TI = 0.39). Hence, a threshold, TI = 0.39, is the minimum required above which the jet tends to oscillate.

Also, a high amplitude frequency, f = 11.85Hz, is observed for S = 0.5D. This is an unexpected pressure fluctuation observed in the cylinder recirculation region. Further study has to be performed to determine the cause for this low-frequency oscillation.

The Figure 4.17 and Figure 4.18, shows the frequency spectrum for channel Reynolds number, Re_{ch} = 27,000 and Re_{ch} = 32,000, respectively. It can be concluded that the jet is not oscillating in these cases because there is no high amplitude frequency in the 70Hz and 84Hz regions, respectively. Also, the turbulence intensity in these cases is less than the threshold, TI = 0.39 for all the cylinder-jet distances tested.

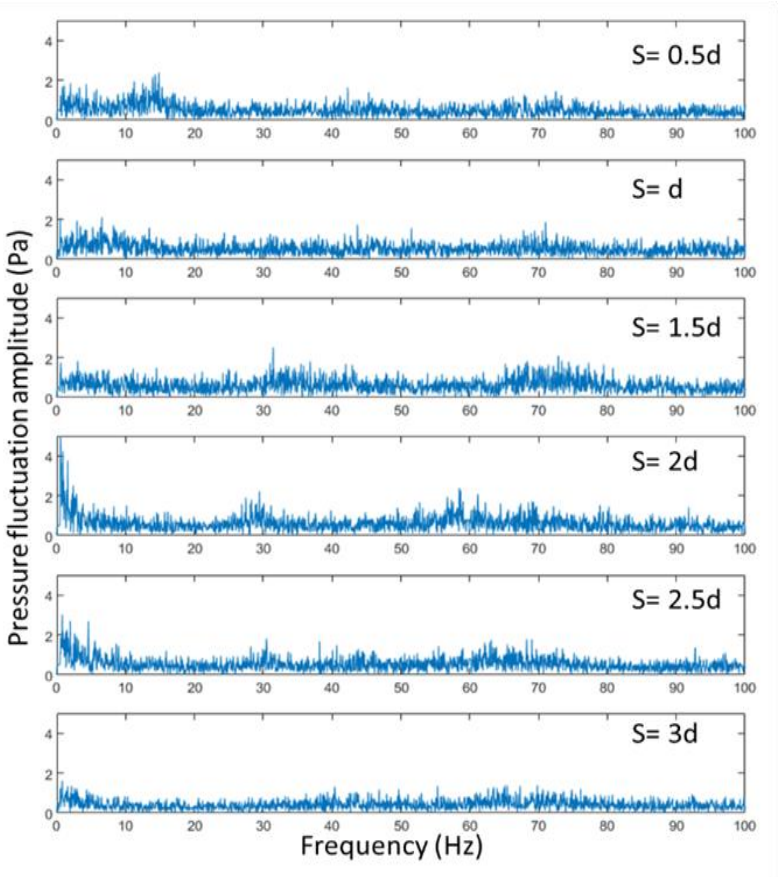

Figure 4.17 Power spectrum of pressure fluctuation at d = 1D and Re_{ch} = 27,000

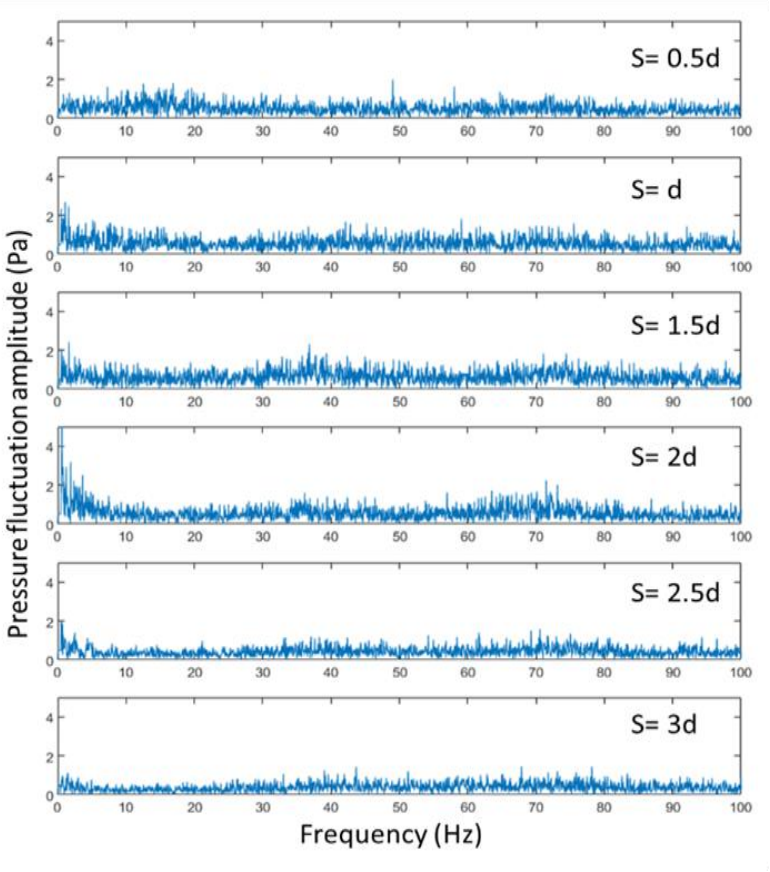

Figure 4.18 Power spectrum of pressure fluctuation at d = 1D and Re_{ch} = 32,000

Figure 4.19 shows the frequency spectrum for cylinder diameter, d = 2D and Channel Reynolds number, Re_{ch} = 22,000. The high amplitude frequency is observed at an average frequency, f = 28.85Hz for S = 2 - 3D; this is close to the cylinder wake frequency, f = 2×13.78 = 27.56Hz; hence the jet is oscillating for S = 2 - 3D cases. For the same cylinder diameter and channel Reynolds number, the TI is above threshold (TI = 0.39) for S = 1 - 3D, but the jet is oscillating only for S = 2 - 3D. This phenomenon is due to the jet being deflected into the low-pressure cylinder recirculation region for S < 2D, as explained in the previous sensitivity analysis.

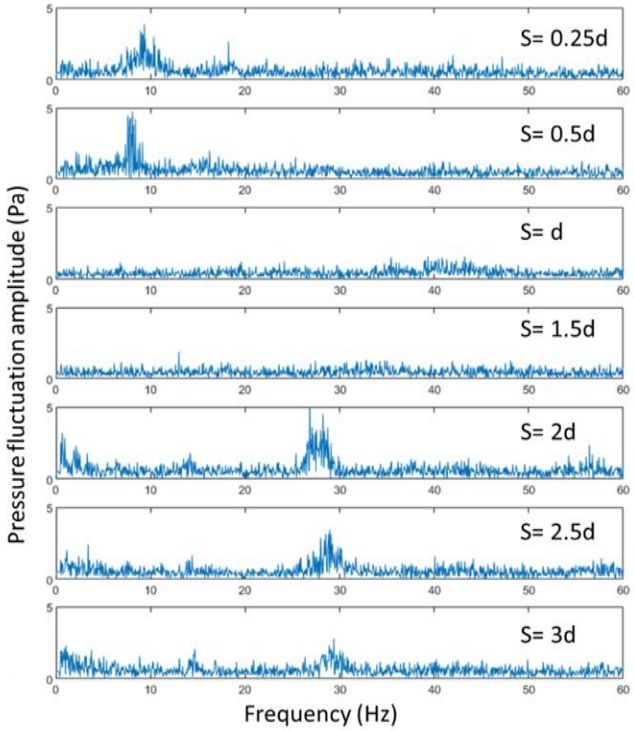

Figure 4.19 Power spectrum of pressure fluctuation at d = 2D and Re_{ch} = 22,000

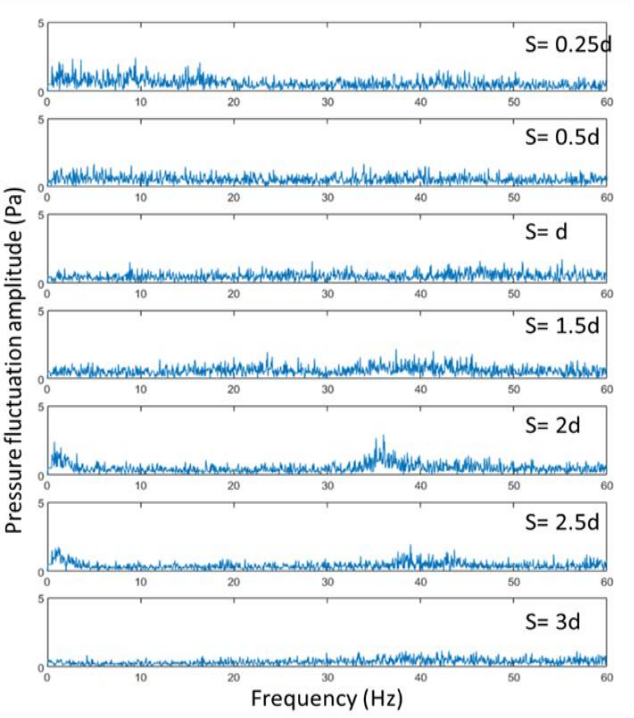

Figure 4.20 Power spectrum of pressure fluctuation at d = 2D and Re_{ch} = 27,000

Figure 4.20 shows the frequency spectrum for cylinder diameter, d = 2D, and channel Reynolds number, Re_{ch} = 27,000. At S = 2D, the high amplitude frequency, f = 36Hz, is closely matched with the cylinder wake frequency, f = 2×18.94 = 37.88Hz; hence, the jet oscillates. Also, the TI results confirms, for S = 1 - 2 D, the TI is above the threshold, TI = 0.39. Applying the second limit that the S ≥ 2D, the jet should oscillate only at S = 2D. Figure 4.21 shows the frequency spectrum for cylinder diameter, d = 2D, and channel Reynolds number, Re_{ch} = 32,000 for various cylinder-jet distance. The results show no frequency peaks; hence, the jet is not oscillating at any cylinder-jet distance.

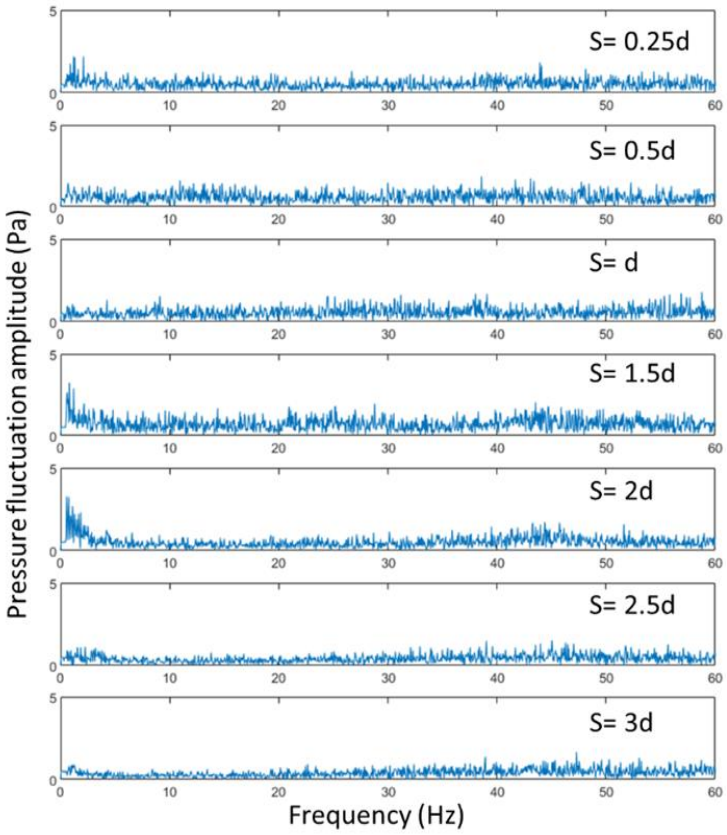

Figure 4.21 Power spectrum of pressure fluctuation at d = 2D and Re_{ch} = 32,000

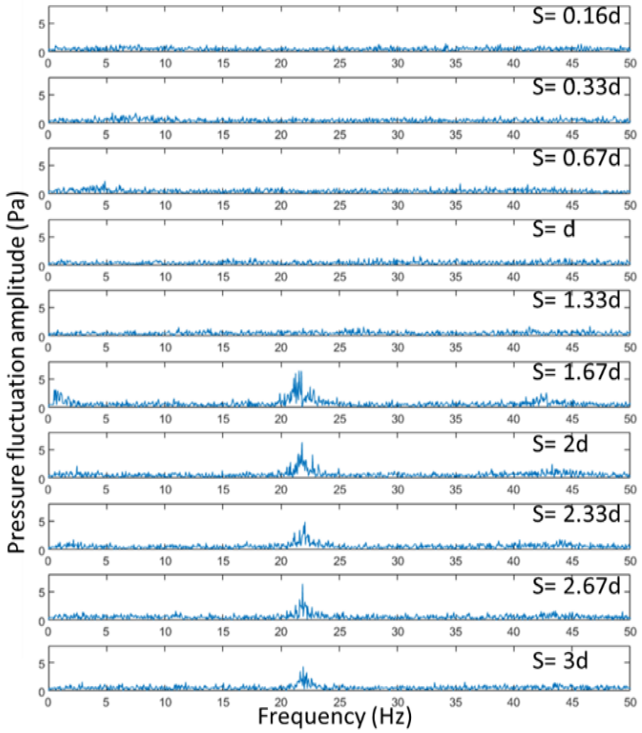

Figure 4.22 Power spectrum of pressure fluctuation at d = 3D and Re_{ch} = 22,000

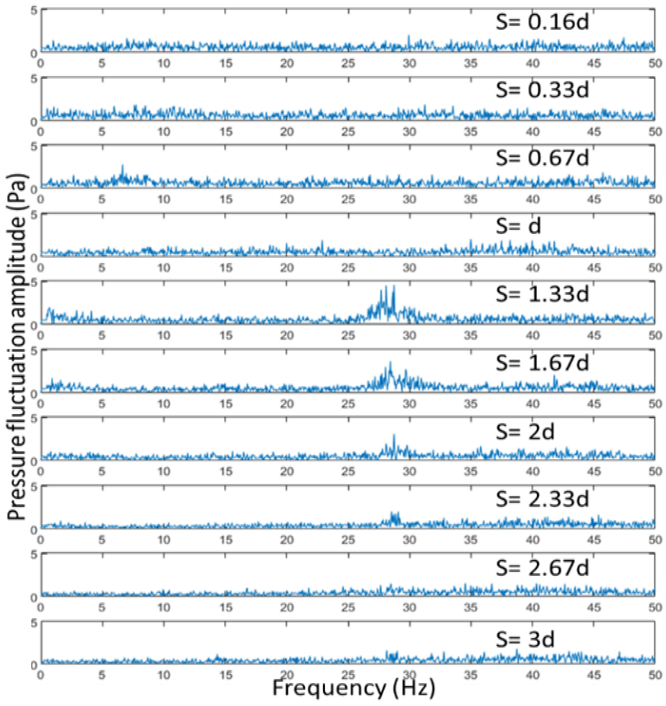

Figure 4.23 Power spectrum of pressure fluctuation at d = 3D and Re_{ch} = 27,000

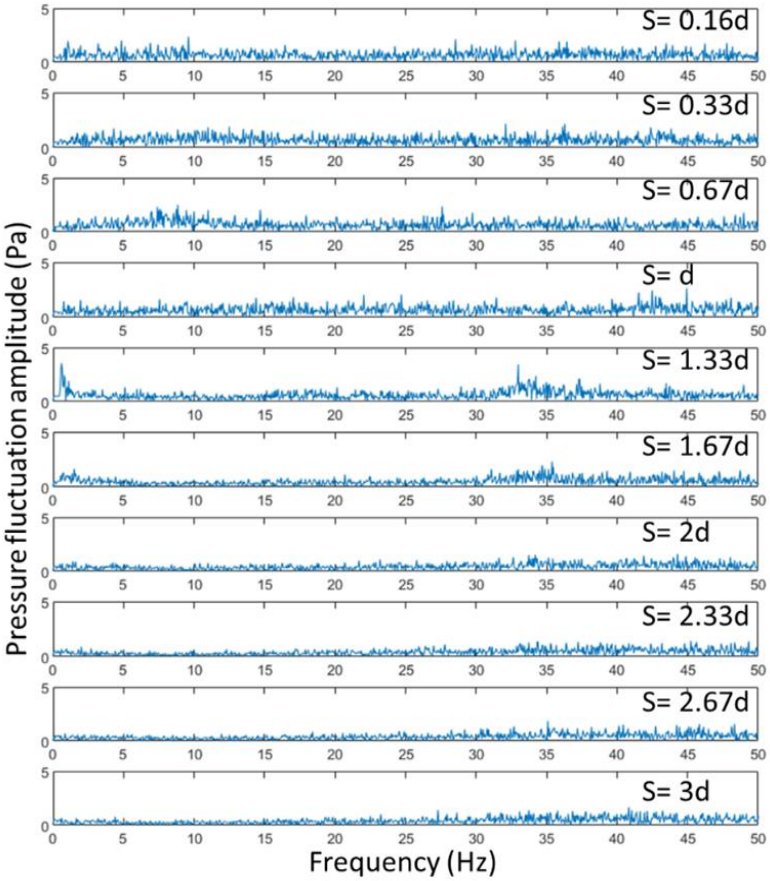

Figure 4.24 Power spectrum of pressure fluctuation at d = 3D and Re_{ch} = 32,000

Figure 4.22 shows the frequency spectrum for cylinder diameter, d = 3D, and channel Reynolds number, Re_{ch} = 22,000. The average jet oscillation frequency, f = 21.82Hz matching cylinder wake frequency, f = 2×10.21 = 20.42Hz, is observed for the cylinder-jet distance, S= 1.67 - 3D. The local TI for this case is higher than the threshold TI.

Results for the same cylinder diameter at channel Reynolds number, Re_{ch} = 27,000, are different from the previous results discussed (Figure 4.23). The jet oscillates at S = 1.33 - 2.33 D at an average frequency, f = 28.61 Hz compared to the cylinder frequency, f = 2×14.21 = 28.42Hz. Although the TI is higher than the threshold for S > 2.33D, there is no jet oscillation. Probably due to the jet deflected away from the pressure probe leading

to the probe not measuring the fluctuation. For the same cylinder at channel Reynolds number, Re_{ch} = 32,000, no jet oscillation frequency is observed in Figure 4.24. Also, the TI distribution for this case is less than the threshold for all cylinder-jet distance.

Comparing all the results, a common trend can be observed that the frequency amplitude decreases with the increase in cylinder-jet distance. The decrease in pressure fluctuation magnitude is due to the jet being deflected away from the pressure probe. However, to confirm this assumption, further experimentation is required.

4.3. Final CFD Analysis

The flow field of the jet in a crossflow (JICF) is primarily affected by the jet-crossflow momentum ratio (J). For constant density flows, the momentum ratio can be reduced to the velocity ratio (VR). The above initial results did study the effect of channel Reynolds Number on jet oscillation, but the velocity ratio was not calculated or given any importance. In this final analysis, the flow interaction between the cylinder wake and jet is studied in detail for various velocity ratios. The preliminary CFD analysis and flow feature analysis results can be summarized to define the oscillating region. The parameters leading to jet oscillation can be summarized in the table below.

Table 4.5

Parameters for jet oscillation

Parameter	Value
Cylinder diameter	d/D = 2 - 3
Cylinder-jet distance	S/d = 3 - 4
Velocity ratio	VR = 4
Jet Reynolds Number	Re_j = 38,000

The above parameters leading to jet oscillation are investigated in the following subsection. In this analysis, the cylinder diameter selected is d = 2. Additionally, the cylinder-jet distance, S/d = 2, will be investigated. The cylinder-jet distance, S/d = 2, will lead to non-oscillating cases. These cases are used to compare the effect of oscillating and non-oscillating cases. The velocity ratio is increased from VR = 4. The jet oscillation is continuously monitored and helps limit the velocity ratio investigated when a non-oscillating case is encountered.

4.3.1. Validation

The current work heat transfer result is validated from the literature work of Florschuetz et al., 1980. The literature test domain includes a channel jet impingement with no initial crossflow; the geometrical parameters include H/D = 3, W/D = 8, and x/D = 10. The literature includes a series of inline multiple jet impingements; however, the current work results include only the first jet. The target plate Nusselt number is averaged in segments similar to the literary work; a graphical representation of the averaging scheme is shown in Figure 4.25.

The segment average Nusselt number of the CFD and literature results are shown in Figure 4.26. Comparing the CFD and literature results, the CFD results have a maximum error of 10% near the stagnation point (Segment 2). It is an expected trend observed in CFD results that the RANS model over-predicts the stagnation Nusselt number. However, the segment 1 and 3 CFD results are in close agreement with the literature findings. In this current work, the result from the CFD is utilized to determine an initial estimate of Nusselt number and classify oscillating and non-oscillating jets. And to understand the flow structure of jet oscillation due to vortex interaction.

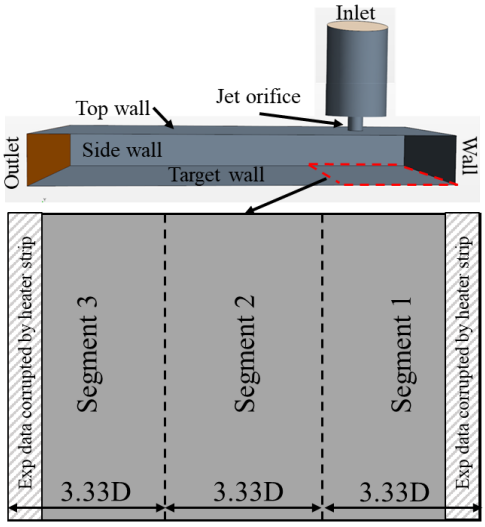

Figure 4.25 Graphical representation of averaging scheme

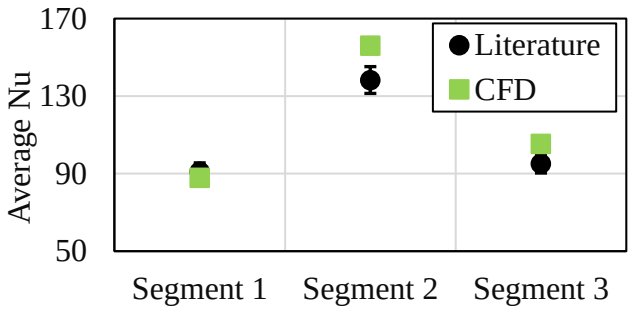

Figure 4.26 CFD Validation segment average Nu

4.3.2. Spectral Analysis of Lift Coefficient

The above-discussed results conclude that the cylinder wake frequency will be equal to the cylinder lift force-frequency (Williamson, 1996). Hence, an FFT analysis is performed on the cylinder lift coefficient from the CFD result to determine the wake frequency. The varying parameters are the velocity ratio and cylinder-jet distance. The cylinder diameter is a constant value, d = 2D.

The spectral analysis of lift coefficient for varying velocity ratios at S/d = 2 is shown

in Figure 4.27. The results show no distinctive peaks in the frequency plots for all the velocity ratios tested. Hence, no cylinder wakes are produced in this case. Figure 4.28 shows the spectral analysis for varying velocity ratios at S/d = 3. The distinctive peaks are observed for velocity ratios, VR = 4 and 4.5.

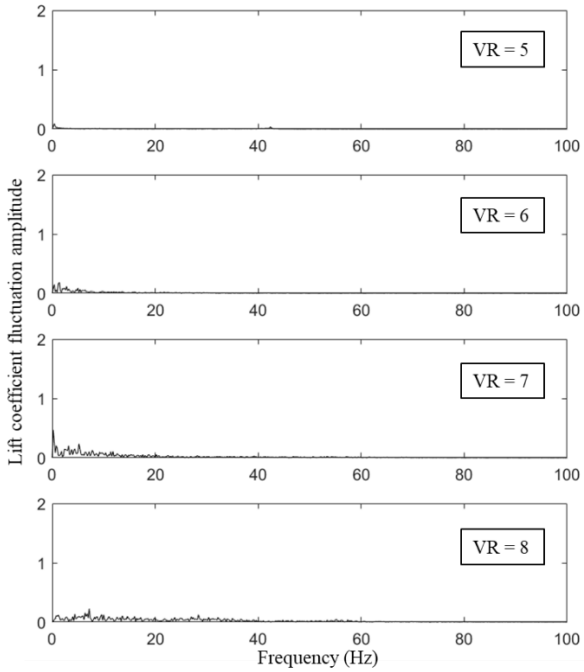

Figure 4.27 Spectral analysis of lift coefficient at S/d = 2

The two peaks observed for S/d = 4 and 4.5 are at frequency, f = 28Hz and f = 24.6Hz, respectively. Therefore, the frequency determined will be equal to cylinder vortex shedding frequency. For velocity ratios, VR = 5 – 6 no frequency peaks are observed, concluding no-wake shedding for these cases. This may be due to the reattachment of the shear layer onto the jet, and this assumption can be confirmed by the vorticity distribution in the following subsections.

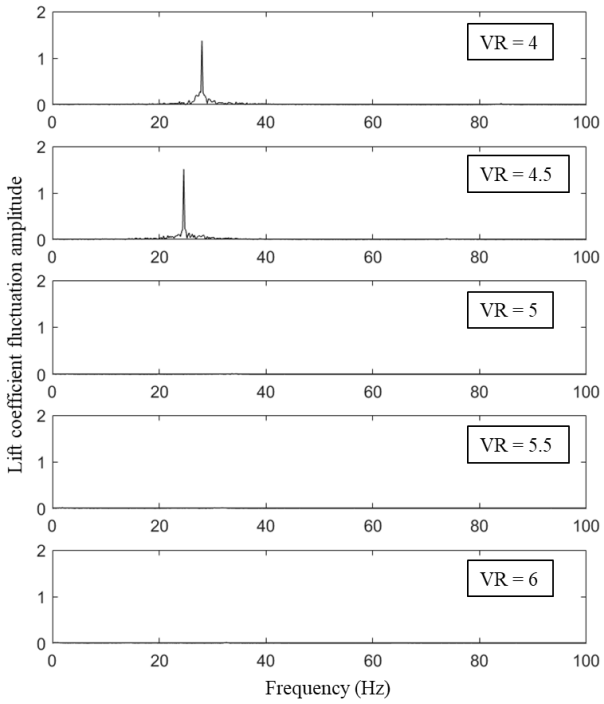

Figure 4.28 Spectral analysis of lift coefficient at S/d = 3

Figure 4.29 shows the spectral analysis of lift coefficient for the tested velocity ratios at S/d = 4. In this case, frequency peaks are observed for velocity rations ranging from VR = 4 – 7. The wake frequency decreases with the increase in velocity ratio due to the decrease in crossflow velocity. Also, the increase in cylinder-jet distance prevents reattachment of the shear layer and hence produces cylinder wakes. For velocity ratio, VR = 8, no peaks are observed, certifying no cylinder vortex shedding.

Comparing Figure 4.28 and Figure 4.29, the vortex shedding is observed for velocity ratios, VR = 4 – 4.5 at S/d = 3; whereas for cylinder jet-distance, S/d = 4 vortex shedding is observed for a higher velocity ratio range, VR = 4 – 7. This phenomenon is due to the increase in the cylinder-jet distance causing difficulty in the reattachment of the shear layer onto the jet in case of S/d = 4.

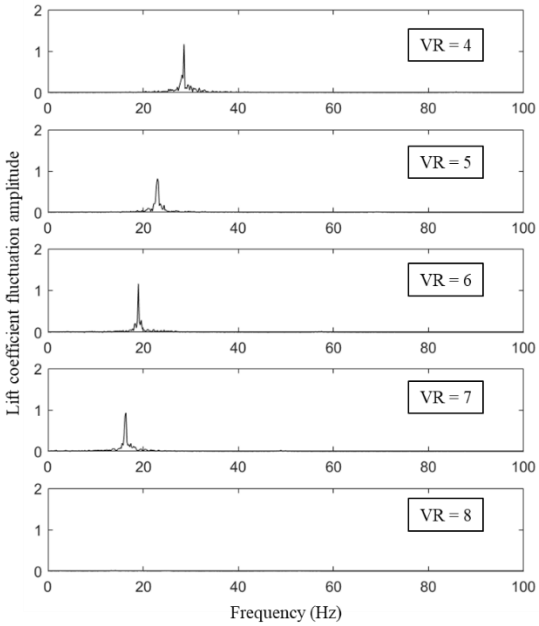

Figure 4.29 Spectral analysis of lift coefficient at S/d = 4

The observed frequencies for cylinder diameter, d = 2D at different velocity ratios can be verified with the literature results using Strouhal number. The literature result frequency is calculated using the uniform crossflow velocity and Strouhal number, St = 0.21. The cylinder wake frequency observed for the various velocity ratios is summarized in Figure 4.30. It can be observed that the CFD frequency predicted is higher than the literature findings. This is because the k-ω SST turbulence model overpredicts the Strouhal number/ frequency, and the blockage ratio has considerable effects on the increase in Strouhal number (Anagnostopoulos et al., 1996). The Strouhal number in the CFD case is calculated to be, St = 0.25, and the literature community does accept results in the range of St = 0.2 - 0.3 (Bearman, 1969). However, this study is focused on the flow interaction and jet oscillation, which depends mainly on the wake strength. Hence, this overprediction is acceptable for this current investigation.

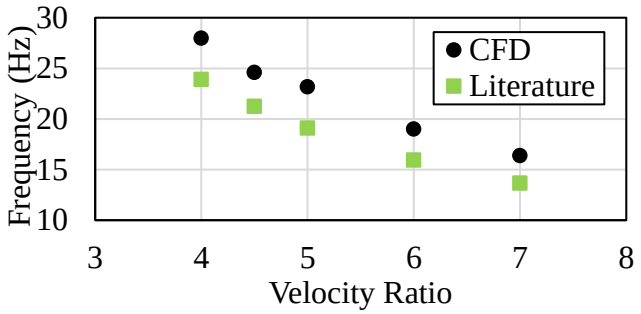

Figure 4.30 Comparison of CFD and literature wake frequency

4.3.3. Spectral Analysis of Target Wall Stagnation Pressure

The stagnation pressure data measured in time is utilized to differentiate oscillating and non-oscillating jets. As discussed before in the flow feature analysis, the frequency peaks determining the jet oscillation will equal twice the cylinder wake frequency.

The stagnation pressure data is obtained from a point probe placed in the stagnation region. The same cases discussed above in the cylinder wake spectral analysis are investigated. Figure 4.31 shows the FFT analysis of pressure fluctuation for various velocity ratios at S/d = 2. The results show no frequency peaks for all the velocity ratios tested. This is an expected result, as no cylinder wakes were observed in the S/d = 2 case. Also, the response surface analysis concluded no jet oscillation for the cylinder-jet distance, S/d = 2.

Figure 4.32 shows the spectral analysis of stagnation pressure for various velocity ratios at S/d = 3. The results show two peaks, a strong peak with its harmonic for the cases with velocity ratio, VR = 4 and 4.5. The pressure frequency observed is f = 56Hz, and f = 49.2 Hz for a velocity ratio, VR = 4 and 4.5, respectively. The pressure frequency is equal to twice the wake frequency, f = 28 × 2 = 56Hz and f = 24.6 × 2 = 49.2 Hz, justifying jet oscillation for these cases. As discussed earlier, no wakes were produced for

velocity ratios, VR = 5 – 6; hence jet cannot oscillate. Therefore, no peaks are observed for velocity ratios, VR = 5 – 6.

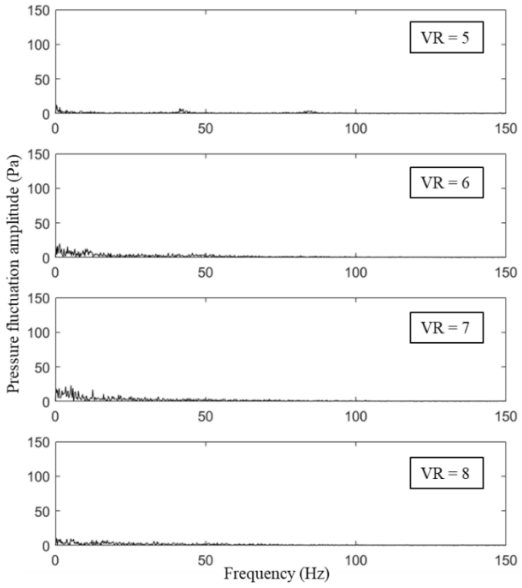

Figure 4.31 Spectral analysis of stagnation pressure at S/d = 2

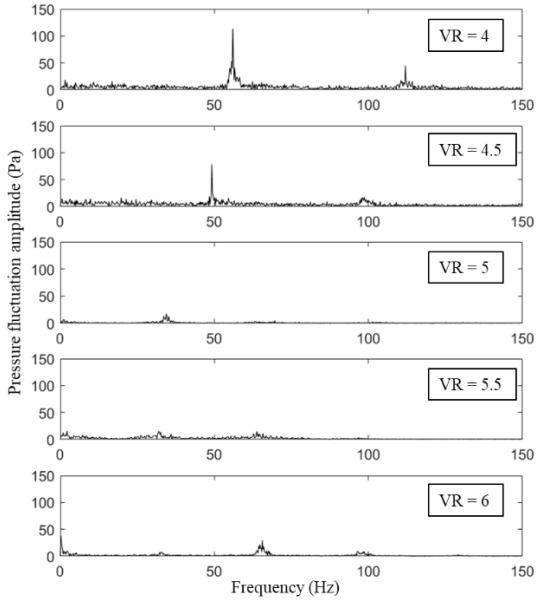

Figure 4.32 Spectral analysis of stagnation pressure at S/d = 3

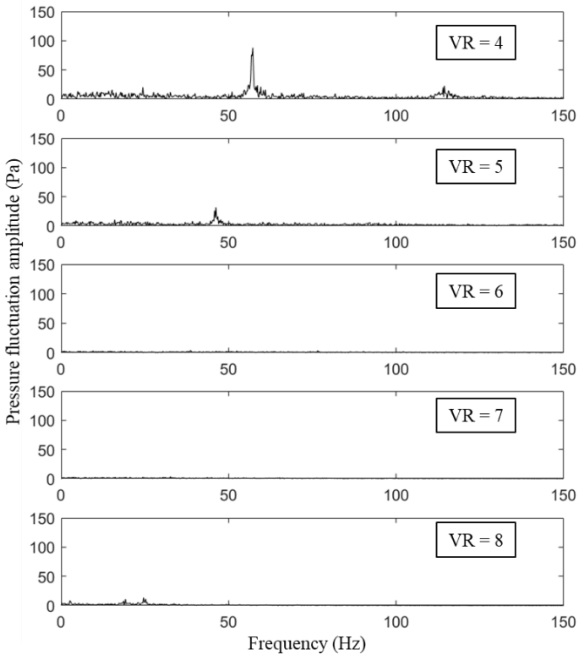

Figure 4.33 Spectral analysis of stagnation pressure at S/d = 4

Figure 4.33 shows the spectral analysis of stagnation pressure for various velocity ratios at S/d = 4. The results show peaks at a frequency, f = 56Hz for VR = 4 and f = 46.2Hz for VR = 5. The pressure frequency is equal to twice the wake frequency, f = 28 × 2 = 56Hz and f = 23.2× 2 = 46.4 Hz, justifying jet oscillation for these cases. The jet does not oscillate for velocity ratios, VR = 6 – 8 because no peaks are observed. From cylinder wake spectral analysis, cylinder wakes were detected for velocity ratios, VR = 4 – 7. This defines an anomaly stating that cylinder wakes do not lead to jet oscillation in all cases. This anomaly may be due to the insufficient cylinder wake strength to move the jet.

The above results can be summarized, stating jet oscillation is only observed for low-velocity ratios, VR = 4 – 5 for cylinder-jet distance, S/d = 3 – 4. Also, cylinder-jet distance, S/d = 2, led to non-oscillating jet cases for all the velocity ratios tested.

4.3.4. Flow Field Results

The mechanism of cylinder wake-jet interaction leading to jet oscillation is analyzed using vorticity, turbulent kinetic energy (TKE), and velocity contour distribution. Also, from the previous section, the non-oscillating jet case (VR = 6 – 8 & S/d = 4) stating the presence of cylinder wakes does not lead to jet oscillation is analyzed. Hence, the flow field results are divided into two subsections, oscillating jet case, and non-oscillating jet case.

4.3.4.1. Oscillating Jet Case

The flow features of an oscillating jet are analyzed at different time intervals using vorticity, TKE, and velocity contours. The oscillating jet case with velocity ratio, VR = 4, and cylinder-jet distance, S/d = 3, is selected for this analysis. The oscillating jet as a time period of t_p = 0.035seconds. The observed contour plots are obtained after steady jet oscillation is attained (approximately after 10 seconds).

Figure 4.34 shows the vorticity distribution for a jet oscillation cycle for every ¼th time period. The vorticity distribution plot is obtained from the x-y plane at a channel height of z/D = 1.5. The cylinder sheds counter-clockwise rotating vortex and clockwise rotating vortex consecutively at cylinder wake frequency. The counter-clockwise rotating vortex is denoted by negative vorticity (blue color), and the clockwise rotating vortex, denoted by positive vorticity (red color). The jet core deforms into a bean shape due to the crossflow and wake interaction, similar to literature findings (Muppidi et al., 2005). Also, it is observed that the jet core rotates clockwise and anticlockwise in time due to consecutive wake vorticity interaction. Along with the cylinder vortex shedding, the deformed jet core also produces wakes downstream. Hence, these jet core wakes

produced also induces forces onto the jet core itself.

At the initial time cycle ($t = t_p$), the jet core is at the maximum displacement in the y-direction. Due to previous clockwise (CW) rotating vortex interaction, the jet is sheared to rotate in counter-clockwise (CCW) direction and pushed away. At the exact moment, a CCW rotating vortex is shed from the cylinder. Also, an anticlockwise rotating vortex is shed for the jet core, inducing an additional torque in the anticlockwise direction.

At the time cycle, $t = 1/4t_p$, the vortex shedding moves downstream, and the jet core is rotating anticlockwise. But the jet core induced clockwise rotating vortex will introduce a torque in the CW direction, reducing the cylinder wake induced torque.

At time cycle, $t = 1/2t_p$, the jet core at its maximum displacement on the other sidewall. And the counter-rotating vortex comes in contact with the jet core, inducing a torque onto the jet core. Simultaneously, a clockwise-rotating vortex is started to shed from the cylinder. Also, the jet core vortex produced is moving downstream.

At time cycle, $t = 3/4t_p$, the previously induced torque rotates the jet core in the clockwise direction, and the clockwise-rotating vortex is completely shed from the cylinder traveling downstream. Also, the jet core produces a CCW vortex, which induces a torque in the CCW direction, restricting the force indued by the cylinder. And complex flow interaction of the vortices will lead to the production of secondary and tertiary vortices.

Finally, the clockwise-rotating cylinder vortex forces the jet core to rotate anticlockwise, and the cycle repeats. As the deformed jet rotates in either direction, it can also be observed that the jet core position moves in the y-direction.

Summarizing the results, the deformed jet core rotates and moves in the y-direction,

primarily driven by the cylinder vortex interaction. However, the jet core-induced vortex is not synchronized with the cylinder vortex shedding; hence, the cylinder vortex's effectiveness is reduced. Also, the vortex strength of the cylinder wakes produced is above the threshold to induce jet oscillation.

The turbulent kinetic energy (TKE) data is plotted in the x-y plane at a channel height of z = 0.25D above the target plate (shown in Figure 4.35). The time steps shown in the TKE contour plots are synchronous with the above discussed time steps of the vorticity plots. As the TKE plot is in proximity with the target plate, the wall jet's extent and shape can be observed. Also, the jet core and its recirculation region possess high turbulent kinetic energy. The wall jet is also observed to move laterally and rotate with jet core motion in time.

At the initial time cycle ($t = t_p$), the jet core and the wall jet sync with maximum lateral and angular deflection. However, at cycle time, $t = 1/4t_p$, the jet and wall jet lag behind the jet core rotation. This is due to the cylinder vortex induces a torque only into the jet core. And the jet core in turn, tries to rotate the wall jet, which will consume time due to the compressibility of the fluid material.

At time cycle, $t = 1/2t_p$, the jet core at its maximum displacement on the other end sidewall. However, the wall jet lags behind and attains maximum angular and lateral deflection at the time cycle, $t = 3/4t_p$. And the jet core is trying to go back to its initial position. Once it reaches the top sidewall, the cycle repeats.

Figure 4.36 shows the velocity contour of the jet oscillation cycle in the y-z plane at the jet orifice center. The jet core is observed to move laterally in the y-direction, and the wall jet follows the lead of the jet core. The wall jet curls at the sidewalls and the amount

of curling increases as the wall jet move towards the sidewall. Initially, the wall jet curling is limited under the shade of the cylinder, however near the sidewall, the crossflow strength is higher, introducing more curling of the wall jet.

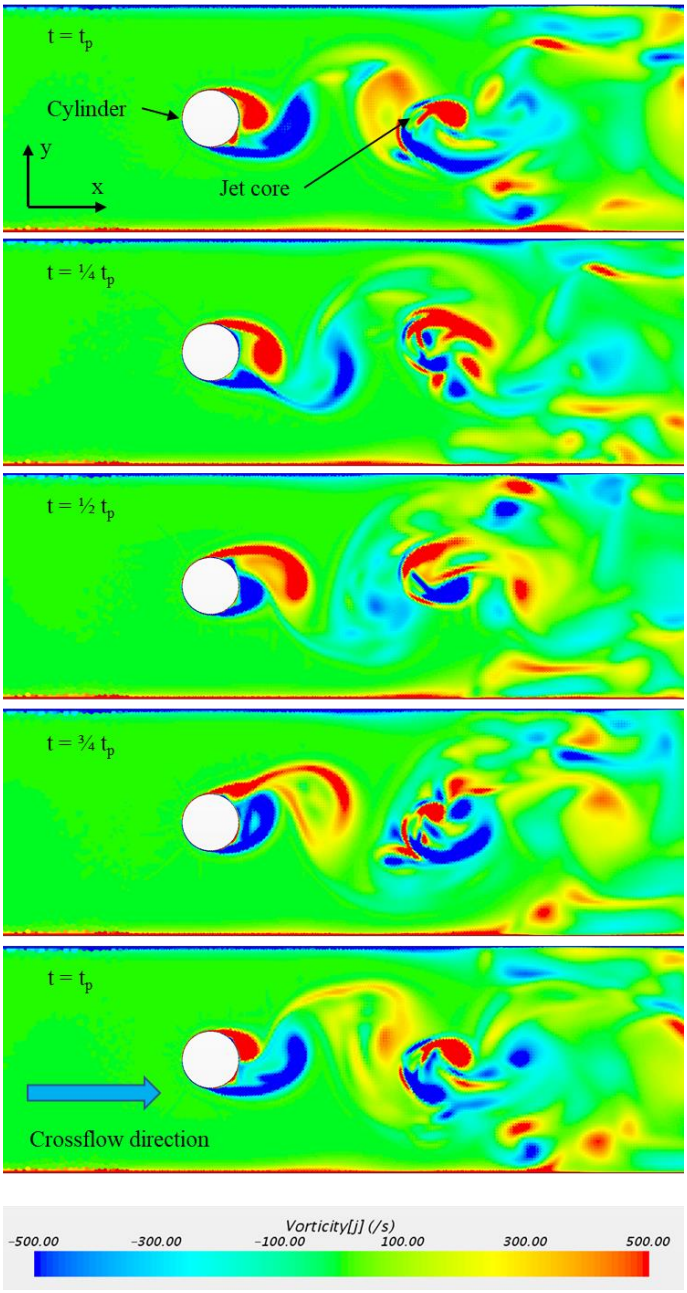

Figure 4.34 Vorticity distribution of a jet oscillation cycle

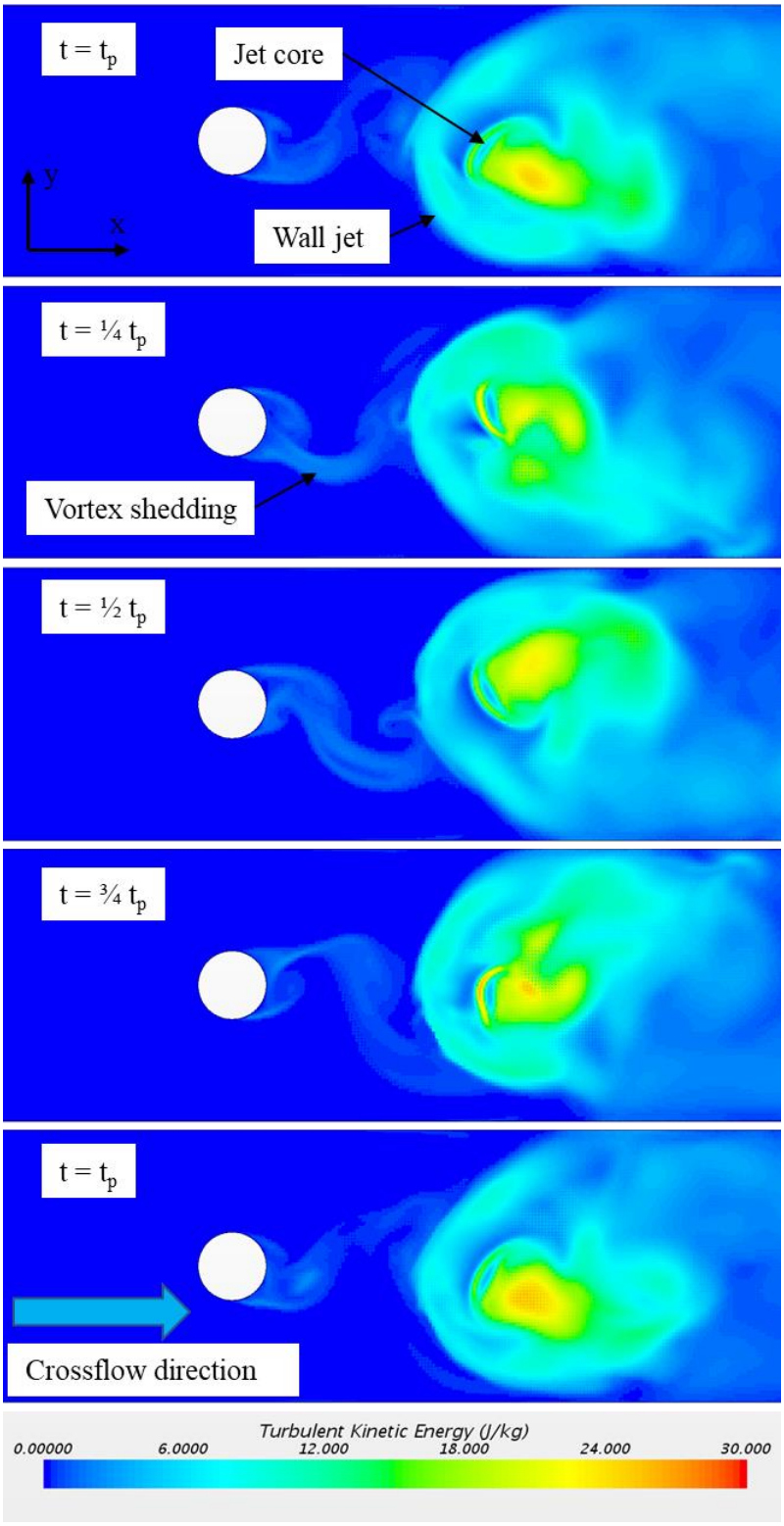

Figure 4.35 TKE distribution of a jet oscillation cycle

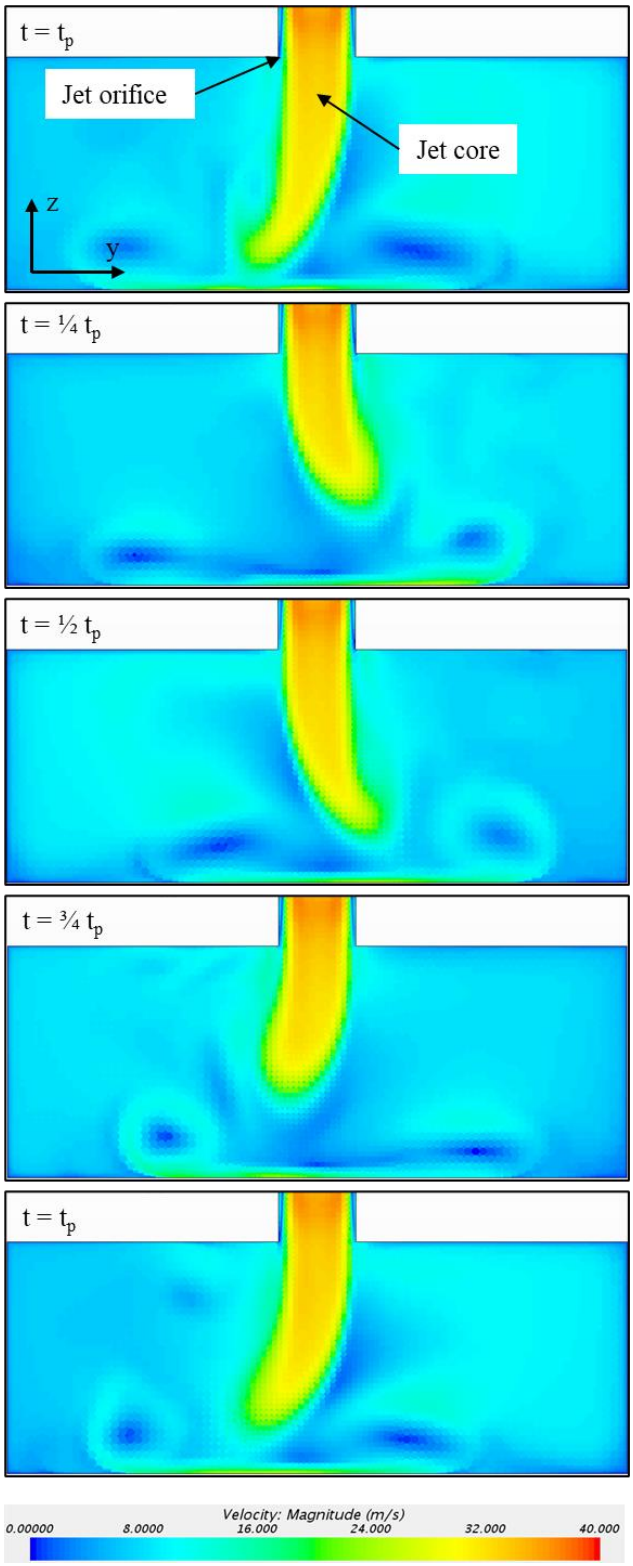

Figure 4.36 Velocity distribution of a jet oscillation cycle

4.3.4.2. Non-Oscillating Jet Case

The flow features of the anomaly observed in the spectral analysis are analyzed further using the vorticity, TKE, and velocity contours at different time intervals. The oddity of the observed cylinder wakes to lead to no jet oscillation is investigated in this section. The non-oscillating jet case with a velocity ratio, VR = 7, and cylinder-jet distance, S/d = 4, is selected for this analysis. The non-oscillating jet as a cylinder wake time period of t_p = 0.061seconds. The observed contour plots are obtained after steady cylinder wake oscillations are attained (approximately after 10 seconds).

Figure 4.37 shows the vorticity distribution for a jet oscillation cycle for every ¼th time step. The figure shows the cylinder wakes and jet core wakes are produced, but the deflection and rotation of the jet core is minimum. Therefore, stating the cylinder wake strength is below the threshold to oscillate the jet. Also, the cylinder wake shedding and jet core shedding are not synchronized. The jet core movement is unsteady and irregular to the cylinder wake interaction. The cylinder wakes observed will induce an oscillating lift and drag force into the cylinder itself. Hence the spectral analysis of the lift coefficient facilitates in determining the cylinder wake frequency.

The initial time step ($t = t_p$) shows that the counter-rotating vortex has already been shed from the cylinder and traveling downstream. Simultaneously, a CCW rotating vortex is shed from the deformed jet core. The vortex shedding would induce a torque in the CCW direction. Hence the deformed jet starts to rotate in the CCW direction; however, no lateral deflection is observed. At the time step, $t = 1/4t_p$, the CCW rotating vortex shears the jet core in the CW direction. At the same time, a CW rotating vortex is ready to detach from the cylinder. Now the jet core rotates in the CW direction.

At time cycle, t = 1/2t_p, the CW rotating cylinder wake is detached from the cylinder and moving downstream. And a CCW rotating vortex started to form on the cylinder. The CW rotating cylinder wake impacts the jet core, forcing it to rotate in the CCW direction (at time step, t = 3/4t_p). The maximum rotation of the jet core is observed at this movement. lastly, the CCW vortex detaches from the cylinder, and jet continues in CCW rotation.

Comparing oscillating and non-oscillating jet case vorticity contour plots, the oscillating jet case's vortex strength is higher than the non-oscillating jet. The cylinder wakes from the oscillating jet induce more rotation into the deformed jet core. Secondary and tertiary vortex pairs are formed in oscillating jet cases but absent in the non-oscillating jet case. The jet core does not produce vortex shedding similar to the oscillating jet case, and the jet core wakes shed are irregular.

Figure 4.38 shows the turbulent kinetic energy contour plots of the x-y plane above the target plate at a distance of z = 0.25D for one cylinder wake shedding. As the vorticity plots showed, the cylinder wakes imparting energy into the jet core to rotate it. The TKE plots show the wall jet and recirculation region displays minimum change in rotation or deflection, for time steps, t = t_p - ½ t_p. And suddenly, the deformed jet core rotates to its maximum angle from time, t = ¾ t_p - t_p. The jet rotation observed in the last two-time steps is irregular and unsteady behavior of the jet. The current results compared to jet oscillation case TKE distribution, the wall jet rotates and moves laterally in the oscillating jet case.

The velocity contour plot of the jet core is shown in Figure 4.39, in the y-z plane. The jet oscillation for one cylinder wake time period is shown for every ¼th time step. The

plots show minimum to no jet oscillation compared to the previous oscillating jet case findings. Hence, no frequency peak is observed in the spectral analysis of the target wall pressure data. Further, the wall jet appears to show less curling near the sidewall region than the oscillating jet case results due to lower crossflow strength (VR = 7).

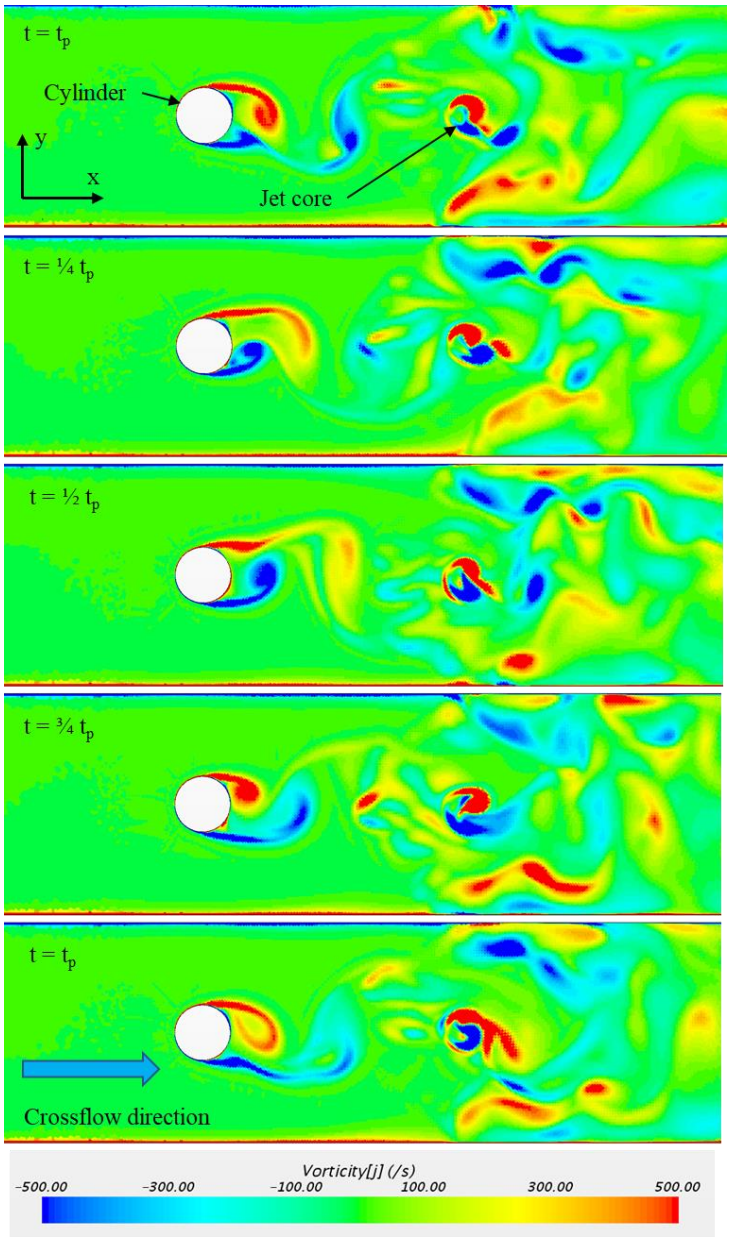

Figure 4.37 Vorticity distribution of a non-oscillating jet

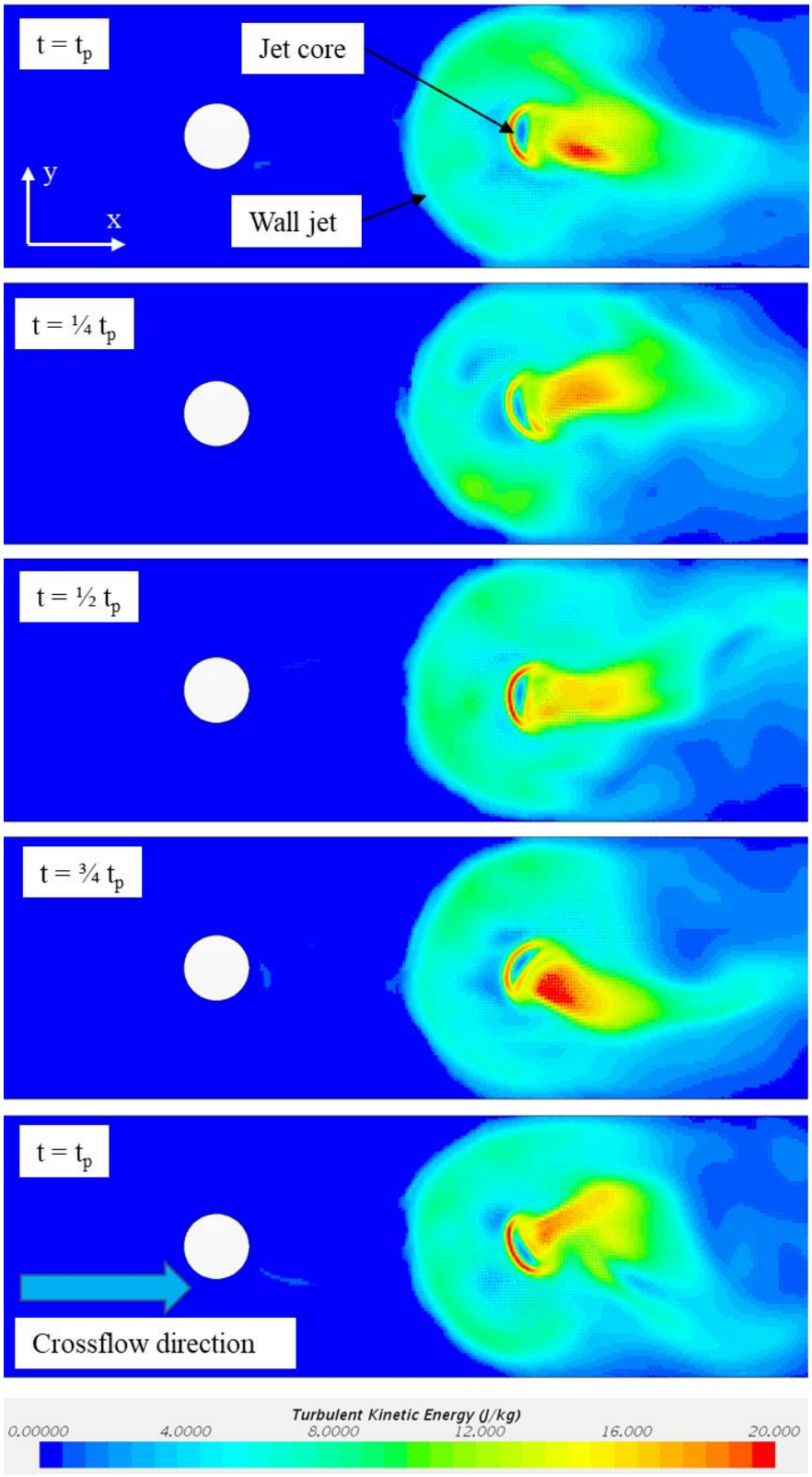

Figure 4.38 TKE distribution of a non-oscillating jet

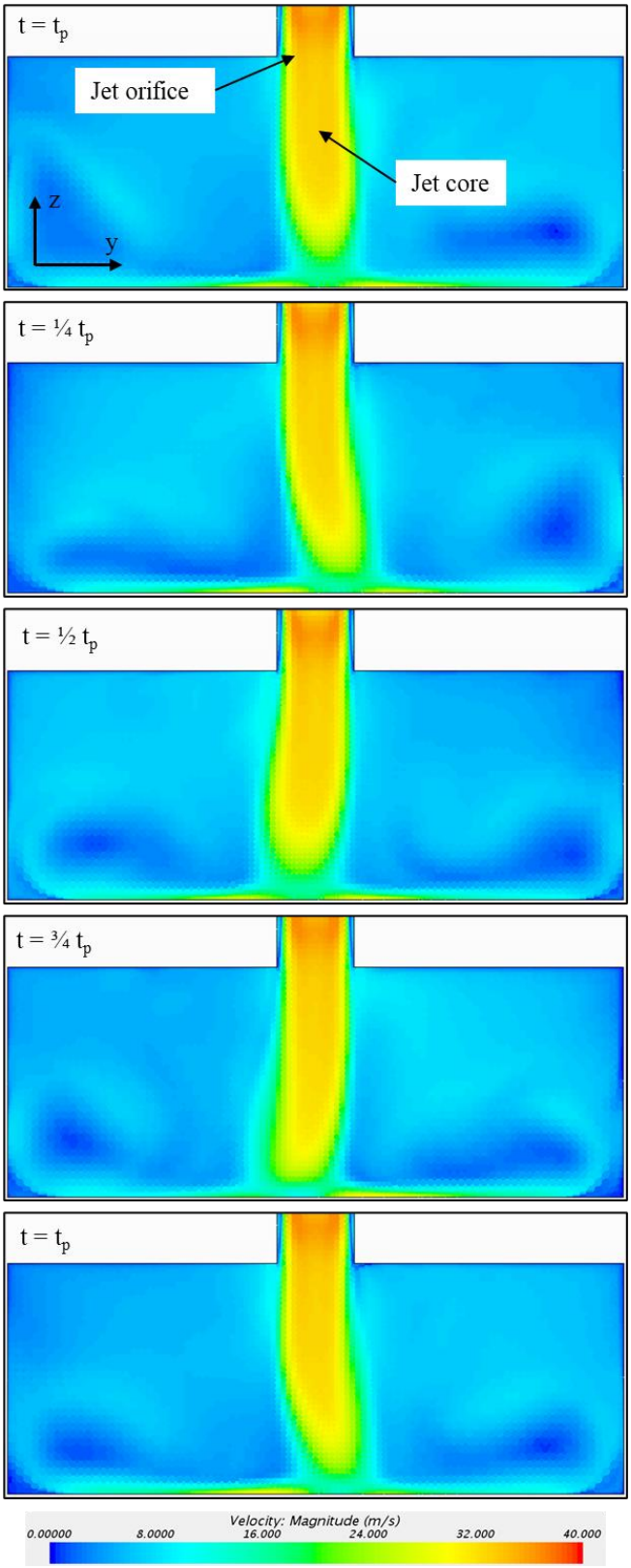

Figure 4.39 Velocity contour of a non-oscillating jet

For a non-oscillating jet case with no cylinder wakes, the jet core is in close proximity to the cylinder. Driving the reattachment of the shear layer separated from the cylinder onto the jet core (shown in Figure 4.6). Hence the cylinder did not shed any vortical structures. Therefore, a few similar cases tested in the spectral analysis led to no cylinder wake frequency peaks.

Summarizing the results of the flow feature analysis of jet oscillation, the deformed jet core oscillates in both lateral and angular directions. The jet oscillation is primarily driven by the cylinder wakes. Also, non-synchronous jet core wakes are produced, reducing the effectiveness of cylinder wakes for jet oscillation. The wall jet also oscillates in a lateral and angular direction but lags behind the jet core. The wall jet curling at the sidewall is observed under the crossflow effect.

The non-oscillating jet case flow features exhibit no lateral deflection or angular rotation of the jet core. Due to the reattachment of the shear layer onto the jet core. However, jet core irregular angular rotation is observed for the non-oscillating jet cases with cylinder wake shedding (at a higher cylinder-jet distance). The cylinder wakes did interact with the jet core and imparted energy into the jet, but the vortex strength is insufficient to induce jet oscillation.

4.3.5. Heat Transfer Results

The final objective of the current study is to derive an optimum design of jet oscillation for maximum heat transfer rate. Therefore, the effect of oscillating cases and non-oscillating jet cases on heat transfer rate are studied. The parameters varied are the velocity ratio and cylinder-jet distance similar to the previous section. And, the cylinder diameter is a constant, d = 2D.

4.3.5.1. Local Nusselt Number

The local Nusselt number contour plots are used to investigate the effect of oscillating and non-oscillating jets on heat transfer rate. For all contour plots, the x-axis and y-axis values are non dimensionalized by the jet diameter (D). And the geometrical position of the jet orifice is used as the origin (0,0). The crossflow is moving from left to right of the page. The cylinder is located at a cylinder-jet distance (S/d) from the origin, upstream towards the left of the page.

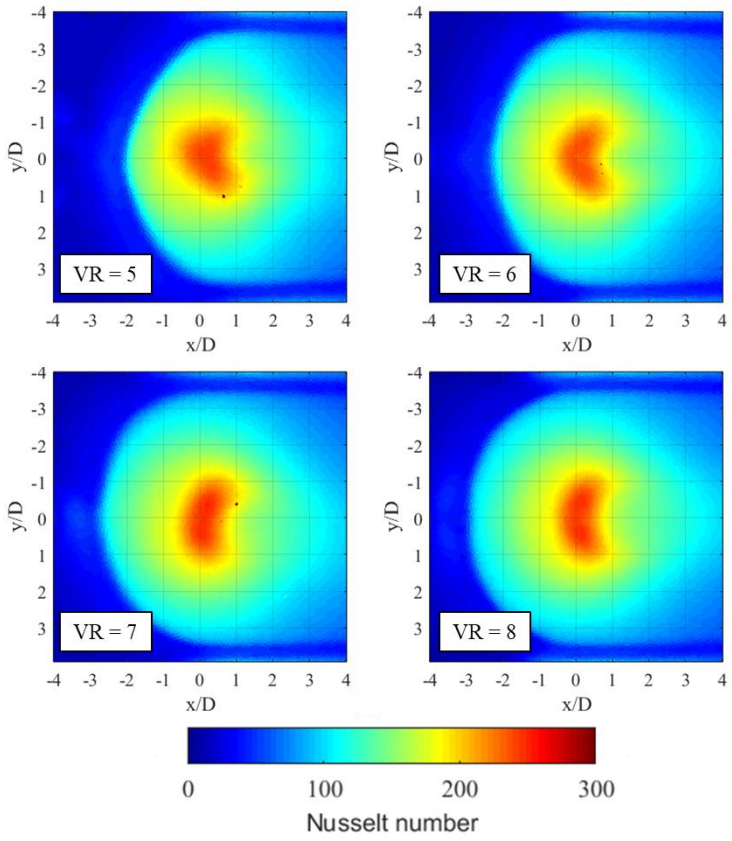

Figure 4.40 Nusselt number distribution at varying VR and S/d = 2

Figure 4.40 shows the local Nusselt number distribution for various velocity ratios tested at S/d = 2. It can be observed that the stagnation region Nusselt number for all the

velocity ratios are similar, with a bean shape in nature. This shape is formed due to crossflow-jet interaction, pushing the jet downstream. The outer boundary observed represents the extent of the wall jet region. The shape of the wall jet region does change with the velocity ratio. The crossflow velocity compresses the wall jet region. And the wall jet compression is proportional to the velocity ratio. The previous results confirmed no jet oscillation for all the velocity ratios tested for S/d = 2. The jet oscillation primarily intends to spread the stagnation region. However, as expected for non-oscillating cases (S/d = 2), the local Nusselt number data show no change in the shape of the stagnation region observed. And the observed shape of the stagnation region can be used to confirm future non-oscillating cases.

Figure 4.41 shows the local Nusselt number distribution for various velocity ratios tested at S/d = 3. The previous results confirmed jet oscillation only for the velocity ratio, VR = 4 & 4.5. The effect of jet oscillation can be observed from the change in the shape of the stagnation region. The Nusselt number distribution for velocity ratio, VR = 4, is the lowest compared to all other velocity ratios tested. Although jet oscillation is observed for this velocity ratio (VR = 4), the decrease in Nusselt number suggests the heat transfer capability of the jet is deteriorated by the high crossflow strength.

The Nusselt number distribution for the other oscillating jet case (VR = 4.5) shows the stagnation region is spread outwards uniformly in the spanwise direction (y/D). Also, the wall jet region downstream appears to be enhanced in a spanwise direction. The stagnation region Nusselt number is the highest compared to all other velocity ratios, hence the best performing oscillating jet case for S/d = 3. The stagnation region Nusselt number distribution for the velocity ratios, VR = 5 – 6, resembles the bean shape

observed for the non-oscillating cases (S/d = 2). Also, the previous spectral analysis did certify non-oscillating jet for velocity ratios, VR = 5 – 6.

Comparing results for the two oscillating cases (VR = 4 &4.5), a decrease in stagnation region Nusselt number is observed for the velocity ratio, VR = 4. Thus, suggesting the vortex strength is too high in VR = 4 to cause an acceptable increase in uniform Nusselt number distribution. And the vortex strength of the velocity ratio, VR = 4.5, leads to uniform Nusselt number distribution.

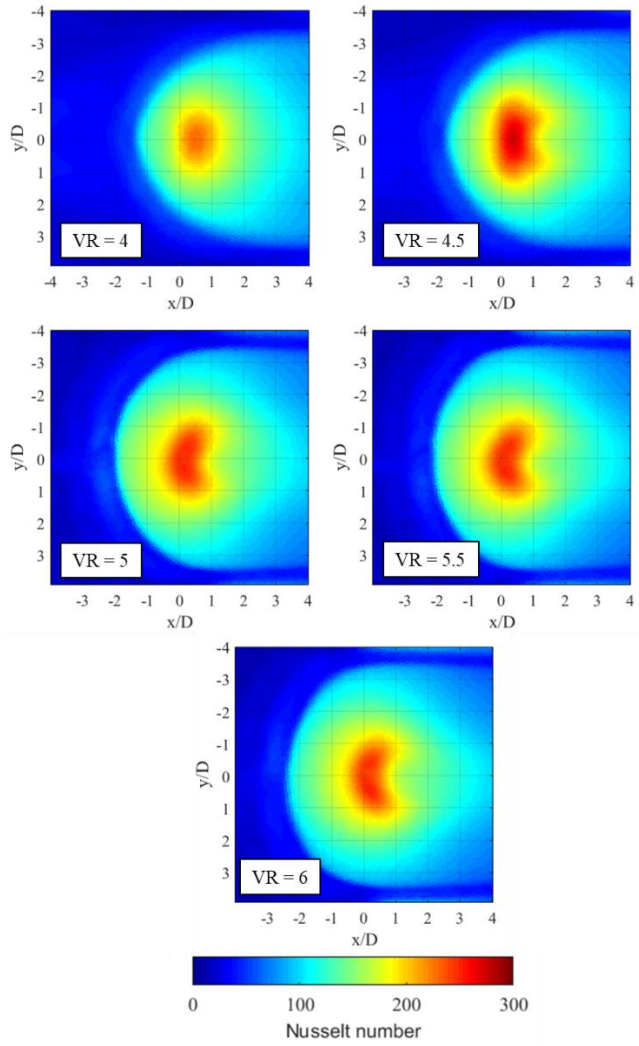

Figure 4.41 Nusselt number distribution at varying VR and S/d = 3

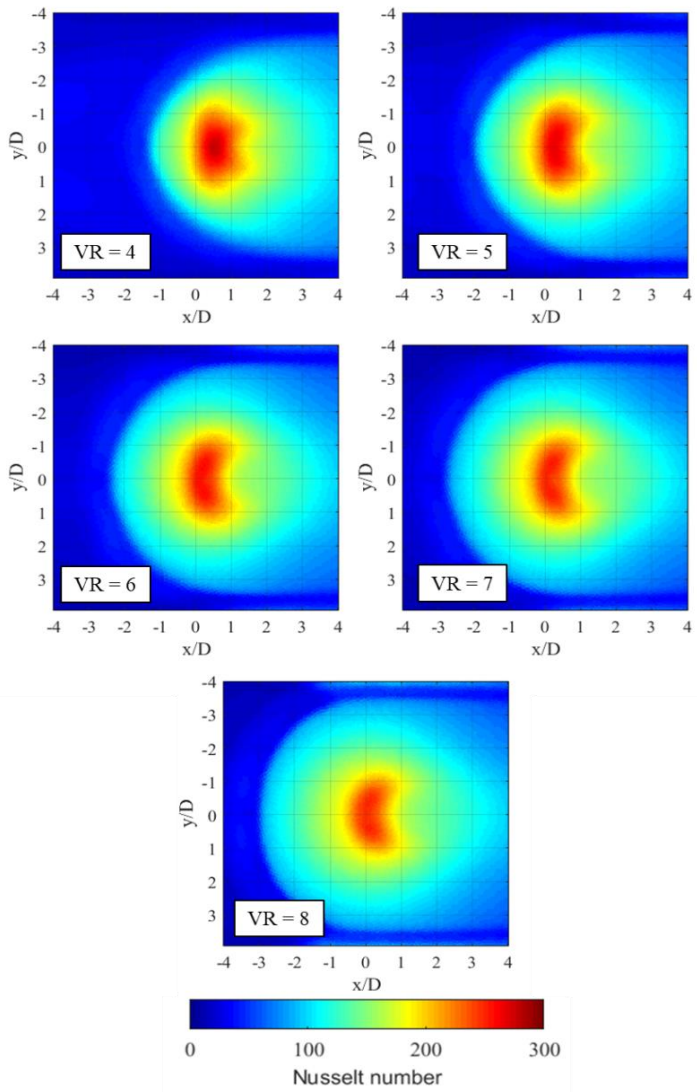

Figure 4.42 Nusselt number distribution at varying VR and S/d = 4

Figure 4.42 shows the local Nusselt number distribution for various velocity ratios tested at S/d = 4. From the CFD spectral analysis, the oscillating jet cases are velocity ratios, VR = 4 & 5. The shape of the stagnation region Nusselt number of velocity ratios, VR = 4 & 5, does resemble the oscillating jet case of S/D = 3 (VR = 4.5). The stagnation region Nusselt distribution is highest for velocity ratio, VR = 4. The Nusselt number distribution for velocity ratios, VR = 6 – 8, is similar to the non-oscillating cases

discussed earlier.

For quantitative comparison discussed in the next section, a steady jet impingement case with no crossflow is investigated for the same jet Reynolds number, Re_j = 38,000. The velocity ratio of this case can be calculated to be VR = ∞. The local Nusselt number distribution is shown in Figure 4.43. The high Nusselt number stagnation region is observed at the geometrical point of impingement (0,0). Also, an outer circle of a high heat transfer rate is observed, representing the secondary peak formed. Lastly, the Nusselt number radially decays outwards.

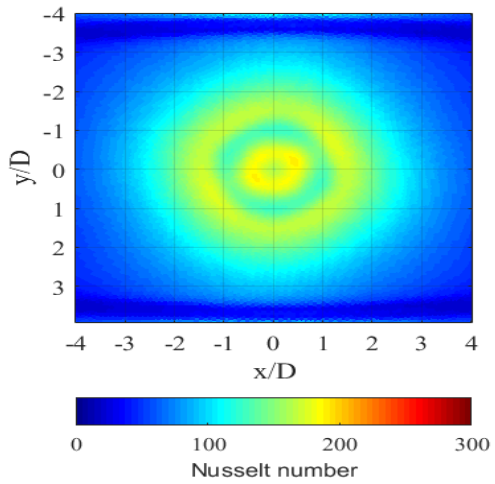

Figure 4.43 Local Nu distribution of steady jet impingement

4.3.5.2. Spanwise Average Nusselt Number

The spanwise average Nusselt number is analyzed for quantitative comparison of oscillating and non-oscillating jet cases. The spanwise average Nusselt number is calculated by averaging the local Nusselt number in the x-direction.

The spanwise average Nusselt number for various velocity ratios at S/d = 2 is shown

in Figure 4.44. The adverse effect of crossflow velocity on Nusselt number distribution is observed. The crossflow velocity is inversely proportional to the velocity ratio. The peak Nusselt number is pushed downstream by the crossflow velocity. The peak for velocity ratio, VR = 8, is offset downstream to x/D = 0.48. The stagnation peak offset decreases with the increase in velocity ratio. The non-oscillating cases discussed here show similar Nusselt number distribution with crossflow effects.

The spanwise average Nusselt number for the steady jet (VR = ∞) shows a maximum peak at the geometrical point of impingement. Also, a secondary peak effect on the spanwise average result is observed at x/D = ±1.

Comparing the non-oscillating jet cases with the steady-state jet case (VR = ∞), the crossflow significantly affects the wall jet region Nusselt number. The peak magnitudes of the non-oscillating cases are higher than the steady jet case due to the crossflow compressing the jet flow features. The upstream wall jet region Nusselt number decreases due to the wall jet advancing against the crossflow. However, the wall jet is assisted by the crossflow in the downstream direction in enhancing the heat transfer rate.

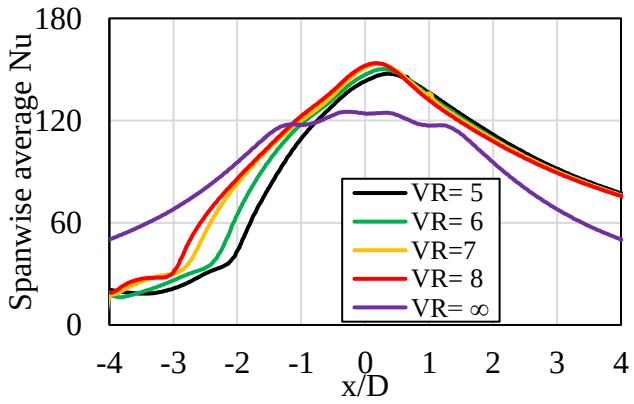

Figure 4.44 Spanwise average Nusselt number for S/d = 2

The spanwise average Nusselt number for various velocity ratios at S/d = 3 is shown in Figure 4.45. The previous results conclude jet oscillation only for velocity ratios, VR = 4 & 4.5. The spanwise average Nusselt number results suggest the non-oscillating jets are outperforming the oscillating jets. However, the jet is intended to oscillate laterally and spread the stagnation region in the spanwise direction (y/D). Hence, the spanwise average Nusselt number suppresses the effect of jet oscillation. The increase in Nusselt number for the non-oscillating cases is mainly due to the crossflow effect, verified by the offset of the stagnation peak for the oscillating jets. The non-oscillating jets share the same Nusselt number with a minimum crossflow effect.

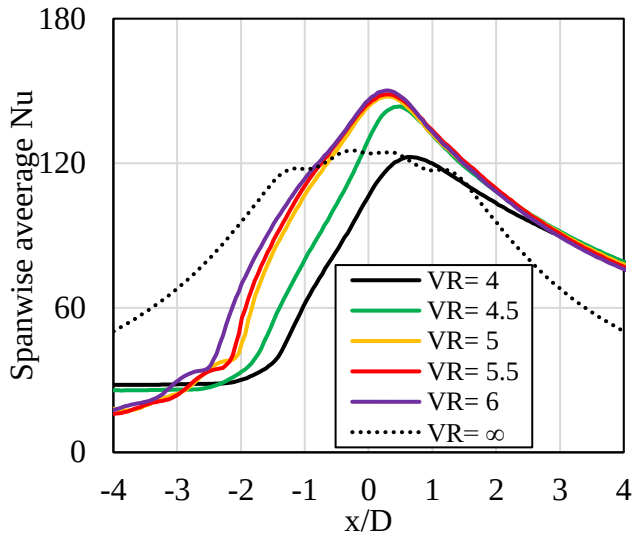

Figure 4.45 Spanwise average Nusselt number for S/d = 3

Comparing the peak Nusselt number, the lowest magnitude is found for the oscillating case with velocity ratio, VR = 4 (Figure 4.45). The peak Nusselt number increases by a maximum of 20% for the rise in velocity ratio of VR = 4 to 4.5. however,

the change in peak magnitude decrease to 3% for the change in velocity ratio of VR = 4.5 to 5. And less than 1% change in peak magnitude for velocity ratios, VR = 5 – 6. Thus, suggesting the increase in peak Nusselt number for the raise in velocity ratio is exponential.

The oscillating jet case (VR = 4) and the steady jet case (VR = ∞) share the same peak Nusselt number magnitude, and the Nusselt number distribution upstream is greatly affected by the crossflow. The oscillating jet case, VR = 4.5, has comparatively better performance in heat transfer rate in the stagnation region compared to the steady jet case.

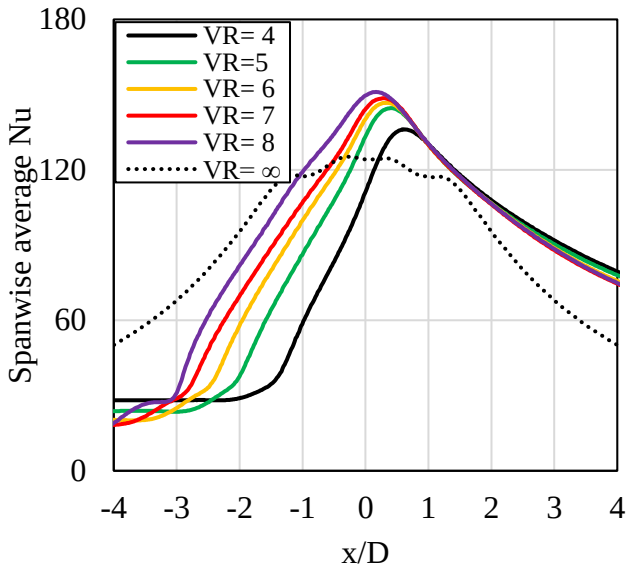

Figure 4.46 Spanwise average Nusselt number for S/d = 4

Figure 4.46 shows the spanwise average Nusselt number for various velocity ratios at S/d = 4. The Nusselt number distribution for the non-oscillating cases changes substantially with velocity ratio than the SD = 2 & 3 results. The stagnation region Nusselt number for the oscillating jet cases (VR = 4 & 5) is higher than the steady jet

case result. A similar effect of crossflow strength on the spanwise average results for the change in velocity ratio continues.

Summarizing spanwise average Nusselt results, the Nusselt number distribution is significantly affected by the crossflow strength. The peak Nusselt number determined for all the non-oscillating cases falls within 2% of Nu = 153. Thus, the oscillating jet cases thermal performance is less than the non-oscillating jet cases. However, the jet oscillates in the spanwise direction; hence the spanwise average results are not appreciated for comparing oscillating and non-oscillating jet cases.

4.3.5.3. Streamwise Average Nusselt Number

As discussed above, to understand the effect of the spanwise oscillating jet on thermal performance, the Nusselt number is averaged in the streamwise direction. For a fair comparison of streamwise average Nusselt number, Nusselt number is averaged in streamwise direction x = ±1D from their stagnation peak. The streamwise averaging is limited to x = ±1D to study the effect of the stagnation region Nusselt number, expecting the oscillating jet to spread the stagnation region. An example showing the area considered for streamwise averaging for the oscillating jet case (S/d = 4 & VR = 4) is shown in Figure 4.47.

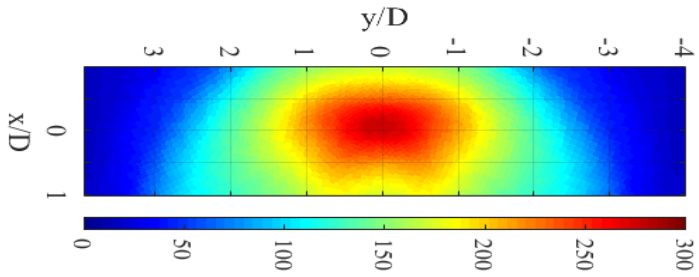

Figure 4.47 Stagnation region offset by x/D = -0.78 for streamwise averaging

The streamwise average Nusselt number for various velocity ratios at S/d = 2 is shown in Figure 4.48. The stagnation region (y/D = ±1) Nusselt number shows two small peaks similar to the steady jet case. However, the overall Nusselt number distributions for all the non-oscillating jet cases are identical to each other. The non-oscillating jet shows a maximum increase of 28% in streamwise average Nusselt number compared to the steady jet case. And this increase is due to the crossflow compressing the jet flow features.

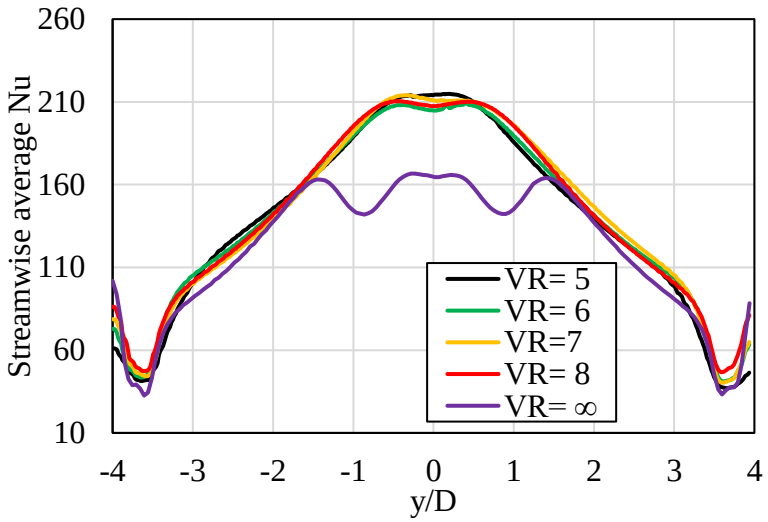

Figure 4.48 Spanwise average Nusselt number for S/d = 2

The streamwise average Nusselt number for various velocity ratios at S/d = 3 is shown in Figure 4.49. The increase in uniform heat transfer rate in the stagnation region for the oscillating jet case (VR = 4.5) can be observed compared to non-oscillating cases. The stagnation region of the oscillating case is found to be plateau with an increase of 7% in Nusselt number from the two-peak valley of the non-oscillating case. The oscillating case (VR = 4) result shows an overall reduction in Nusselt number because the crossflow suppresses the effect of jet oscillation. The oscillating jet results conclude a maximum

increase of 35% in streamwise average Nusselt number compared to the steady jet case. However, there is a reduced heat transfer rate near the sidewall due to the crossflow.

The Nusselt number distribution for the non-oscillating cases (VR = 5 – 6) shows similar findings to S/d = 2 results. Compared to the steady jet case, the non-oscillating case leads to a maximum increase of 26% in streamwise average Nusselt number.

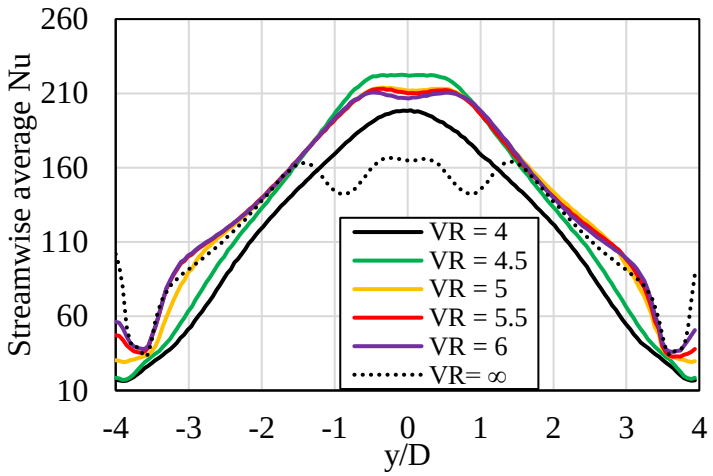

Figure 4.49 Streamwise average Nusselt number for S/d = 3

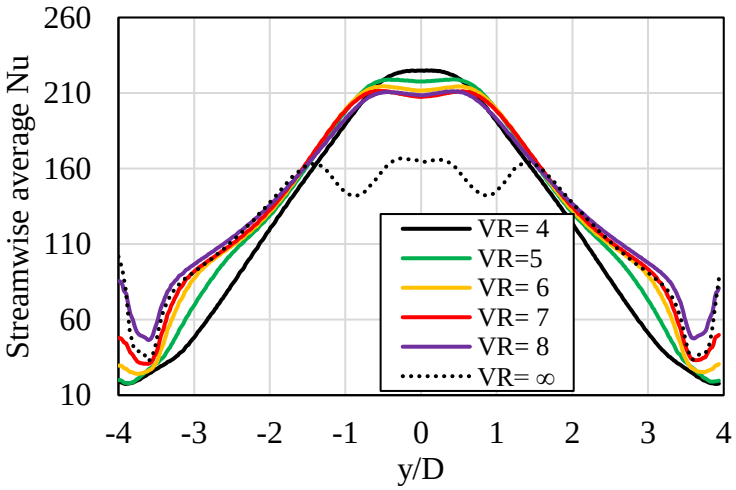

Figure 4.50 Streamwise average Nusselt number for S/d = 4

Figure 4.50 shows the streamwise average Nusselt number for various velocity ratios at S/d = 4. The maximum heat transfer rate is observed for the oscillating jet case (VR = 4 – 5) results, with a maximum increase of 36% in the Nusselt number. The non-oscillating jet cases show a maximum increase of 27% in Nusselt number compared to the steady jet case. Also, there is a reduction in the Nusselt number for the oscillating jet case compared to the non-oscillating jet case closer to the sidewall.

Summarizing the streamwise average results, The non-oscillating cases for S/d = 2, 3 and 4, show the same increase of 27% in Nusselt number in the stagnation region. This is expected as the local stagnation region Nusselt number results show no change in the contour for the non-oscillating jet cases. However, a maximum increase of 36% is observed for the oscillating jet cases compared to the steady jet case. Also, the streamwise averaged Nusselt number is uniformly distributed compared to the non-oscillating and steady jet case.

4.3.5.4. Area Average Nusselt Number

The area-averaged Nusselt number is calculated to determine the overall effect of the oscillating and non-oscillating jet case. The area considered for averaging is the same x = ±1D stagnation region shown in Figure 4.47. The area-averaged Nusselt number result for the velocity ratio and cylinder-jet distance tested is shown in Figure 4.51. For thermal comparison with the steady jet case, the individual test results are divided by the steady jet case average Nusselt number, $Nu_0 = 92.17$.

The results show an increase in the average Nusselt number with the increase in velocity ratio. This increase proves that although the jet oscillates for Velocity ratio, VR = 4 – 5 at S/d = 3 & 4, the effect of crossflow is dominant in area-averaged Nusselt

number. It can be observed that the Nusselt number decreases with the increase in cylinder-jet distance; however, the S/d = 2 shows a minimum change in the Nusselt number.

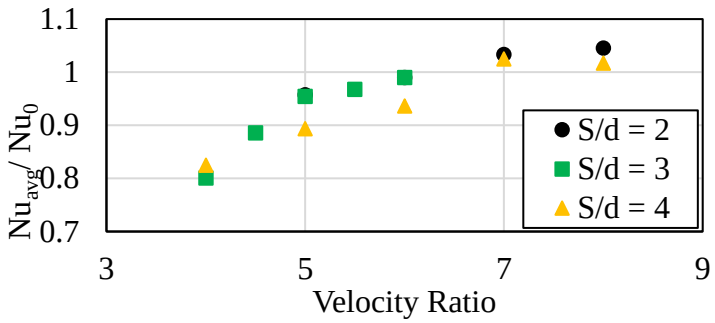

Figure 4.51 Area average Nusselt number for varying velocity ratios

4.4. Experimental Results

The final experimental analysis includes investigating the effect of velocity ratio, cylinder diameter, and cylinder-jet distance on jet oscillation. The range of velocity ratios and cylinder-jet distances tested is similar to the final CFD analysis. However, additional velocity ratios were tested for detailed analysis. The range of velocity ratios tested depended on their previous test results. The method employed, is to increase the velocity ratio till the maximum possible streamwise average Nusselt number is reached compared to the steady jet case. The jet Reynolds number is kept constant for all the cases tested at Re_j = 38,000.

The uncertainty analysis of the experimental results showed a maximum area-averaged Nusselt number error of ±9.8%, jet Reynold's number error of ±2.3%, and velocity ratio error of ±3.6%

4.4.1. Validation

The experiment heat transfer result is validated from the literature work of Florschuetz et al., 1980 similar to CFD validation. The same test case validated in the CFD result is tested experimentally. The averaging scheme is identical to literature work and CFD validation, shown in Figure 4.25.

The segment average Nusselt number for literature, experimental, and CFD result is shown in Figure 4.52. Comparing experimental and literature results, the stagnation region (Segment 2) Nusselt Number is predicted within the error limit of the literature result. However, the CFD result at the stagnation region Nusselt number is over predicted. The segment 2 & 3 experimental results have the maximum error due to the data corrupted by the heater strip junction. Therefore, the result showcased in this paper comprises only data near the stagnation region and excludes the data near the heater junction area.

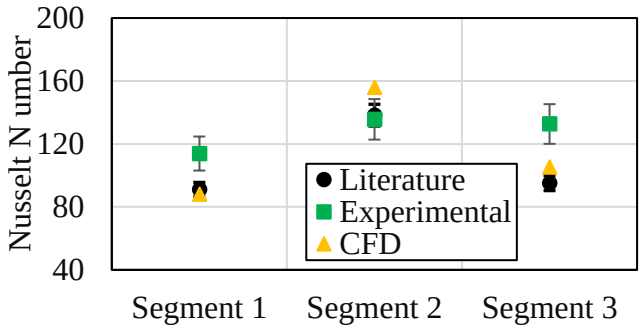

Figure 4.52 Experimental result validation segment average Nu

4.4.2. Spectral Analysis

An FFT analysis of the target wall pressure fluctuation is analyzed similarly to previous spectral analysis for cylinder diameter, d = 2D, and 3D at various velocity ratios

and cylinder-jet distance. The spectral analysis will aid in differentiating oscillating and non-oscillating jet cases. The method employed to distinguish the oscillating and non-oscillating jet case is as discussed before. If a frequency peak of twice the cylinder wake frequency exists in the frequency spectrum of pressure measurement, it confirms jet oscillation. To determine cylinder wake frequency, the target wall pressure fluctuation is measured downstream of the cylinder in the absence of the jet. The frequency spectrum of the pressure fluctuations for cylinder diameters, d = 2D, and 3D are analyzed, and the cylinder wake frequency are summarized in Table 4.6 and Table 4.7, respectively.

Table 4.6

Cylinder wake frequency of cylinder diameter, d = 2D

Velocity Ratio	Frequency, Hz
4	28.59
5	25
6	22
7	18.79
8	16.49
10	13.56
12	11.23

Table 4.7

Cylinder wake frequency of cylinder diameter, d = 3D

Velocity Ratio	Frequency, Hz
4	23.59
6	17.06
8	13.26
10	10.7
12	8.9
15	7.1

The Strouhal number can be calculated using the frequency and their respective velocity. The Strouhal number for cylinder diameter, d = 2D and 3D is equal to, St = 0.26 and 0.30, respectively. The Strouhal number is higher for the cylinder diameter, d = 3D, due to the increase in blockage ratio. The cylinder wake frequency tabulated will be used for differentiating oscillating and non-oscillating jet cases.

4.4.2.1. Spectral Analysis of Stagnation Pressure at d = 2D

The spectral analysis is carried for various velocity ratios, VR = 4 – 12 and cylinder-jet distances, S/d = 2 – 4. Figure 4.53 shows the frequency spectrum of pressure fluctuations at various velocity ratios at a cylinder-jet distance of S/d = 2. The results show no frequency peaks for all the velocity ratios tested; hence, all the cases are non-oscillating jets. Also, these results are in match with the CFD results confirming the jet core is in the recirculation region with no oscillations.

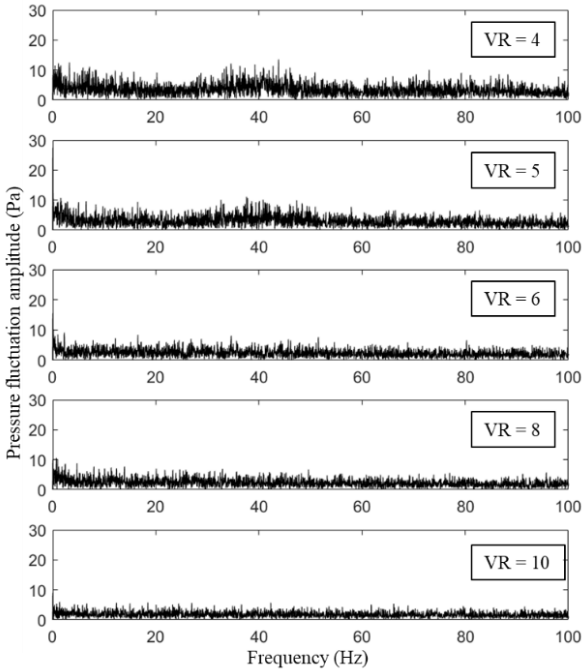

Figure 4.53 Frequency spectrum of stagnation pressure at S = 2d & d = 2D

The frequency spectrum of stagnation pressure at various velocity ratios at S/d = 3 is shown in Figure 4.54. The results show frequency peaks for velocity ratios, VR = 4 – 6, and the frequency is equal to twice the cylinder wake frequency. Hence the velocity ratios, VR = 4 – 6, are concluded oscillating jet cases. Whereas, with no frequency peaks the velocity ratios, VR = 7 – 12 is considered non-oscillating jets. However, the CFD results show jet oscillation only for velocity ratios, VR = 4 – 4.5. Concluding the vortex strength required for jet oscillation is overpredicted by the CFD simulation.

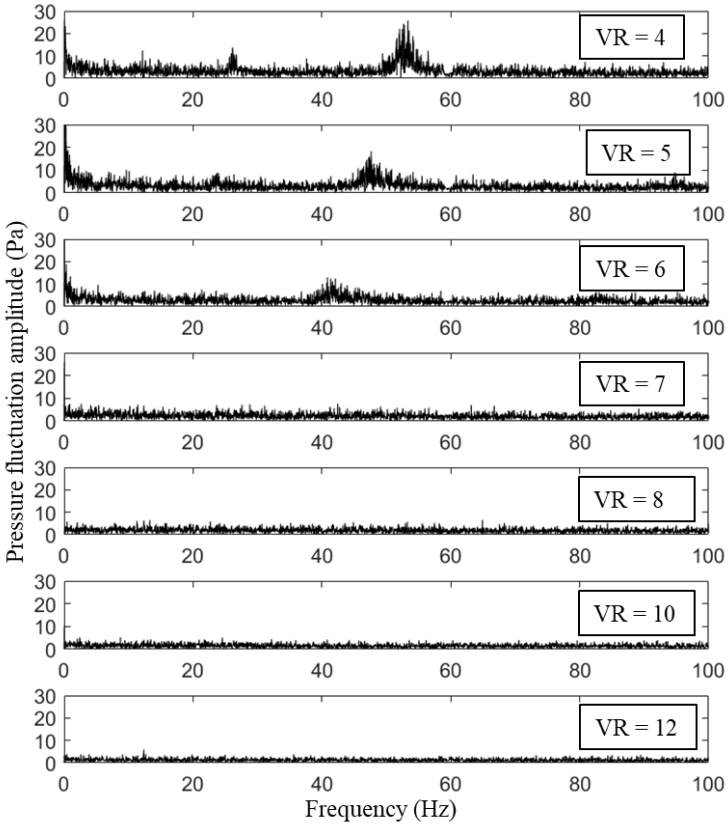

Figure 4.54 Frequency spectrum of stagnation pressure at S = 3d & d = 2D

Figure 4.55 shows the frequency spectrum of pressure fluctuations at various velocity ratios at a cylinder-jet distance of S/d = 4. The results confirmed jet oscillation for

velocity ratios, VR = 4 – 8 with frequency peaks. The frequency spectrum shows no peaks for velocity ratios, VR = 10 and 12, confirming these as non-oscillating jet cases.

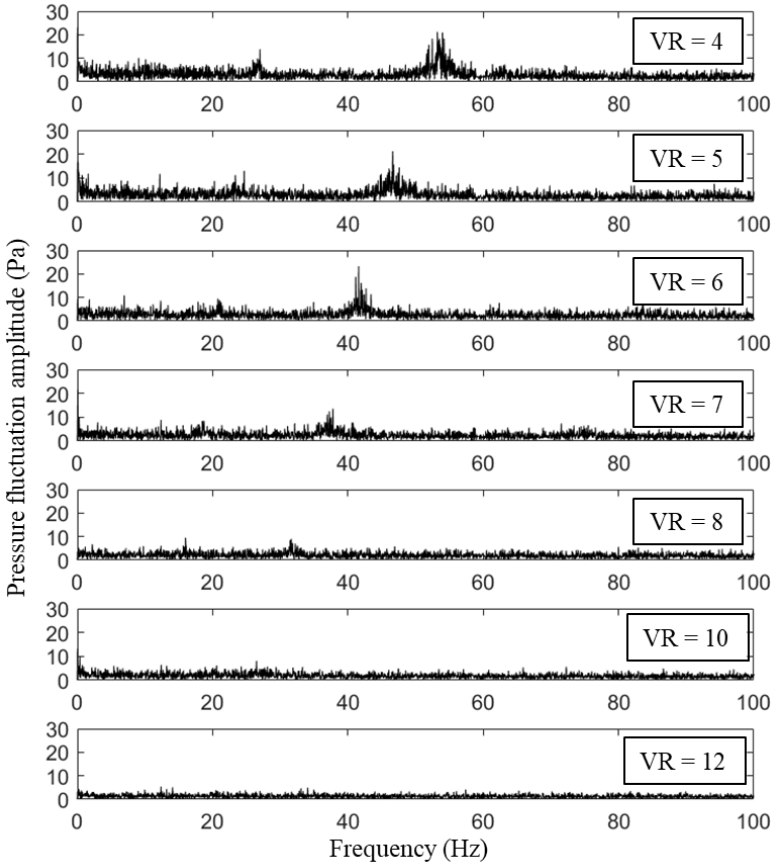

Figure 4.55 Frequency spectrum of stagnation pressure at S = 4d & d = 2D

4.4.2.2. Spectral Analysis of Stagnation Pressure at d = 3D

The spectral analysis is carried out for various velocity ratios, VR = 4 – 15 and cylinder-jet distances, S/d = 3. Figure 4.56 shows the frequency spectrum of pressure fluctuations at different velocity ratios at a cylinder-jet distance of S/d = 3. The results show frequency peaks for velocity ratios, VR = 4 – 10 leading to jet oscillation. The remaining cases with no peaks can be concluded as non-oscillating jet cases.

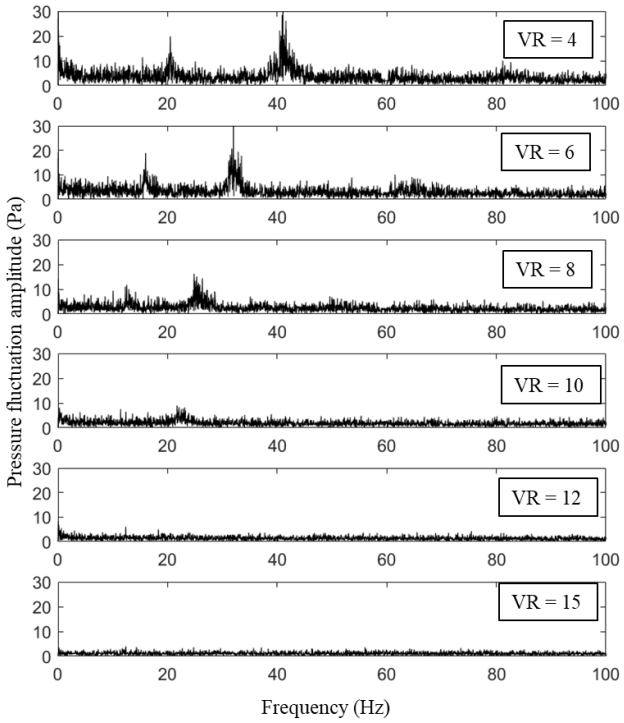

Figure 4.56 Frequency spectrum of stagnation pressure at S = 3d & d = 3D

Summarizing the spectral analysis results, the cases tested are sorted into oscillating and non-oscillating jet cases. The experimental results confirm the jet oscillates for higher velocity ratios than the CFD findings. This confirms the CFD overpredicts the momentum required for jet oscillation.

4.4.3. Heat Transfer Results

The experimental heat transfer result is the crucial element of this current research to determine the effect of jet oscillation on heat transfer rate. The parameters varied are the velocity ratio, cylinder diameter, and cylinder-jet distance. For a cylinder diameter of, d = 2D the velocity ratio is varied from, VR = 3 – 15, and the cylinder-jet distance is varied for S/d = 2, 3, & 4. Later the cylinder diameter, d = 3D, is tested for the optimum cylinder-jet distance and varying velocity ratios.

4.4.3.1. Local Nusselt Number

The target wall local Nusselt number contour plots are used to investigate the local effect of oscillating and non-oscillating jets on heat transfer rate. For all contour plots, the x-axis and y-axis values are non dimensionalized by the jet diameter (D). The geometrical position of the jet orifice is used as the origin (0,0). The crossflow is moving from left to right of the page. The corrupted data are not shown in the contour plots; hence blank areas are observed in the following figures.

Figure 4.57 shows the local Nusselt number distribution for tested velocity ratios at S/d = 2 and d = 2D. The spectral analysis concluded all velocity ratios led to non-oscillating jet cases. The stagnation region Nusselt number shows the deformed jet core shape (bean shape) from the previous result. The wall jet boundary limit is governed by the crossflow strength, similar to the earlier findings. Also, the Nusselt number distribution is proportional to the velocity ratio.

Figure 4.58 shows the local Nusselt number distribution for the various velocity ratios tested at S = 3d and d = 2D. The previous results confirmed jet oscillation only for the velocity ratio, VR = 4 – 6. The local Nusselt number plots show the bean shape is dominant for velocity ratios, VR = 4 – 8. But the shape of the oscillating jet core does not match the unique shape found in the CFD results. Also, the maximum Nusselt number is observed for the oscillating jet case with velocity ratio, VR = 6. The lateral spread of stagnation region heat transfer coefficient increases with the increase in velocity ratio. This shows the oscillating jet core is leading to the lateral deflection and angular rotation of the wall jet. Also, the curling of the wall jet is reduced with a decrease in crossflow strength.

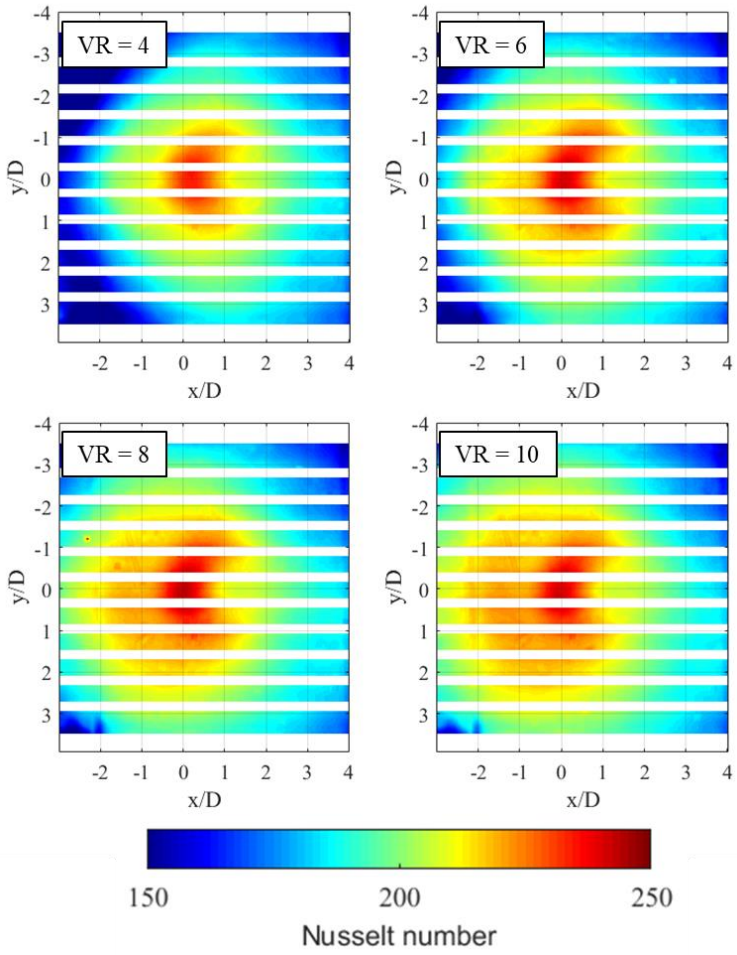

Figure 4.57 Nusselt number distribution at varying VR at S = 2d and d = 2D

For the velocity ratio VR = 12, the jet core region Nusselt number is the lowest, and also, the shape of the stagnation region is round in nature. This shape proves that the crossflow has a minor effect in compressing the flow features. Also, with the decrease in velocity ratio, the upstream wall jet entered the cylinder recirculation region.

The local Nusselt number distribution for the oscillating and non-oscillating cases at S/d = 4d is shown in Figure 4.59, and the range of velocity ratios tested is VR = 4 – 12. The usual trend of increase in stagnation region Nusselt with velocity ratio is observed. The extent of the upstream wall jet is found to be a maximum of x/D = -3, showing the

wall jet is not in the recirculation region. Hence, cylinder wakes can be shed from the cylinder without interruption. Also, the uniform distribution of Nusselt number in the wall jet region is observed for higher velocity ratios.

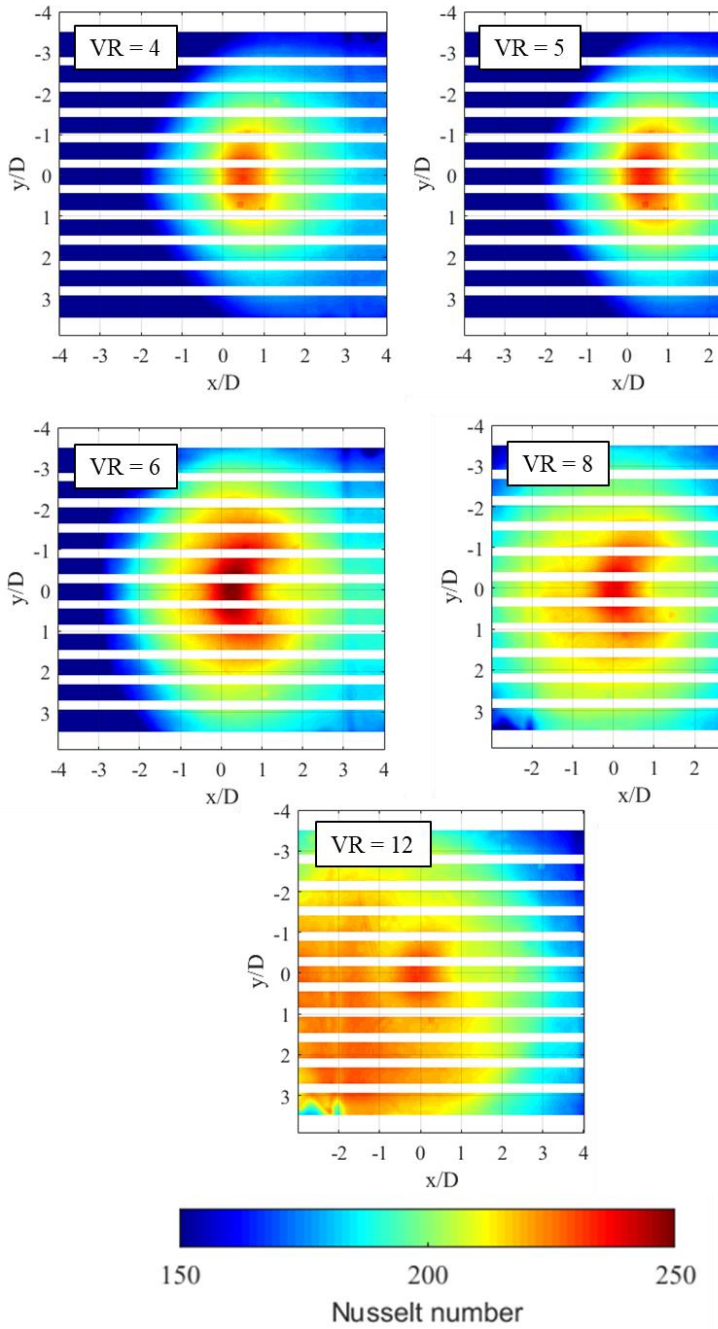

Figure 4.58 Nusselt number distribution at varying VR at S = 3d and d = 2D

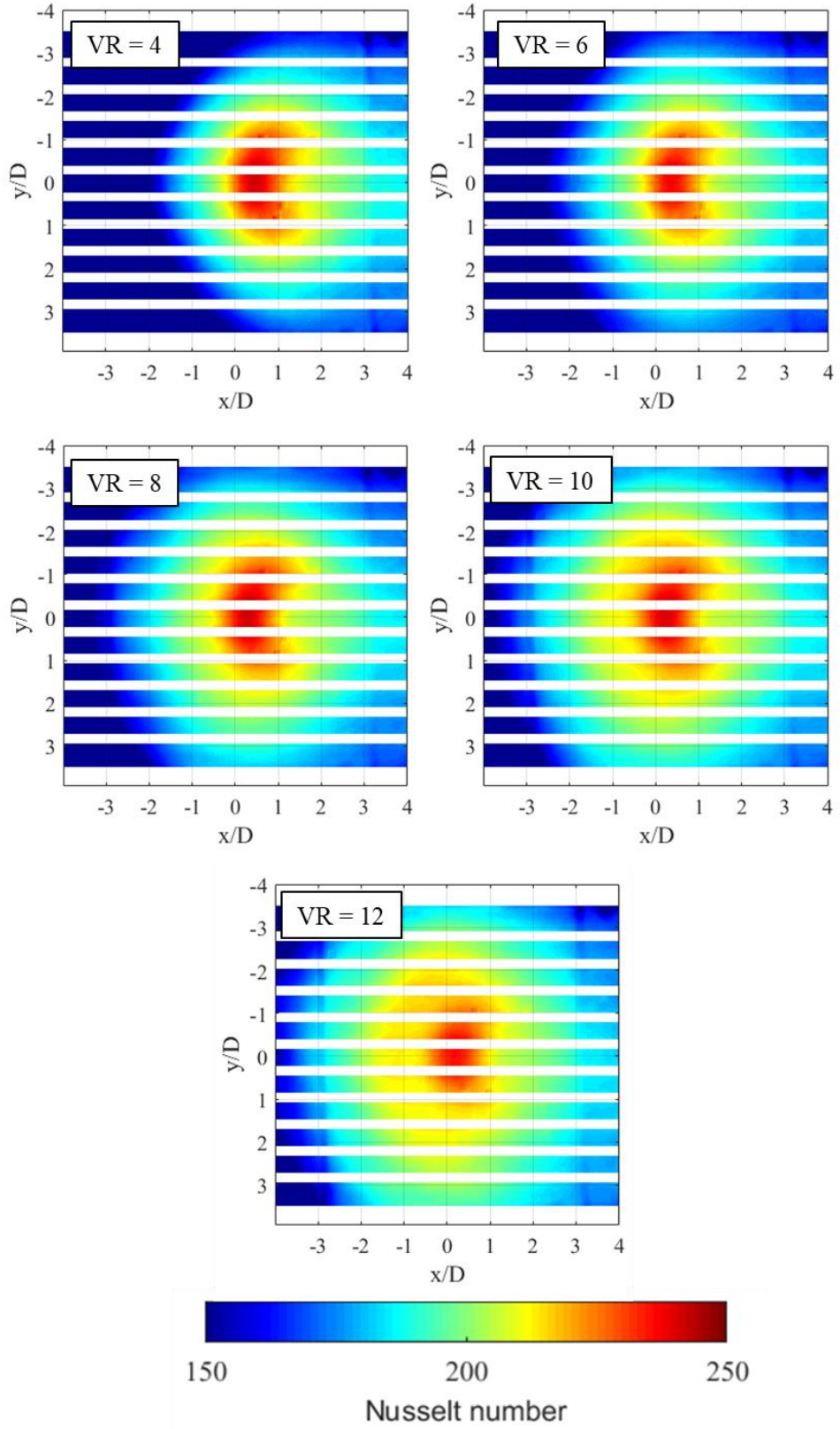

Figure 4.59 Nusselt number distribution at varying VR and S = 4d and d = 2D

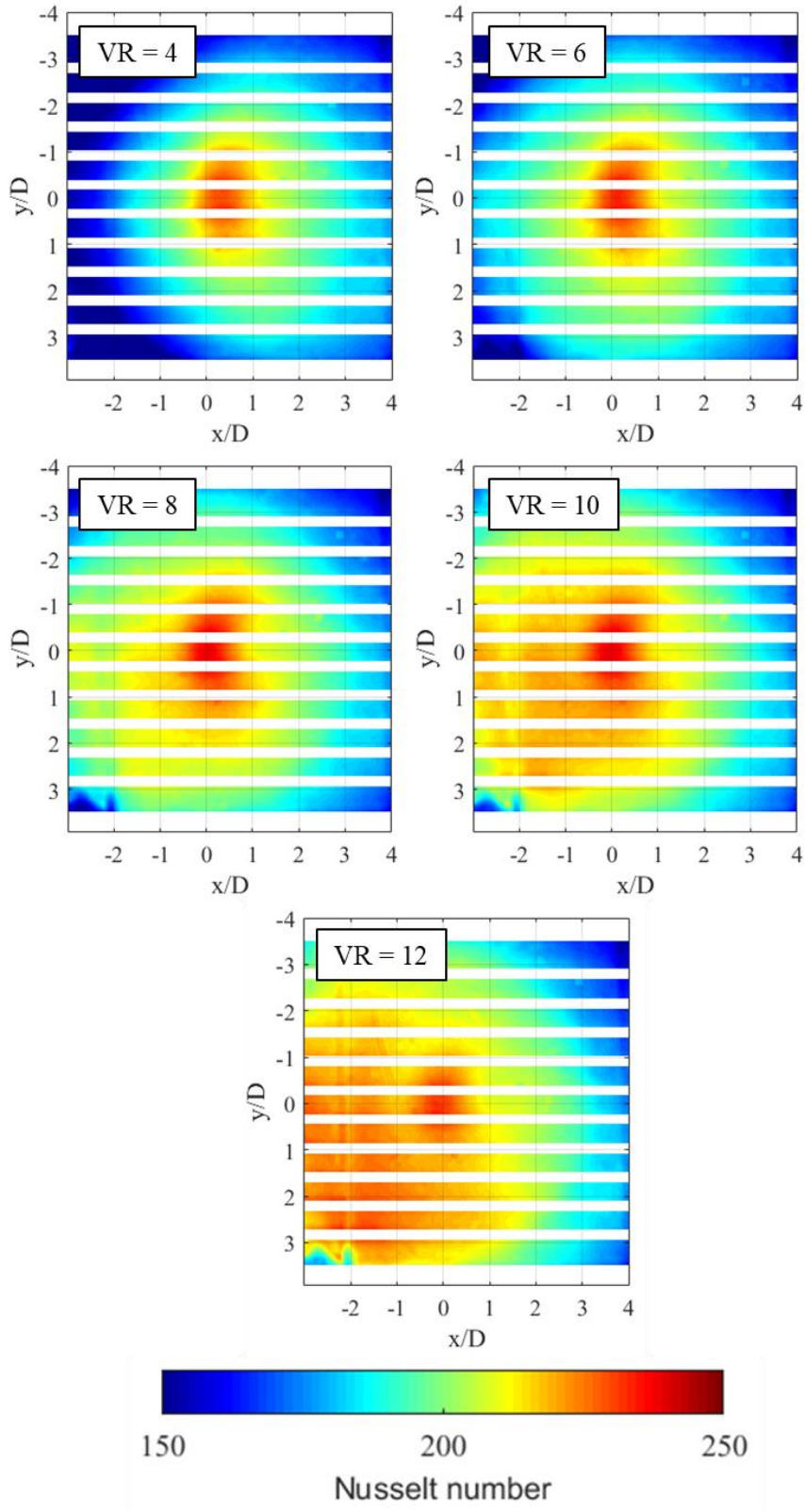

Figure 4.60 Nusselt number distribution at varying VR and S = 3d and d = 3D

Figure 4.60 shows the local Nusselt number distribution for various velocity ratios tested at S = 3d and d = 3D. The spectral analysis concludes jet oscillation for velocity ratios, VR = 4 – 10. The local Nusselt number results for the oscillating and non-oscillating jet cases follow the same stagnation region and wall jet region Nu distribution findings. For the velocity ratios, VR = 8 – 12, the sidewall Nusselt number spreads more uniformly in nature on either side.

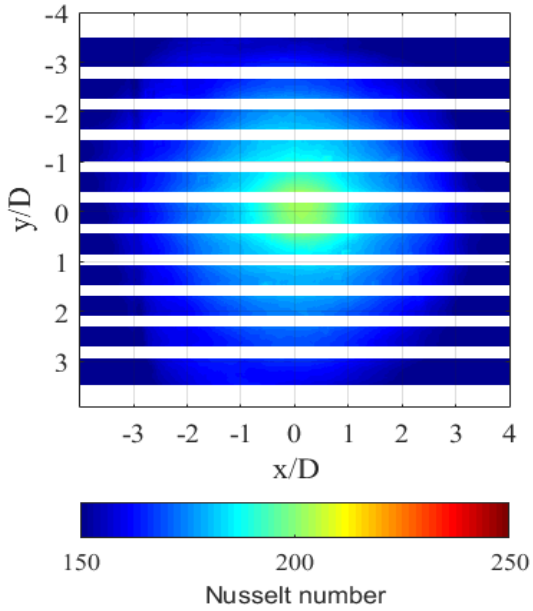

Figure 4.61 Local Nu distribution of steady jet impingement

For quantitative comparison, a steady jet impingement case with no crossflow is investigated for the jet Reynolds number, Re_j = 38,000. The velocity ratio of this case can be calculated to be VR = ∞. The local Nusselt number distribution is shown in Figure 4.61. The high Nusselt number stagnation region is observed at the geometrical point of impingement (0,0). The Nusselt number radially decays outwards from the stagnation

point, similar to the literature findings (O'Donovan et al., 2007). There is no secondary peak formed near the stagnation region, that was observed in the CFD results (Figure 4.43).

Summarizing the experimental spanwise average results, the stagnation region bean shape is dominant in both oscillating and non-oscillating jet cases. And the wall jet region is spread laterally in the y-direction with the increase in velocity ratio.

4.4.3.2. Spanwise Average Nusselt Number

The spanwise average Nusselt number is analyzed for quantitative comparison of oscillating and non-oscillating jet cases. The spanwise average Nusselt number is calculated by averaging the local Nusselt number in the x-direction.

The spanwise average Nusselt number for various velocity ratios at S/d = 2 and d = 2D is shown in Figure 4.62. The peak stagnation region Nusselt number magnitude and position are dictated by the crossflow strength, similar to CFD results. The jet core is deflected downstream a maximum distance of x/D = 0.5D, for the velocity ratio, VR = 4. The upstream wall jet region Nusselt number increases with the increase in velocity ratio. And a maximum change of 25% in the Nusselt number is observed at the upstream wall jet region compared to the steady jet case. The curves for all the velocity ratios overlap each other in the downstream wall jet region, suggesting a minimum change in Nusselt number.

Comparing the current results with the steady jet case, the curve for velocity ratio, VR = 10, closely follows the steady jet case result with a higher magnitude. A maximum increase of 20% is observed in the stagnation region. The velocity ratio, VR = 4 results, shows a reduction in heat transfer rate near the upstream wall jet similar to CFD results.

The CFD results also concluded the steady jet case showed maximum Nusselt number compared to other cases in the upstream wall jet region. But the experimental results suggest the non-oscillating cases possess better thermal performance than the steady jet case.

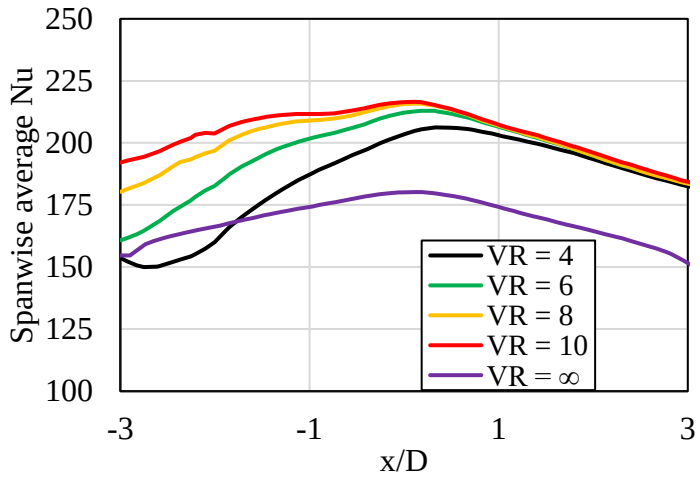

Figure 4.62 Spanwise average Nusselt number for S = 2d and d = 2D

The spanwise average Nusselt number for various velocity ratios at S/d = 3 and d = 2D is shown in Figure 4.63. The previous spectral analysis results conclude jet oscillation only for velocity ratios, VR = 4 – 6. The spanwise average Nusselt number results suggest the non-oscillating jets are outperforming the oscillating jets in the upstream wall jet region. A maximum increase of 94 % in Nusselt number is observed between the velocity ratios, VR = 4 and 12. However, the peak stagnation region Nusselt number is found for the oscillating jet case with VR = 6. The downstream Nusselt number for all the cases tested are in close proximity resulting in minimum change.

The upstream wall jet region Nusselt number of the oscillating jet cases (VR = 4 – 6)

is underperforming compared to the steady jet case. But the oscillating jet overperforms the steady jet case in the stagnation and downstream region, with a maximum increase of 21% in spanwise average Nusselt number.

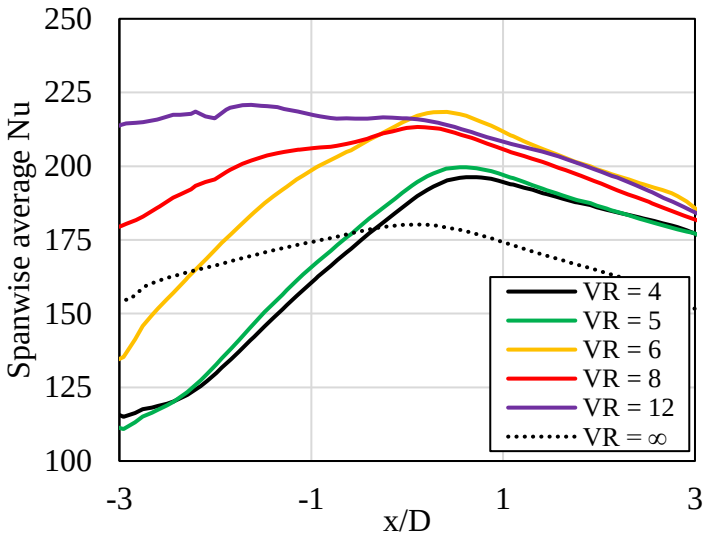

Figure 4.63 Spanwise average Nusselt number for S = 3d and d = 2D

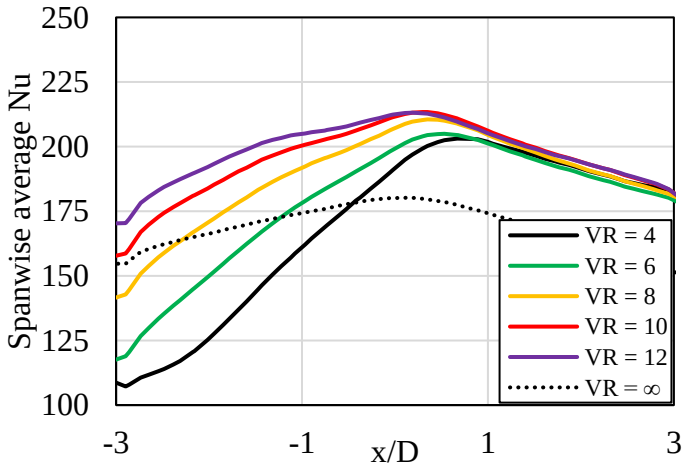

Figure 4.64 Spanwise average Nusselt number for S = 4d and d = 2D

Figure 4.64 shows the spanwise average results for velocity ratios, VR = 4 – 12 at S/d = 4 and d = 2D. The overall trend of the oscillating and non-oscillating jet results is similar to the previous discussion. The change in Nusselt number in the stagnation region is minimum compared to other cylinder-jet distances. A maximum increase of 58% in Nusselt number is observed in the upstream wall jet region for the velocity ratios (VR = 4 & 12).

The non-oscillating case outperforms the steady jet case with a maximum increase of 18% in the stagnation region Nusselt number. On the other hand, the oscillating jet cases (VR = 4 – 8) show reduced heat transfer rate in the upstream region and enhanced heat transfer rate in the stagnation region. A maximum increase of 17.6 % in Nusselt number is observed for the oscillating case, VR = 8 compared to the steady jet case.

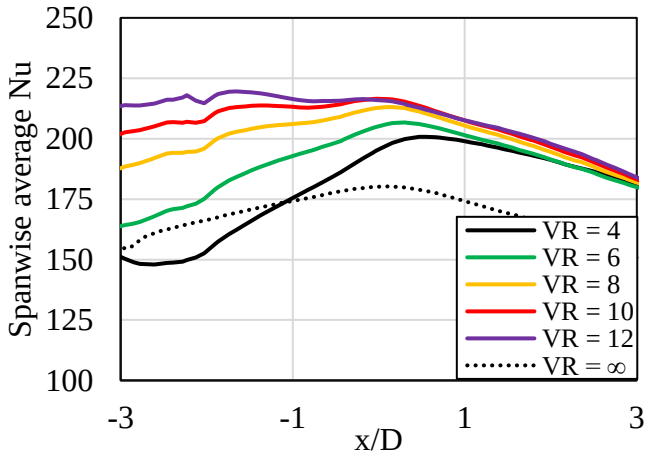

Figure 4.65 Spanwise average Nusselt number for S = 3d and d = 3D

Figure 4.65 shows the spanwise average results for velocity ratios, VR = 4 – 12 at S/d = 3 and d = 3D. The spectral analysis concluded the velocity ratios, VR = 4 – 10, as the oscillating jet cases. The non-oscillating jet case shows a maximum change of 44% in

Nusselt number compared to the oscillating jet case in the upstream wall jet region. The stagnation region Nusselt number increases with the increase in velocity ratio. The effect of the oscillating jet is not significant due to lateral jet oscillation. The downstream wall jet region Nusselt number shows minimum change for the velocity ratios tested.

Summarizing spanwise average Nusselt results, the Nusselt number distribution is significantly affected by the crossflow strength similar to CFD results. The non-oscillating jet enhances heat transfer rate in the upstream region, with a maximum increase of 94% in Nusselt number. And the oscillating jet cases thermal performance is better in the stagnation region than the non-oscillating jet cases. However, the jet oscillates in the lateral direction; hence the spanwise average results are not appreciated for comparing oscillating and non-oscillating jet cases.

4.4.3.3. Streamwise Average Nusselt Number

As discussed above, to understand the effect of the spanwise oscillating jet on thermal performance, the Nusselt number is averaged in the streamwise direction. Therefore, for a fair comparison of streamwise average Nusselt number, Nusselt number is averaged in streamwise direction x = ±1D from their stagnation peak. An example showing the area considered for streamwise averaging for the oscillating jet case is shown in Figure 4.47.

The streamwise average Nusselt number for various velocity ratios at S/d =2 and d = 2D is shown in Figure 4.66. The overall Nusselt number distributions for all the non-oscillating jet cases are in close proximity. The non-oscillating jet shows a maximum increase of 15% in streamwise average Nusselt number compared to the steady jet case. The steady jet case stagnation region Nusselt number exhibits a flat peak extending laterally, y/D = ±0.4D, and the Nusselt number suddenly drops.

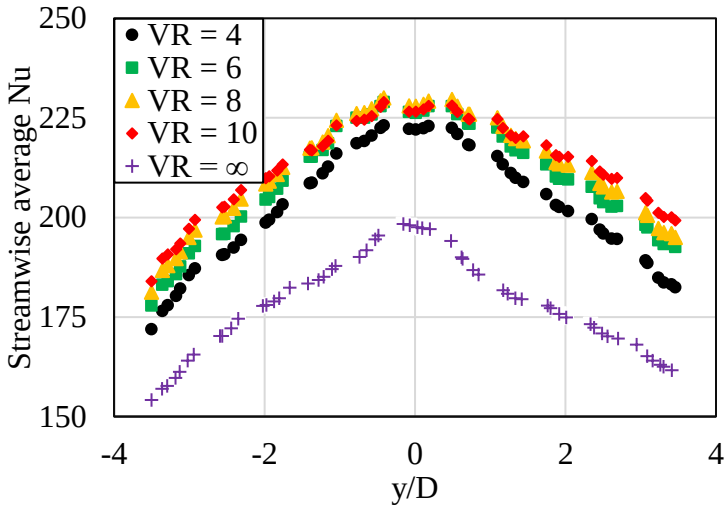

Figure 4.66 Streamwise average Nusselt number for S = 2d and d = 2D

The streamwise average Nusselt number for various velocity ratios at S/d = 3 and d = 2D is shown in Figure 4.67. The stagnation region Nusselt number increases with the increase in velocity ratio and reaches the maximum Nusselt number at velocity ratio, VR = 6. Then, further starts reducing with the increase in velocity ratio. The oscillating jet case (VR = 6) shows a maximum increase in Nusselt number of 19% in Nusselt number in the stagnation region than the steady jet case. And a maximum Nusselt number increase of 17% in the sidewall region.

The non-oscillating jet cases show a reduced heat transfer rate in the stagnation region compared to oscillating jet cases. However, the non-oscillating jet case (VR = 12) outperforms the oscillating jet case in the sidewall region. And the stagnation region Nusselt number starts producing the sudden drop in Nusselt number at y/D = ±0.4D, similar to the steady jet case.

Figure 4.68 shows the streamwise average Nusselt number for various velocity ratios tested at S/d = 4 and d = 2D. The results show a minimum change in Nusselt number in

the stagnation region, and maximum change is observed near the sidewall region. The sidewall Nusselt number increases with the increase in velocity ratio and a maximum increase of 18.4% compared to the steady jet case. Thus, the general trend of the experimental results is in good agreement with CFD results but higher in magnitude.

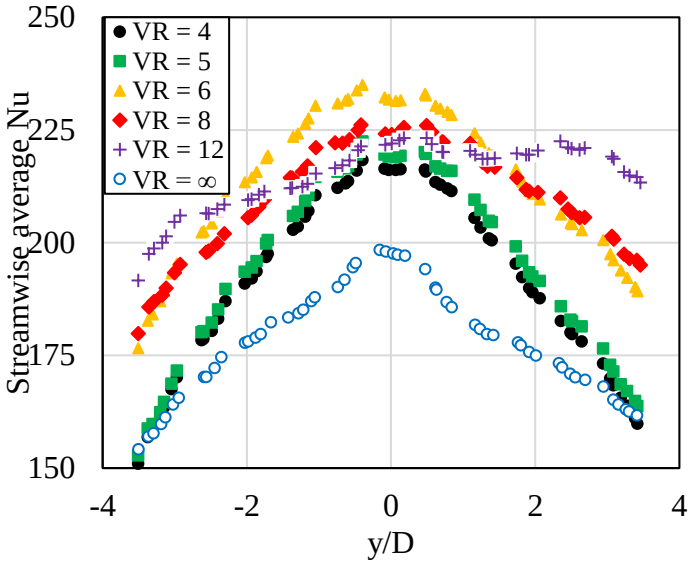

Figure 4.67 Streamwise average Nusselt number for S = 3d and d = 2D

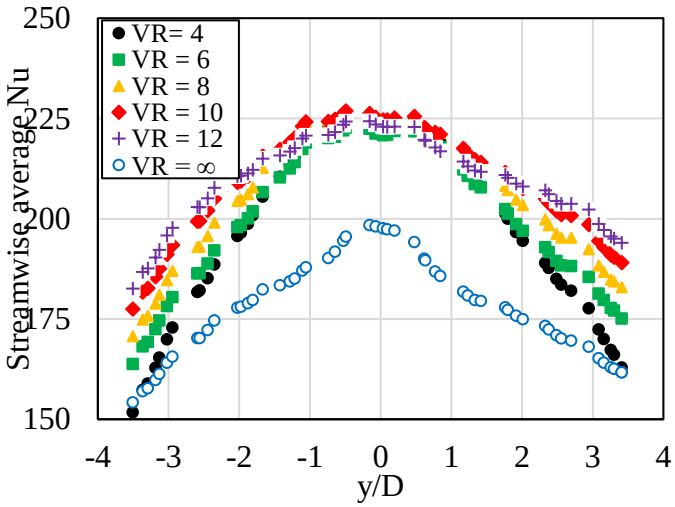

Figure 4.68 Streamwise average Nusselt number for S = 4d and d = 2D

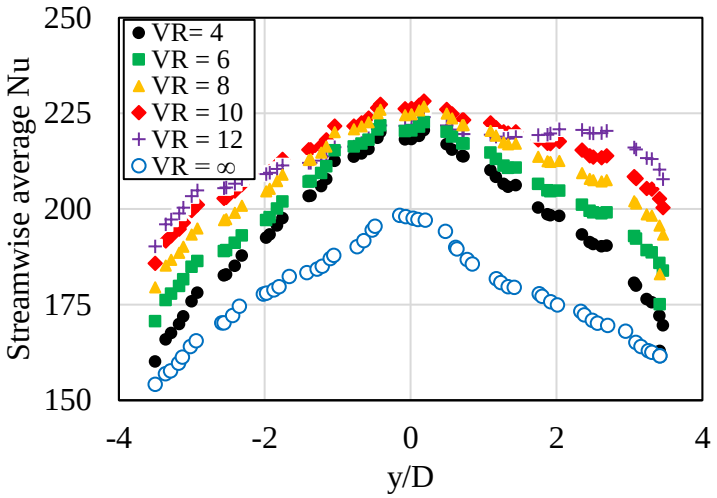

Figure 4.69 Streamwise average Nusselt number for S = 3d and d = 3D

Figure 4.69 shows the streamwise average Nusselt number for various velocity ratios tested at S = 3d and d = 3D. The results show the maximum stagnation Nusselt number for the oscillating jet with velocity ratio, VR = 10. The stagnation and sidewall region Nusselt number showed a maximum increase of 15% and 20%, respectively, for the oscillating jet compared to the steady jet case. On the other hand, the non-oscillating jet case (VR = 12) shows a decrease in stagnation region Nusselt number compared to the oscillating jet case. Also, the non-oscillating jet Nusselt number profile follows the steady jet case results, with a magnitude offset.

Summarizing the streamwise average results, the oscillating jet case with velocity ratio, VR = 6, and cylinder-jet distance, S = 3d, possess the best thermal performance compared to the steady jet case with a maximum increase of 19%. However, the experimental result uncertainty of ±9% in Nusselt number statistically reduces this effectiveness. Hence the current work claims the change in the Nusselt number trend for the oscillating jet case under the uncertainty limit.

The remaining oscillating and non-oscillating cases for d = 2D and S/d = 2, 3 & 4 show an increase of 14% in Nusselt number in the stagnation region compared to the steady jet case. As the sidewall region Nusselt number increases with velocity ratio, it can conclude uniform distribution of Nusselt number in the sidewall region.

4.4.3.4. Area Average Nusselt Number

The area-averaged Nusselt number is calculated to determine the overall effect of the oscillating and non-oscillating jet case. The area considered for averaging is the same x = ±1D stagnation region shown in Figure 4.47. The area-averaged Nusselt number result for the velocity ratio and cylinder-jet distance tested is shown in Figure 4.70. For thermal comparison with the steady jet case, the individual test results are divided by steady jet case average Nusselt number, Nu_0 = 175.84.

The results show an increase in the average Nusselt number with the increase in velocity ratio. The Nusselt number change does plateau for higher velocity ratios. The increase in Nusselt number is lowest for the cylinder-jet distance, S/d = 4. The plot for S/d = 3 dose shows a sudden increase in Nusselt number at velocity ratio, VR = 6.

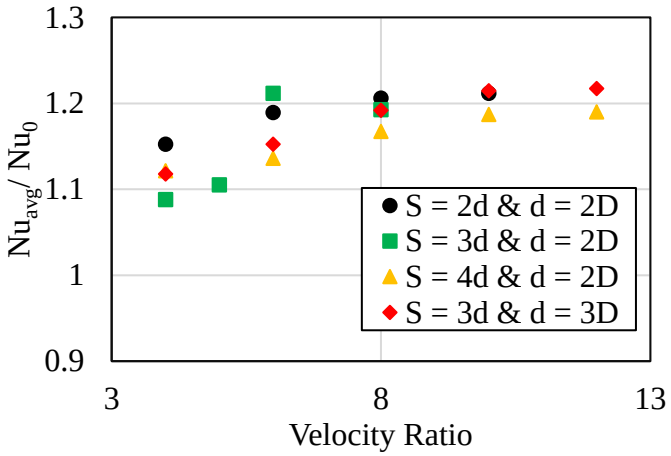

Figure 4.70 Area average Nusselt number for varying velocity ratios

5. Conclusions

The overall objective of this study is to investigate the flow interaction of an impinging jet with vortex structures periodically shed from a cylinder to impart jet oscillation leading to enhanced heat transfer rates. Further, perform CFD and experimental analysis to understand the underlying flow physics causing the jet oscillation and develop an optimum design with correlations.

The preliminary response surface sensitivity results prove the feasibility of the hypothesis to use vortex shedding from the cylinder to oscillate an impinging jet laterally. And, to prove jet oscillation leads to a more uniform distribution of Nusselt number, potentially reducing thermal stress in the material. The statistical analysis for the 25 cases studied led to jet oscillation for only two cases, concluding the jet oscillation is highly sensitive to the parameters analyzed. The shear layer detached from the cylinder attaches to the jet when placed at a distance of 1 - 2 jet diameter downstream; additionally, the crossflow velocity also affects this phenomenon. The jet oscillation occurred only for the cylinder hieght equal to the channel height, below which the cylinder tip vortex had an adverse effect on the production of cylinder wakes and jet oscillation.

A correlation was developed to determine the impact of each parameter and its combination; a thorough understanding of the sensitivities led to the development of preliminary correlation and optimization of the jet oscillation. The jet oscillation critical parameters are the cylinder height, the cylinder-jet distance, and crossflow Reynolds number. The major contributor is the cylinder height and the crossflow Reynolds number, which is proportional to the vortex strength generated by the cylinder.

From the initial spectral analysis, a method was developed to distinguish oscillating

and non-oscillating jet cases. FFT analysis has been carried out on the collected unsteady velocity and pressure measurement to determine cylinder and jet oscillation frequency. Also, the effect of cylinder diameter and channel Reynolds number on the cylinder vortex strength is determined for various distances downstream in the channel by mapping the local turbulence intensity. A conclusion has been defined on the interaction of the cylinder vortex strength with the downstream jet leading to jet oscillation. Also, it was determined that higher cylinder diameter and lower channel velocities are more efficient for jet oscillation.

A significant conclusion on the effect of cylinder wakes on jet oscillation is the steps leading to jet oscillation. Firstly, the local turbulence intensity for the particular cylinder diameter has to be higher than the threshold, TI = 0.39. Finally, the jet has to be sufficiently placed away from the low-pressure recirculation region such that it is not deflected into this region.

The flow field of the jet in a crossflow (JICF) is primarily affected by the velocity ratio (VR). The above initial results did study the effect of channel Reynolds Number on jet oscillation, but the velocity ratio was not calculated or given any importance. In the final analysis, the flow interaction between the cylinder wake and jet was studied in detail for various velocity ratios. The varying parameters in the final CFD and experimental investigation are the velocity ratio, cylinder-jet distance, and cylinder diameter. Firstly, a spectral analysis was followed to distinguish oscillating and non-oscillating jets. The CFD spectral analysis came across an anomaly where no jet oscillation was observed, although cylinder wakes were produced.

The detailed mechanism of wake-jet interaction leading to jet oscillation is explained

using TKE, vorticity, and velocity contours at different time intervals. The result showed the cylinder wakes deformed the jet core and induced lateral and angular oscillations. The jet core also produces wakes, inducing momentum driving the jet oscillation. However, the jet core wakes were not synchronized with the cylinder wakes, reducing jet oscillation at specific time intervals. Also, the flow interaction leading to a non-oscillating jet is analyzed. The flow features of the anomaly observed in the spectral analysis are analyzed in detail. Anamoly states in the presence of cylinder wake, the jet may not oscillate if the vortex strength is insufficient.

The final objective of the current study is to derive an optimum design of jet oscillation for maximum heat transfer rate. Therefore, the effect of oscillating cases and non-oscillating jet cases on heat transfer rate are quantified for different cylinder-jet distances, velocity ratios, and cylinder diameters. The local Nusselt distribution discusses the effect of velocity ratio and cylinder-jet distance on the stagnation region and wall jet region Nusselt number.

The CFD results concluded the stagnation region of non-oscillating jet cases resembled a bean shape due to the jet core deformation. The oscillating jet cases possessed a unique stagnation region shape showing off uniform Nusselt number distribution. The spanwise average Nusselt number results concluded the Nusselt number distribution is significantly affected by the crossflow strength. The peak Nusselt number determined for all the non-oscillating cases is equal to $Nu = 153 \pm 3$. The oscillating jet cases spanwise average results were less than the non-oscillating jet case results. However, the jet oscillates in the spanwise direction; hence the streamwise average results are appreciated to certify the thermal performance of oscillating and non-

oscillating jet cases.

To understand the effect of oscillating jet, the streamwise average Nusselt number was averaged in the oscillating jet region, x = ±1D of stagnation region. The streamwise average results concluded the non-oscillating cases for S/d = 2, 3 and 4, show the same increase of 27% in Nusselt number in the stagnation region. However, a maximum increase of 36% is observed for the oscillating jet cases compared to the steady jet case. Also, the Nusselt number distribution is uniformly distributed compared to the non-oscillating and steady jet case. The area-averaged results showed minimum change, as the jet Reynold number is constant.

The experimental heat transfer results concluded the stagnation region bean shape is dominant in both oscillating and non-oscillating jet cases. And the wall jet region is extended laterally in the y-direction with the increase in velocity ratio. The spanwise average results concluded the Nusselt number distribution is significantly affected by the crossflow strength similar to CFD results. The non-oscillating jet enhances heat transfer rate in the upstream region by 94% in Nusselt number.

The streamwise average results concluded the oscillating jet case with a velocity ratio of VR = 6, cylinder diameter of d = 2D, and cylinder-jet distance of S = 3d possess the best thermal performance. Hence, this oscillating case is considered the current work's optimum design for maximum heat transfer rates. The oscillating jet results compared to the steady jet case showed a maximum increase of 19%. However, the experimental result uncertainty of ±9% in Nusselt number restricts in claiming this increase. Hence the current work claims there is an increase in the Nusselt number for the oscillating jet case. But the percentage increase in Nusselt number is governed by the uncertainty limit.

The uncertainty of the heat transfer experiment result is crucial; hence, future work should develop new methods to reduce error. Further studies have to be conducted to synchronous the cylinder wake and jet core wake shedding for maximum effectiveness. Also, the effect of inlet conditions should be studied for the application of this method in a gas turbine blade.

REFERENCES

Agricola, L., Prenter, R., Lundgreen, R., Hossain, M., Ameri, A., Gregory, J., & Bons, J. (2017, July). Impinging sweeping jet heat transfer. In *53rd AIAA/SAE/ASEE Joint Propulsion Conference* (p. 4974).

Alam, M. M., Moriya, M., Takai, K., & Sakamoto, H. (2003). Fluctuating fluid forces acting on two circular cylinders in a tandem arrangement at a subcritical Reynolds number. *Journal of Wind Engineering and Industrial Aerodynamics*, 91(1-2), 139-154. doi:10.1016/S0167-6105(02)00341-0

Anagnostopoulos, P., Iliadis, G., & Richardson, S. (1996). Numerical study of the blockage effects on viscous flow past a circular cylinder. *International Journal for Numerical Methods in Fluids*, 22(11), 1061-1074. doi:10.1002/(SICI)1097-0363(19960615)22:11%3C1061::AID-FLD393%3E3.0.CO;2-Q

Arthurs, David, and Samir Ziada. "Self-excited oscillations of a high-speed impinging planar jet." *Journal of fluids and structures* 34 (2012): 236-258. doi:10.1016/j.jfluidstructs.2012.06.002

Bartesaghi, S., & Colombo, G. (2013). Embedded CFD simulation for blood flow. *Computer-Aided Design and Applications*, 10(4), 685-699. doi:10.3722/cadaps.2013.685-699

Bearman, P. W. (1969). On vortex shedding from a circular cylinder in the critical Reynolds number regime. *Journal of Fluid Mechanics*, 37(3), 577-585. doi:10.1017/S0022112069000735

Bell, J. H., Schairer, E. T., Hand, L. A., & Mehta, R. D. (2001). Surface pressure measurements using luminescent coatings. *Annual Review of Fluid Mechanics*, 33, 155-206. doi:10.1146/annurev.fluid.33.1.155

Boyce, M. P. (2011). *Gas turbine engineering handbook*. Elsevier.

Camci, C., & Herr, F. (2002). Forced convection heat transfer enhancement using a self-oscillating impinging planar jet. *Journal of Heat Transfer*, 124(4), 770-782. doi:10.1115/1.1471521

Chakroun, W. M., Abdel-Rahman, A. A., & Al-Fahed, S. F. (1998). Heat transfer augmentation for air jet impinged on a rough surface. *Applied thermal engineering*, 18(12), 1225-1241. doi:10.1016/S1359-4311(97)00100-2

Chiekh, M. B., Ferchichi, M., & Béra, J. C. (2011). Modified flapping jet for increased jet spreading using synthetic jets. *International Journal of Heat and Fluid Flow*, 32(5), 865-875. doi:10.1016/j.ijheatfluidflow.2011.06.004

Chiriac, V. A., Lee, T. Y. T., & Rosales, J. L. (2002, January). Microelectronic cooling techniques using single and dual oscillatory impinging air jets. In *ASME 2002 International Mechanical Engineering Congress and Exposition* (pp. 171-178). American Society of Mechanical Engineers Digital Collection.

Chung, Y. M., & Luo, K. H. (2002). Unsteady heat transfer analysis of an impinging jet. *Journal of Heat Transfer*, 124(6), 1039-1048. doi:10.1115/1.1469522

da Silveira, L. T., Pereira, L. A. A., & Hirata, M. H. (2005, November). The Effects of Interference between Two Circular Cylinders Arranged in Tandem by Vortex Method. In *18th International Congress of Mechanical Engineering, Proceedings of COBEM* (pp. 6-11).

Fernandes, R., Ricklick, M., Prasad, A., & Pai, Y. (2017). Benchmarking reynolds averaged navier–stokes turbulence models in internal pin fin channels. *Journal of Thermophysics and Heat Transfer*, 31(4), 976-982. doi:10.2514/1.T5046

Florschuetz, L. W., Truman, C. R., & Metzger, D. E. (1981, March). Streamwise flow and heat transfer distributions for jet array impingement with crossflow. In *Turbo Expo: Power for Land, Sea, and Air* (Vol. 79634, p. V003T09A005). American Society of Mechanical Engineers.

Florschuetz, L. W., Metzger, D. E., Takeuchi, D. I., & Berry, R. A. (1980). Multiple jet impingement heat transfer characteristic: Experimental investigation of in-line and staggered arrays with crossflow. Final Report Arizona State Univ.

Giordano, R., Astarita, T., & Carlomagno, G. M. (2008, July). Vortex shedding in the near wake of a finite cylinder. In *The 14th International Symposium on Applications of Laser Techniques to Fluid Mechanics*, Lisbon, Portugal.

Griffith, M. D., Leontini, J., Thompson, M. C., & Hourigan, K. (2011). Vortex shedding and three-dimensional behaviour of flow past a cylinder confined in a channel. *Journal of Fluids and Structures*, 27(5-6), 855-860. doi:10.1016/j.jfluidstructs.2011.02.007

Halbig, M., Jaskowiak, M., Kiser, J., & Zhu, D. (2013, January). Evaluation of ceramic matrix composite technology for aircraft turbine engine applications. In *51st AIAA Aerospace Sciences Meeting including the New Horizons Forum and Aerospace Exposition* (p. 539).

Han, J. C., Dutta, S., & Ekkad, S. (2012). *Gas turbine heat transfer and cooling technology*. CRC press.

Haneda, Y., Tsuchiya, Y., Nakabe, K., & Suzuki, K. (1998). Enhancement of impinging jet heat transfer by making use of mechano–fluid interactive flow oscillation. *International journal of heat and fluid flow*, 19(2), 115-124. doi:10.1016/S0142-

727X(97)10016-9

He, G., Guo, Y., Hsu, A. T., Brankovic, A., Syed, S., & Liu, N. S. (1999, June). The effect of Schmidt number on turbulent scalar mixing in a jet-in-crossflow. In *Turbo Expo: Power for Land, Sea, and Air* (Vol. 78590, p. V002T02A029). American Society of Mechanical Engineers.

Herwig, H., Mocikat, H., Gürtler, T., & Göppert, S. (2004). Heat transfer due to unsteadily impinging jets. *International journal of thermal sciences*, 43(8), 733-741. doi:10.1016/j.ijthermalsci.2004.02.013

Hewakandamby, B. N. (2009). A numerical study of heat transfer performance of oscillatory impinging jets. *International Journal of Heat and Mass Transfer*, 52(1-2), 396-406. doi:10.1016/j.ijheatmasstransfer.2008.07.004

Hidalgo, P., Herrault, F., Glezer, A., Allen, M., Kaslusky, S., & Rock, B. S. (2010, October). Heat transfer enhancement in high-power heat sinks using active reed technology. In 2010 *16th International Workshop on Thermal Investigations of ICs and Systems (THERMINIC)* (pp. 1-6). IEEE.

Hidalgo, P., Jha, S., & Glezer, A. (2015, September). Enhanced heat transfer in air cooled heat sinks using aeroelastically fluttering reeds. In 2015 *21st International Workshop on Thermal Investigations of ICs and Systems (THERMINIC)* (pp. 1-6). IEEE.

Hidalgo, P., & Glezer, A. (2015, July). Small-scale vorticity induced by a self-oscillating fluttering reed for heat transfer augmentation in air cooled heat sinks. In *International Electronic Packaging Technical Conference and Exhibition* (Vol. 56888, p. V001T09A004). American Society of Mechanical Engineers.

Hill, P. G., & Peterson, C. R. (1992). *Mechanics and thermodynamics of propulsion*. Reading.

Hossain, M. A., Ameri, A., Gregory, J. W., & Bons, J. P. (2018). Sweeping jet impingement heat transfer on a simulated turbine vane leading edge. *Journal of the Global Power and Propulsion Society*, 2, 402-414. doi:10.22261/JGPPS.5A7OAZ

Inoue, T., Nagahata, F., & Hirata, K. (2016). On Switching of a Flip-Flop Jet Nozzle with Double Ports by Single-Port Control. *Journal of Flow Control, Measurement & Visualization*, 4(04), 143. doi:10.4236/jfcmv.2016.44013

Kalter, R., Tummers, M. J., Kenjereš, S., Righolt, B. W., & Kleijn, C. R. (2014). Effects of electromagnetic forcing on self-sustained jet oscillations. *Physics of Fluids*, 26(6), 065101. doi:10.1063/1.4880897

Karagozian, A. R. (2014). The jet in crossflow. *Physics of Fluids*, 26(10), 1-47. doi:10.1063/1.4895900

Khan, W. A., Culham, J. R., & Yovanovich, M. M. (2004). Fluid flow and heat transfer from a cylinder between parallel planes. *Journal of thermophysics and heat transfer*, 18(3), 395-403. doi:10.2514/1.6186

Koklu, M., & Owens, L. R. (2014, June). Flow separation control over a ramp using sweeping jet actuators. In *7th AIAA Flow Control Conference* (p. 2367).

Kolšek, T., Jelić, N., & Duhovnik, J. (2007). Numerical study of flow asymmetry and self-sustained jet oscillations in geometrically symmetric cavities. *Applied mathematical modelling*, 31(10), 2355-2373. doi:10.1016/j.apm.2006.10.010

Lawson, N. J., & Davidson, M. R. (2001). Self-sustained oscillation of a submerged jet in a thin rectangular cavity. *Journal of fluids and structures*, 15(1), 59-81. doi:10.1006/jfls.2000.0327

Lee, D. Y., & Vafai, K. (1999). Comparative analysis of jet impingement and microchannel cooling for high heat flux applications. *International Journal of Heat and Mass Transfer*, 42(9), 1555-1568. doi:10.1016/S0017-9310(98)00265-8

Liang, G. (2012). U.S. Patent No. 8,297,927. Washington, DC: U.S. Patent and Trademark Office.

Ligrani, P. M., Oliveira, M. M., & Blaskovich, T. (2003). Comparison of heat transfer augmentation techniques. *AIAA journal*, 41(3), 337-362. doi:10.2514/2.1964

Liu, Q. (2006). Study Of Heat Transfer Characteristics Of Impinging Air Jet Using Pressure And Temperature Sensitive Luminescent Paint. (PhD Dissertation). https://stars.library.ucf.edu/etd/791/

Liu, T., Campbell, B., & Sullivan, J. (1995, June). Accuracy of temperature-sensitive fluorescent paint for heat transfer measurements. In *30th Thermophysics Conference* (p. 2042).

Lundgreen, R. K., Hossain, M. A., Prenter, R., Bons, J. P., Gregory, J. W., & Ameri, A. (2017, January). Impingement heat transfer characteric of a sweeping jet. In *55th AIAA Aerospace Sciences Meeting* (p. 1535).

Martin, H. (1977). Heat and mass transfer between impinging gas jets and solid surfaces. *In Advances in heat transfer* (Vol. 13, pp. 1-60). Elsevier. doi:10.1016/S0065-2717(08)70221-1

Mataoui, A., & Schiestel, R. (2009). Unsteady phenomena of an oscillating turbulent jet flow inside a cavity: Effect of aspect ratio. *Journal of Fluids and Structures*,

25(1), 60-79. doi:10.1016/j.jfluidstructs.2008.03.010

Middelberg, G., & Herwig, H. (2009). Convective heat transfer under unsteady impinging jets: the effect of the shape of the unsteadiness. *Heat and mass transfer*, 45(12), 1519-1532. doi:10.1007/s00231-009-0527-4

Muppidi, S., & Mahesh, K. (2007). Direct numerical simulation of round turbulent jets in crossflow. *Journal of Fluid Mechanics*, 574, 59-84. doi:10.1017/S0022112006004034

Nguyen, C. Q. (2010). Interaction Between Secondary Flow & Film Cooling Jets of a Realistic Annular Airfoil Cascade (High Mach Number). (PhD Dissertation). https://stars.library.ucf.edu/etd/1651/

O'Donovan, T. S., & Murray, D. B. (2007). Jet impingement heat transfer–Part I: Mean and root-mean-square heat transfer and velocity distributions. *International journal of heat and mass transfer*, 50(17-18), 3291-3301. doi:10.1016/j.ijheatmasstransfer.2007.01.044

Okamoto, S., and Sunabashiri, Y. (December 1, 1992). "Vortex Shedding From a Circular Cylinder of Finite Length Placed on a Ground Plane." *ASME. J. Fluids Eng*. December 1992; 114(4): 512–521. doi:10.1115/1.2910062

Pack, L. G., & Seifert, A. (2001). Periodic excitation for jet vectoring and enhanced spreading. *Journal of Aircraft*, 38(3), 486-495. doi:10.2514/2.2788

Page, R. H., Chinnock, P. S., & Seyed-Yagoobi, J. (1996). Self-oscillation enhancement of impingement jet heat transfer. *Journal of thermophysics and heat transfer*, 10(2), 380-382. doi:10.2514/3.799

Parida, P. Cold plate with combined inclined impingement and ribbed channels. U.S. Patent Application No. 14/716,329.

Park, C. W., & Lee, S. J. (2000). Free end effects on the near wake flow structure behind a finite circular cylinder. *Journal of Wind Engineering and Industrial Aerodynamics*, 88(2-3), 231-246. doi:10.1016/S0167-6105(00)00051-9

Prasad, A. (2021). Investigation of Bio-Inspired Pin Geometries for Enhanced Heat Transfer Applications. (PhD Dissertation). https://commons.erau.edu/edt/589/

Prasad, A. (2016). A Detailed Uncertainty Analysis of Heat Transfer Experiments Using Temperature Sensitive Paint. (Master's Thesis). https://commons.erau.edu/edt/311/

Platzer, M. F., Simmons, J. M., & Bremhorst, K. (1978). Entrainment characteristics of unsteady subsonic jets. *AIAA Journal*, 16(3), 282-284. doi:10.2514/3.7523

Raman, G., & Cornelius, D. (1995). Jet mixing control using excitation from miniature oscillating jets. *AIAA journal*, 33(2), 365-368. doi:10.2514/3.12444

Ricklick, M. (2009). Characterization of an inline row impingement channel for turbine blade cooling applications. (Master's Theses). https://stars.library.ucf.edu/etd/3929/

Ricklick, M., Kapat, J. S., & Heidmann, J. (2010). Sidewall effects on heat transfer coefficient in a narrow impingement channel. *Journal of thermophysics and heat transfer*, 24(1), 123-132. doi:10.2514/1.44166

Ricklick, M., Claretti, R., & Kapat, J. S. (2010, October). Channel height and jet spacing effect on heat transfer and uniformity coefficient on an inline row impingement channel. In *Turbo Expo: Power for Land, Sea, and Air* (Vol. 43994, pp. 675-684).

Ricklick, M., & Kapat, J. S. (2011). Determination of a local bulk temperature based heat transfer coefficient for the wetted surfaces in a single inline row impingement channel. *Journal of turbomachinery*, 133(3). doi:10.1115/1.4001227

Ricklick, Mark, Phil Poinsatte, Doug Thurman, (2015). Preliminary Assessment of the Implication of CMC Surface Features on Gas Turbine Cooling Methodologies. NASA-Faculty Fellowship Program Final Report, summer 2015.

Ricklick, M. A., & Carpenter, C. (2014, July). Comparison of Heat Transfer Prediction for Various Turbulence Models in a Pin Fin Channel. In *50th AIAA/ASME/SAE/ASEE Joint Propulsion Conference* (p. 3838).

Righolt, B. W., Kenjereš, S., Kalter, R., Tummers, M. J., & Kleijn, C. R. (2015). Dynamics of an oscillating turbulent jet in a confined cavity. *Physics of Fluids*, 27(9), 095107. doi:10.1063/1.4930926

Shukla, A. K., & Dewan, A. (2017). Flow and thermal characteristics of jet impingement: comprehensive review. *International Journal of Heat Technology*, 35(1), 153-166. doi:10.18280/ijht.350121

Singh, S., Acharya, S., & Ames, F. (2017, July). Cooling Performance Comparison of a Low Aspect Ratio Incremental Impingement Pin-Fin Channel Configurations. In *ASME 2017 Heat Transfer Summer Conference*. American Society of Mechanical Engineers Digital Collection.

Smith, B. L., & Glezer, A. (2005). Vectoring of adjacent synthetic jets. *AIAA journal*, 43(10), 2117-2124. doi:10.2514/1.12910

Tamburello, D. A., & Amitay, M. (2008). Active control of a free jet using a synthetic jet. *International journal of heat and fluid flow*, 29(4), 967-984. doi:10.1016/j.ijheatfluidflow.2008.02.017

Tesař, V., Hung, C. H., & Zimmerman, W. B. (2006). No-moving-part hybrid-synthetic jet actuator. *Sensors and Actuators A: Physical*, 125(2), 159-169. doi:10.1016/j.sna.2005.06.022

Tesař, V. (2009). Enhancing impinging jet heat or mass transfer by fluidically generated flow pulsation. *Chemical Engineering Research and Design*, 87(2), 181-192. doi:10.1016/j.cherd.2008.08.003

Trávníček, Z., Tesař, V., Broučková, Z., & Peszyński, K. (2014). Annular impinging jet controlled by radial synthetic jets. *Heat transfer engineering*, 35(16-17), 1450-1461. doi:10.1080/01457632.2014.889467

Tomac, M. N., & Gregory, J. (2012, January). Frequency studies and scaling effects of jet interaction in a feedback-free fluidic oscillator. In *50th AIAA Aerospace Sciences Meeting including the New Horizons Forum and Aerospace Exposition* (p. 1248).

Uzol, O., & Camci, C. (2002). Experimental and computational visualization and frequency measurements of the jet oscillation inside a fluidic oscillator. *Journal of Visualization*, 5(3), 263-272. doi:10.1007/BF03182334

Viets, H. (1975). Flip-flop jet nozzle. *AIAA journal*, 13(10), 1375-1379. doi:10.2514/3.60550

Williamson, C. H. (1996). Vortex dynamics in the cylinder wake. *Annual review of fluid mechanics*, 28(1), 477-539. doi:10.1146/annurev.fl.28.010196.002401

Yang, L., Ren, J., Jiang, H., & Ligrani, P. (2014). Experimental and numerical investigation of unsteady impingement cooling within a blade leading edge passage. *International Journal of Heat and Mass Transfer*, 71, 57-68. doi:10.1016/j.ijheatmasstransfer.2013.12.006

Yang, L., Ligrani, P., Ren, J., & Jiang, H. (2015). Unsteady structure and development of a row of impingement jets, including Kelvin–Helmholtz vortex development. *Journal of Fluids Engineering*, 137(5). doi:10.1115/1.4029386

Yu, Y., Simon, T. W., Zhang, M., Yeom, T., North, M. T., & Cui, T. (2014). Enhancing heat transfer in air-cooled heat sinks using piezoelectrically-driven agitators and synthetic jets. *International Journal of Heat and Mass Transfer*, 68, 184-193. doi:10.1016/j.ijheatmasstransfer.2013.09.001

Zhou, J. W., Wang, Y. G., Middelberg, G., & Herwig, H. (2009). Unsteady jet impingement: heat transfer on smooth and non-smooth surfaces. *International Communications in Heat and Mass Transfer*, 36(2), 103-110. doi:10.1016/j.icheatmasstransfer.2008.10.020

Zuckerman, N., & Lior, N. (2006). Jet impingement heat transfer: physics, correlations,

and numerical modeling. *Advances in heat transfer*, 39, 565-631. doi:10.1016/S0065-2717(06)39006-5

PUBLICATIONS

Krishna, K., & Ricklick, M. A. (2020, January). Effect of Cylinder vortex shedding on downstream Impinging Jet Oscillation through Wake Interaction. In *AIAA Scitech 2020 Forum* (p. 0635).

Krishna, K., & Ricklick, M. A. (2019, August). Experimental Investigation of an Oscillating Jet Induced by Cylinder Wakes. In *AIAA Propulsion and Energy 2019 Forum* (p. 4255).

Krishna, K., Prasad, A., & Ricklick, M. A. (2018, January). Preliminary Numerical Investigation on the interaction of an Impinging Jet with Cylinder Wake. In *2018 AIAA Aerospace Sciences Meeting* (p. 0389).

Krishna, K., & Ricklick, M. (2017, June). Heat Transfer Analysis of Jet Impingement Cooling on a Simulated Ceramic Matrix Composite Surface. In *Turbo Expo: Power for Land, Sea, and Air* (Vol. 50879, p. V05AT13A009). American Society of Mechanical Engineers.

Krishna, K. (2016). Heat Transfer Analysis of an Oblique Jet Impingement Cooling on CMC Rough Surface. (Master's Thesis). https://commons.erau.edu/edt/303/

Krishna, K., & Ricklick, M. A. (2016, July). Preliminary investigation of an oblique jet impingement cooling on a CMC rough surface. In *52nd AIAA/SAE/ASEE Joint Propulsion Conference* (p. 4851).